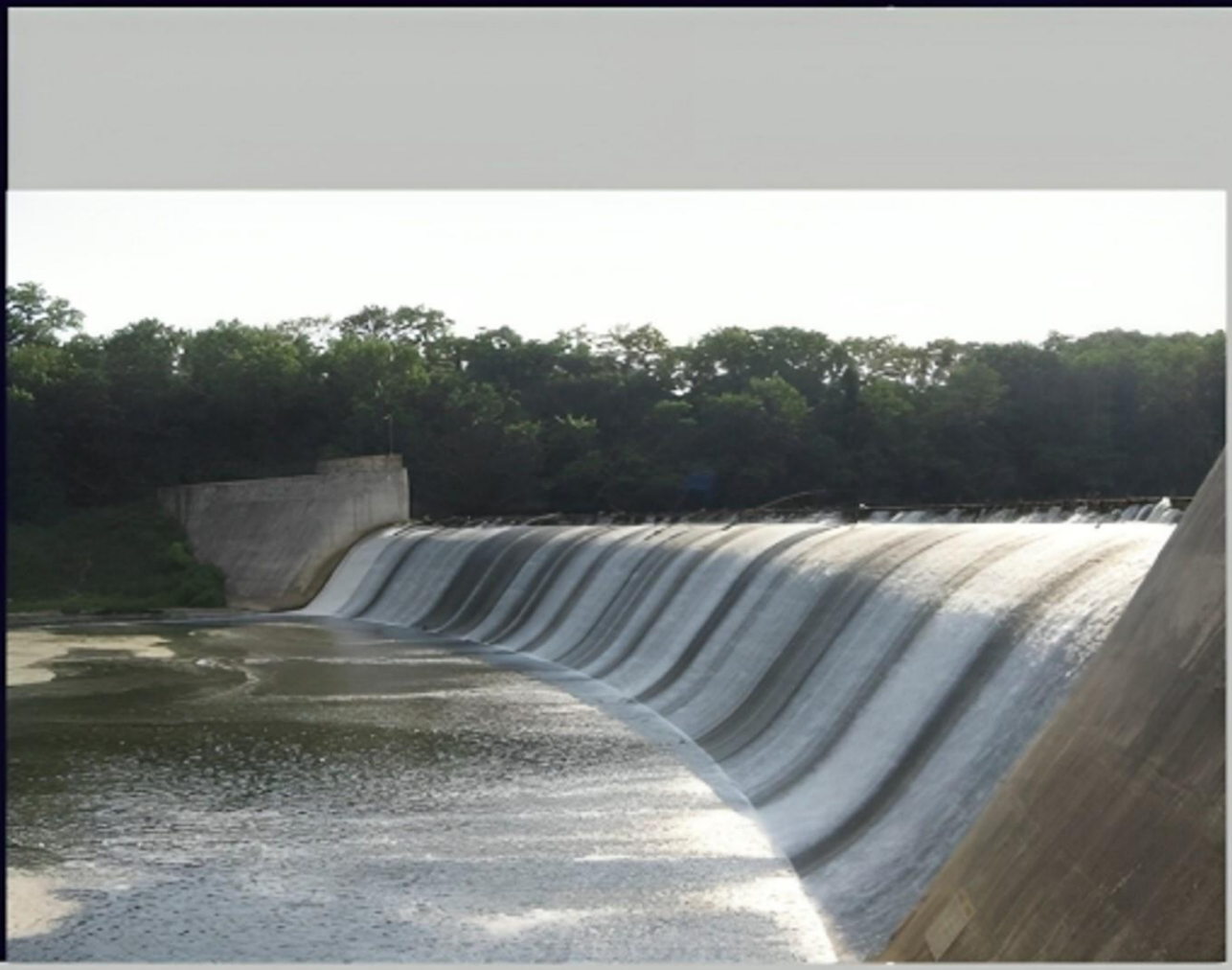
Iranian Hydraulic Association

Shahid Chamran University of Ahvaz

Journal of Hydraulic Structures

Scientific Professional Journal



April 2025
Volume 11, Issue 2

ISSN (Online): 2345-4156
https://jhs.scu.ac.ir/

Aims and Scope

Journal of Hydraulic Structures is an interdisciplinary journal which publishes high-quality peer-reviewed articles addressing the latest developments and applied methods in analysis and design, construction, maintenance, management, and operation policy of Hydraulic Structures.

The Journal aims at providing an efficient route to fast-track publication, within 10-12 weeks after manuscript submission.

The general areas covered by the Journal include:

- Advances in numerical and analytical methods applicable to hydraulic structures
- Hydro informatics and soft computing
- Hydraulic aspects of hydraulic structures
- Applied surface and subsurface hydrology and hydrometeorology
- Forecasting approaches in water resources engineering
- Economic and social aspects of hydraulic structures
- Uncertainty analysis and risk management in hydraulics and water resources engineering
- Application of Nanotechnology in hydraulic structures
- Geotechnics of hydraulic structures
- Damage detection techniques
- Technical and methodological advances in application, design/selection, production, construction materials of hydraulic structures.
- Application of Artificial Intelligence techniques in all aspects of hydraulic structures.

General Information:

Title: Journal of Hydraulic Structures

Publisher: Shahid Chamran University of Ahvaz

ISSN (Print): 2345-413X

ISSN (Online): 2345-4156

Website: https://jhs.scu.ac.ir/

Address: Faculty of Civil Engineering and Architecture, Shahid Chamran University of Ahvaz, Ahvaz, Iran

Email: jhs@scu.ac.ir

Journal of

Hydraulic Structures

Shahid Chamran University of Ahvaz

Director-in-Charge: Prof. Ali Haghighi

Editor-in-Chief: Prof. Hamid R. Ghafouri

Managing Editor: Dr. Amir H. Shafiee

Contents:

01

Construction of Meandering Channel and Its Application in Investigation of Bed Topography around Hydraulic Structures

Nargess Moghaddassi; Mohammad Vaghefi

28

Simulation of Tsunami Waves Using Mike 3 Flow Model FM

Vahid Naderkhanloo; Mohammad Hemmati; Hojjat Ahmadi

44

An investigation on the parameters affecting the behavior of broadly graded, dispersive base soil-filter systems in earth dams

Amir Hossein Vakili; Amin Falamaki

61

Investigating the Behavior of Jacket Offshore Steel Structure under Blast Loading

Farhad Hosseinlou; Wissam Asaad Ibrahim; Mojtaba LabibZadeh

87

Investigating the vulnerability of underground water to pollution (case study: East and Northeast of Chaharmahal and Bakhtiari province)

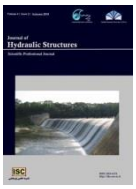
Mohammadsadegh Talebi

108

Full scale optimization of chlorine injection pattern in Khansar water distribution network using WaterGEMS

Ali Poorkarimi; Habib Asi; Shahrzad Maleki

Journal of Hydraulic Structures
J. Hydraul. Struct., 2024;11(2):1-27
DOI: 10.22055/jhs.2024.47556.1314



OPEN ACCESS

Construction of Meandering Channel and Its Application in Investigation of Bed Topography around Hydraulic Structures

Nargess Moghaddassi [*1]
Mohammad Vaghefi [2]

Abstract

Considering river behavior analysis, numerous researchers worldwide have so far attempted to construct experimental channels. This piece of research discussed the construction of a channel with two bends and its application. Beginning from the upstream side, the channel respectively consisted of an 8-meter-long straight path, two consecutive 180-degree bends, and another 8-meter-long straight path downstream. In addition to presenting the stages of design and construction of this channel, this study provided some instances, where different hydraulic structures, including a T-shaped spur dike, a gate, sharp-edged and wide-edged spillways, submerged vanes, and a bridge pier, were implemented in meandering paths. A comparison of the results from the use of different hydraulic structures in this meandering channel showed that these structures had different effects on bed topography variations. For instance, under similar flow conditions, the maximum scour depth increased in the sharp-edged spillway experiment by approximately 40% compared to that in the wide-edged spillway experiment. In addition, the maximum scour around the T-shaped spur dike located in the external bend was 2.7 times greater than that with the case it was placed at the upstream internal bend. Reviewing the results of two cases of using submerged vanes in front of a single pier located at an angle of 180 degrees in the meandering channel, as compared to the case of a single pier without the use of vanes shows that the maximum scour depth around the bridge pier was reduced by approximately 10% when utilizing submerged vanes in conjunction with the single pier. Furthermore, by positioning three submerged vanes at the intersection of the two bends, the maximum depth of the scour hole was observed to occur at an angle of 358 degrees, located at a distance equivalent to 5% of the channel width from the outer wall, corresponding to 0.185 times the channel width. By repositioning the T-shaped spur dike to a 180-degree angle from the outer bend to the inner bend, an increase of nearly 35% was observed in the maximum scour within the bend.

Keywords: Flume Experiments; Scour; Spur Dike; Submerged Vanes; Bridge Piers

Received: 06 August 2024; Accepted: 06 October 2024

[*] E-mail: nmoghaddassi@pnu.ac.ir (**Corresponding Author**)
[1] Department of Civil Engineering, Payame Noor University, Nakhl Street, 193953697, Tehran, Iran.
[2] Department of Civil Engineering, Persian Gulf University, 7516913817, Bushehr, Iran.

CC BY

1. Introduction

Predicting river behavior, particularly at bends, is of great importance as rivers mostly have meandering paths in nature, Akbari and Vaghefi [1]. It is highly complicated to use field studies and mathematical computations to study river processes. Nevertheless, physical modeling can be used as a complementary method for simulating complicated processes, Peakall and Ashworth [2]. However, developing such models is often highly costly and sometimes impossible. While constructing experimental and research channels under specific conditions helps researchers study river behavior, this method has made possible many research studies conducted on laboratory channels. After inspections made on the quality and conditions of different research channels and considerations of the importance that meandering rivers have, this study has involved the design and construction of a meandering channel to make different experimental studies feasible for studying the behavior of river structures present in it.

A review of the research conducted around river engineering topics refers to the particular importance of studying the flow behavior in bends in different experimental channels with varied materials, dimensions, and shapes worldwide. Instances of hydraulic channels incorporated by researchers at different research institutes all over the world have been introduced as follows:

Researchers such as Raudkivi and Ettema [3], Chiew and Melville [4], Chiew [5], Shakibaeinia et al. [6], Nazari-Giglou et al. [7], Vaghefi et al. [8], Wang et al. [9], Yagci et al. [10], Chavan and Kumar [11], and Zou et al. [12] utilized straight channels to carry out their experiments.

Since flow and sediment patterns in meandering river paths are more complicated than those in straight paths, river meanders and bends have received less attention from researchers. A number of these research works are mentioned here:

Tarbiat Modares University in Tehran has a collection of different experimental channels, an instance of which is a steel channel with glass walls and a 90-degree bend. Ghodsian and Vaghefi [13] and Vaghefi et al. [14,15] may be stated as instances of research studies conducted in this university. In China, Wang et al. [16] used a channel with six meandering bends. A concrete hydraulic experimental channel with a 90-degree bend was constructed in the hydraulics laboratory of Urmia University by Abdolahpour et al. [17]. Dugue et al. [18] presented their studies on a single-bend channel with PVC walls in Switzerland. The University of Minnesota in the U.S. hosts several experimental channels for researchers, and Khosronejad et al. [19] conducted some experiments in a straight channel in St. Anthony Falls Laboratory. Various channels have been used by researchers in India, among which Moharana and Khatua [20] conducted in a sinuous channel may be referred to. Termini [21] presented his research in a meandering channel having sinuous curves with an angle of 110 degrees at the University of Palermo in Italy. Queen's University in Canada has different research departments in river and coastal engineering. Meandering channels made of PVC have been used by numerous researchers, including Binns and da Silva [22]. Mera et al. [23] built a river model with construction and building materials at the University of A Coruña to study the Mero River in Cambre, Spain. Pagliara et al. [24] utilized a channel comprised of three bends for their studies. Liu et al. [25] conducted their research at Sichuan University in China on a meandering concrete channel with sinuous bends. Akhtari and Seyedashraf [26] used a channel with a 60-degree bend. In Bushehr, Persian Gulf University has a steel channel with glass walls and a 180-degree sharp bend designed and constructed by Vaghefi and Akbari [27]. Moqanlu et al. [28], Keshavarz et al. [29], Solati et al. [30], Vaghefi et al. [31], Keshavarz et al. [32], Sedighi et al. [33], and Akbari et al. [34] conducted a thorough examination of their respective findings within this 180-degree

sharp bend. Park and Ahn [35] used a double-bend, S-shaped meandering channel with a length of 16.5 meters, a width of 1 meter, and a height of 60 centimeters in South Korea to carry out their experiments. This channel consisted of two 150-degree bends connected via a 1-meter-long straight path. Serajian et al. [36] presented their experimental studies in a 90-degree bend channel in Ahvaz.

According to surveys on the experimental channels available in different universities and research institutes, it has been observed that channels with a straight path or with a single bend have been constructed in most laboratories. These few meandering channels under investigation are also mostly straight channels that have been changed from straight into meandering using construction materials to study the behavior of meandering rivers. Therefore, this study aimed to present a method of constructing a meandering channel comprised of two 180-degree bends. Experimental channels in a meandering shape with a steel structure and glass walls have less often been considered and constructed. Among the many prominent features of this channel are its being 1 meter wide and long and having consecutive 180-degree bends Moghaddassi et al. [37,38].

Patel and Kumar [39] employed a glass flume measuring 17.2 meters in length, 1 meter in width, and 0.72 meters in depth for their investigative study. Within the scope of their research, they examined various configurations of spur dikes, specifically T-shaped, L-shaped, and rectangular designs. Additionally, Pradhan et al. [40] utilized a T-shaped spur dike in their research to analyze alterations in the topography of the bed.

This study presented a comprehensive examination of the technical and lesser-known aspects pertaining to the construction and installation of meandering channels, which are certainly of significant interest to river engineers. In the following, the stages of constructing a meandering channel will be addressed from the onset to the end , and instances of its applications will be presented. Additionally, it illustrated examples of the application of various river structures, such as bridge piers and spur dikes, … and compared their performance in relation to scouring and sedimentation across different channels. This article presented an analysis of technical and less commonly discussed aspects pertaining to the construction, installation, and operation of meandering channels, which would be of significant interest to professionals in the field of river engineering. The discussion included a comparative evaluation of various structures, such as bridge piers and spur dikes, in relation to their functionality in different channel contexts, particularly concerning scouring and sedimentation processes.

2. Process of Meandering Channel Construction and Implementation

This section first introduces the meandering channel properties and then addresses the stages of its construction and setup.

2.1 Meandering Channel Properties

Beginning with the upstream side, this meandering channel is comprised of an 8-meter-long straight path, two consecutive 180-degree bends, and another 8-meter-long straight path downstream. The bends have an outer curvature radius of 4 meters, and considering the 1-meter-wide channel, their relative curvature radius is 3.5. The bed is made of steel, and the channel has 0.8-meter-high walls made of shatter-proof security glass with a thickness of 10 millimeters. A reservoir with a length of 2 meters, a width of approximately 1 meter, a height of 85 centimeters, and a volume of 1700 liters is implemented at the channel entrance on five pillars. To adjust the flow depth in the channel, a butterfly gate is used at the end of the straight downstream path

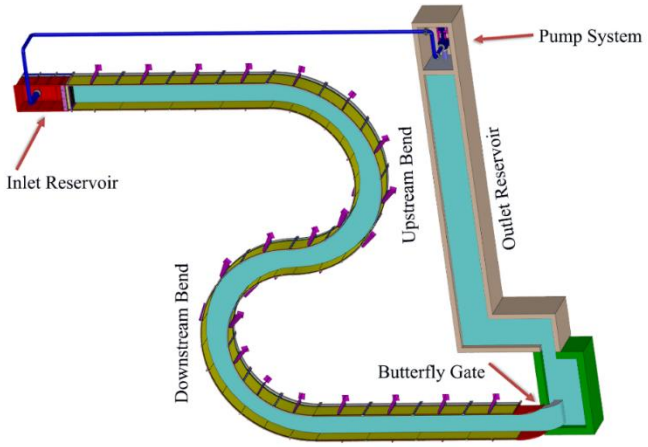
Moghaddassi et al. [37].

The outlet reservoir is made of concrete and is 15 meters long, which transfers water to the inlet reservoir with the pump set up at its end. Figure 1 illustrates a 3D model along with the construction of the real model.

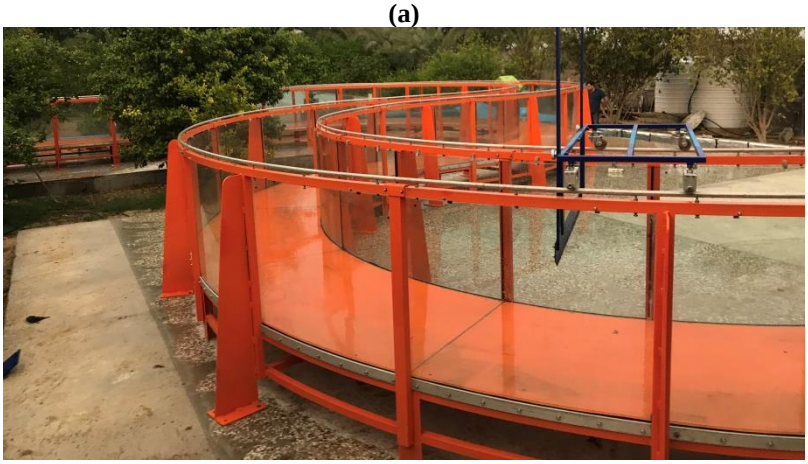
2.2 Meandering Channel Construction Stages

2.2.1 Designing and Preparing the Ground

Prevention of potential ground subsidence under the influence of the applied loads requires implementing a proper and reinforced substructure. A concrete substructure with a thickness of 20 cm and a mosaic pavement was used to reinforce the present bed. In order to determine the control points and install the channel at the precise location, a Leica Total Station camera was used.



(a)



(b)

Figure 1. A 3D view of the channel: a) a schematic view and b) a real picture in the laboratory

2.2.2 Structural Design

Solid work and Sap2000 software programs helped design the structure. The channel's main structure consists of 20 parts with a length of 2 meters, a width of 1 meter, and a height of 80 centimeters, and each 2-meter-long part is located on five pillars. The required steel for constructing every part of the channel was considered to be ST37 with a yield strength of 2400 kg/cm^2. The loads from different sections, including the glass, the water, and the filler materials made of Sicilian Sand, are considered in the model. Since the internal stress of the structural members is insignificant, the deformations and the maximum deflection of the members are the decisive factors in this analysis. The inlet reservoir and the outlet butterfly gate of the channel have been designed considering a flow rate of 100 L/s.

2.2.3 Designing Pump and Water Supply System

Supply of water to the meandering channel is made possible using Pumpiran 150-200. In this pump, the circle number (n) is 1450, the transferable discharge (Q) is 330 m^3/hr, the head (H) is 9 m, and the power (P) is 15 kw. Due to flow drop on the water transmission pathway, this system allows a transferable discharge up to 100 L/s. Considering the type of electropump employed and the pipes available on the market, an 8-inch-long pipe is used at the inlet suction and a 6-inch-long pipe at the outlet discharge. Considering the discharge pipe harnessed at the structural wall around the channel and the shock proof implemented at the pump outlet, the vibration transfer is controlled through the flow pipe in this channel.

An ultrasonic flowmeter, Altek (Type: TFM3100-F1), is used to determine the flow rate with an accuracy of ±1%. Transducers of this type of flowmeter can be installed in different methods: N, W, Z, or V. The best place to install the flowmeter transducers is a point on the pipeline which is at the maximum distance from the pump inlet, the valve, or any obstacle generating a turbulent flow. In this channel, the transducers are 4 meters away from the pump's outlet area. The minimum upstream distance of the transducers must be five times the pipe's diameter (80 cm), and it is predicted to be 12 meters in this case. Different arrangements of the transducers were tested and controlled. Given the diameter of the discharge pipe, the best choice in this project is the V-method installation. The performance of the ultrasonic flowmeter was evaluated and verified using two different flowmeters. Figure 2 illustrates how the pump, the piping system, and the flowmeter are installed in this channel.

A concrete reservoir with a width of 1 meter, a height of 2 meters, and a length of 15 meters is constructed along the channel to tighten the path of water transmission from the outlet section and pump water to the channel inlet. Construction of this basin includes excavating the site, implementing a concrete slab for the wall and the bed, isolating and waterproofing, implementing the tiles and ceramic, installing a trash capture filter at a distance of 1 meter from the pump inlet, and implementing a concrete slab on the flow path. Figure 3 shows the construction of the outlet reservoir and the water transmission system.

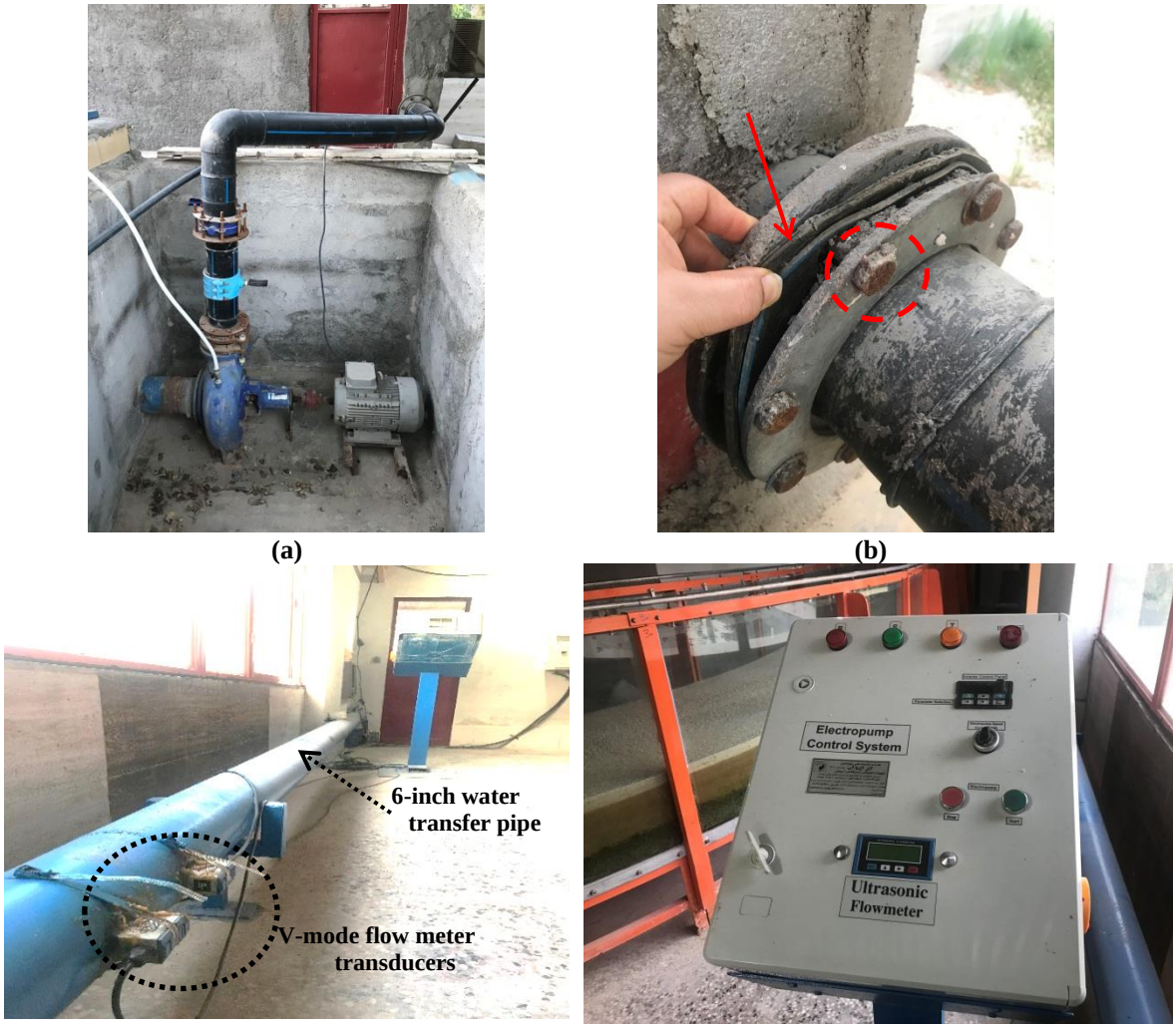


Figure 2. Installation of the pump and the flowmeter: (a) the installed pump, (b) 1- the waterproof rubber O-ring sealing gasket, and 2- bolts and nuts, (c) the flowmeter transducers in V-mode, and (d) the flowmeter control box

2.2.4 Installation of Channel Modules

A 2-meter-long module of the channel structure was first constructed. Then stencils were supplied for making and installing the glass. After testing and verifying the proper and precise connection between the parts, the other parts of the structure and glass were built and assembled in the workshop. After designing and constructing the first module, the other channel modules were built and assembled according to the working drawings. After assembling different modules according to the working drawings and visiting the first module, the installation and the initial test of the glass were done.



Figure 3. Construction of the outlet reservoir and the water transmission system: (a) site excavation, (b) concrete wall implementation, (c) walls and bed waterproofing, (d) bed and body tiling, (e) trash capture filter implementation, and (f) the final concrete cover on the reservoir

Figure 4 illustrates the construction of a part of the structure, the inlet reservoir, the outlet gate, and the initial assembly of the channel in the workshop. After the initial assembly of the whole structure according to the drawings, different channel modules were assembled and moved to the paint workshop. After painting, the modules were prepared to be loaded for implementation at the project site. Figure 5 shows the stages of painting the channel modules.



Figure 4. Construction of the structure and assembly of the first channel in Azar Ashena Ab Co



(a) **(b)**

Figure 5. Stages of painting the channel modules: (a) sanding and removing the rust from the parts and (b) painting

After transferring the modules to the site, the stages of installation and assembly of the channel, including implementation of the 2-meter-long modules and glass, were done according to the working drawings. The heat-resistant sealing paste was used to waterproof the modules. As a waterproofing test, the channel was exposed to a hydrostatic pressure of water for a height of 0.8 meters for 24 hours.

Engine and gear, which could be transported both electrically and manually, were used to adjust the gate, and they were able to move the gate with the precision degree of 1 millimeter. Figure 6 illustrates the different parts of the outlet butterfly gate.



(a) **(b)**

Figure 6. Different outlet gate sections: (a) the gate manual control and (b) the butterfly gate

Using a ¾-inch PVC pipe to prevent the turbulent flow from entering the channel and calm it, a system was designed and implemented as shown in Fig. 7; this set well converted the turbulent inlet flow of the reservoir into a uniform and steady flow in the channel.



(a) **(b)**

(c) **(d)**

Figure 7. How turbulence is controlled and the flow is calmed: (a) installing PVC pipes to control the flow, (b) the flow inlet before turbulence control, (c) the turbulent inlet flow, and (d) the uniform outlet flow through the channel entrance path

2.2.5 Design and Construction of Protective Structures

Structural walls and ceilings were implemented around the channel to protect the channel structure under different weather conditions such as wind and rain, to eliminate the external variables' effect on experimental results, and to provide appropriate moisture and temperature for laboratory conditions.

2.2.6 Implementation of Bed

This channel will host various experiments under both rigid and mobile bed conditions (as shown in Fig. 8). Fig. 8-a depicts the rigid bed, and Fig. 8-b shows the mobile bed filled with Sicilian fine materials. To prevent materials outpour, galvanized sheets function as sloped surfaces at the beginning and the end of the channel's straight paths, as shown in Fig. 8-b.



(a) **(b)**

Figure 8. Channel bed: (a) the rigid bed and (b) the mobile bed along with the galvanized sheets at the beginning and the end of the channel for preventing materials outpour

2.2.7 Designing Other Measuring Devices Related to the Channel and Preparing It to Begin the Tests

To conduct different experiments with respect to scour in this channel, a flattener device was designed and incorporated for leveling the bed, as shown in Fig. 9-a. A 12 gauge galvanized wire was attached to the channel structure throughout the path to allow the bed flattener device to move on it with the help of rollers. Figure 9-b illustrates the device designed for measuring the maximum scour depth during the tests. Figure 9-c shows the bed profiler device for measuring sediment variations and bed scour. Precise point determination will be needed for conducting experiments in the bend. Therefore, as shown in Fig. 10, bend gradation was done using the Total Station camera with a precision of 0.1 mm.

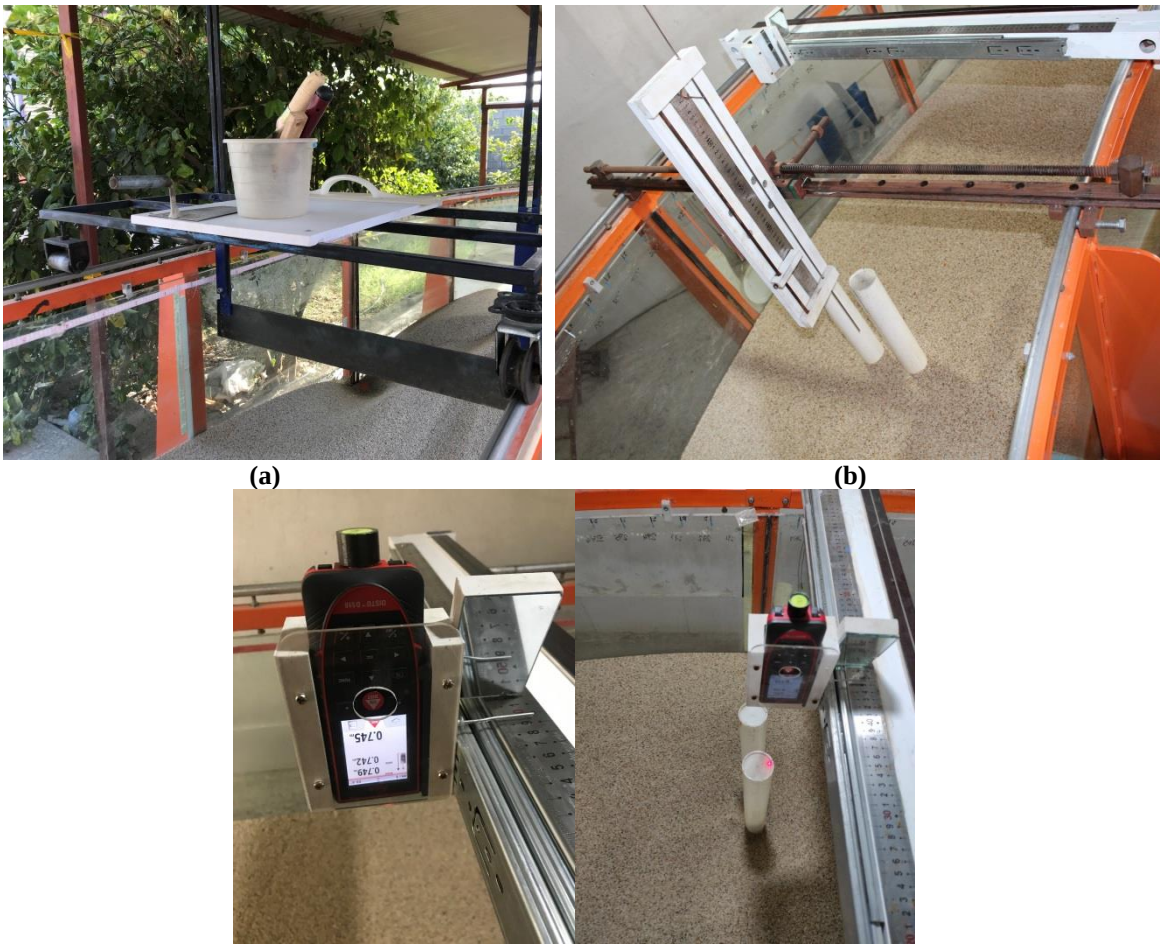


Figure 9. Pieces of equipment used for mobile bed experiments: (a) the bed flattener device, (b) the scour depth measurement device, and (c) the bed profiler used for measuring sediment variations and bed scour

Given the high flow velocity on the straight path following the downstream bend outlet, part of the downstream straight region was made rigid using bricks. To prevent the entrance of particles to the output reservoir, a region was predicted as the sediment intake basin at the end of the straight path (Fig. 11). Application of this method could be useful, particularly at channels with a small length with the possibility of particles entering the pump suction area.



Figure 10. Bend gradation using the Leica Total Station camera



Figure 11. Creating a sediment intake basin at the end of the downstream straight path to prevent sediment from entering the outlet reservoir

3. Applications of Hydraulic Structures in the Meandering Channel

As previously explained, it is possible to carry out different experiments regarding river engineering and different relevant hydraulic structures in this laboratory. Submerged vanes, T-shaped spur dikes, bridge piers Dehghan et al. [41], gates, and spillways Parsaie et al. [42] are instances of such structures that were introduced and analyzed in this study.

In this section, all experiments were performed under incipient motion conditions with a discharge of 70 liters per second and a water depth of 17 cm at the inlet of the upstream bend (except for experiments with a spillway). In addition, the duration of 4 hours was considered as the equilibrium time for all experiments. The channel bed was filled with uniform silica with a thickness of 30 cm. The average particle diameter (d_{50}) was equal to 1.85 mm and its standard deviation was equal to 1.2.

3.1 Effect of Submerged Vanes

Using submerged vanes is one of the methods which gain the researchers' attention to reduce bridge pier scour or protect the outer wall of bends against erosion. Figure 12 illustrates submerged vanes placed at the outer bend of a meandering channel.



Figure 12. Application of submerged vanes at the outer bend of a meandering channel

As can be seen in this figure, submerged vanes are thin rectangular structures created due to having a streamwise angle, and a high-pressure and low-pressure region on both sides. Moreover, these structures cause secondary vortices, change the flow pattern in the riverbed and, as a result, change sediment transport and scour. For this reason, it is highly important to study the bed topography variations around them. Figure 13 shows these changes in the meandering channel under the presence of these three vanes. These vanes are made of Plexiglas with a thickness of 1 cm and a width of 7.5 cm. They are spaced 7.5 cm apart at a 25-degree angle, so that they are located at the 180-degree angle of the first external bend, with the center of the vanes being 10 cm away from the edge of the external bend. The water height over the vanes is 8 cm and their submergence ratio is 50%.

As shown in Fig. 13, with the submerged vanes placed at the junction between the two bends, a scour hole is developed at a distance of 5% of channel width from the end of the upstream bend outer wall and the beginning of the downstream bend inner wall. This maximum value in the upstream bend was 17.6 cm, which occurred at the 178.5-degree angle, while changes in other parts of the first bend were too small. These trivial changes in the upstream bend were also reported with no hydraulic structures in this channel Moghaddassi et al. [38]. In the downstream bend, sedimentary piles were observed near the inner wall of the downstream bend from the 290-degree angle onward, extended toward the mid-channel. The maximum sedimentation along the path was 11.9 cm in the downstream bend and at a distance of 60% of the channel width within

the range of 355 to 358 degrees. In addition, two maximum scour holes were observed near the inner and outer walls in this bend. According to the figure, it can be seen that the first hole is skewed from the 210-degree angle to the mid-channel and is drawn to the outer bank up to the 300-degree angle. In this case, the maximum scour hole depth was equal to 18.5 cm at the 358-degree angle and at a distance of 5% of the channel width from the outer wall. Another scour hole with a depth of 17.9 cm was also observed at the 182-degree angle at a distance of 5% of the channel width from the inner wall of the downstream bend.

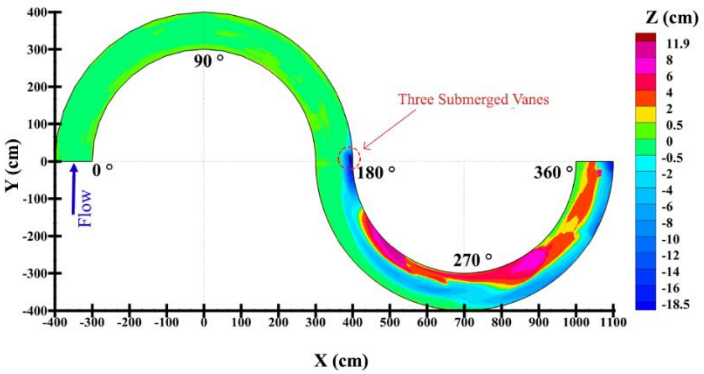


Figure 13. Bed topography variations in the meandering channel equipped with submerged vanes

Upon analysis of the two scenarios involving the application of submerged vanes in front of a single pier positioned at an angle of 180 degrees within the meandering channel, compared to a single pier without such vanes, it was observed that the maximum scour depth around the bridge pier, when utilizing the submerged vanes in conjunction with the single pier, was approximately reduced by 10%.

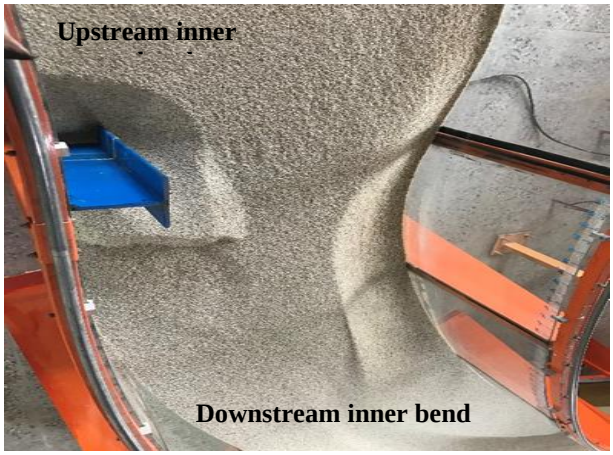
In alignment with the findings presented in this study, Odgaard and Wang [43] similarly demonstrated that submerged vanes serve effectively in safeguarding riverbanks against erosion and enhancing drainage efficiency at culverts and bridge crossings. Furthermore, the research conducted by Ouyang et al. [44] indicated that the sediment management capacity within a complex arrangement of three submerged vanes positioned in a sequential manner decreased as the spacing between the vanes is reduced.

In their study, Safaripour et al. [45] examined the impact of submerged vanes immersion ratios on the scour hole slope surrounding pier groups situated within a sharp bend channel. The findings of this research indicated that submerged vanes had the most influence in the reduction of the upstream slope, particularly in scenarios involving a single pier, when the vanes were submerged by 75% in conjunction with triad longitudinal piers featuring a 25% immersion, where a reduction of about 50% and 74% in scour slope was observed, respectively, in comparison to piers that were not equipped with vanes.

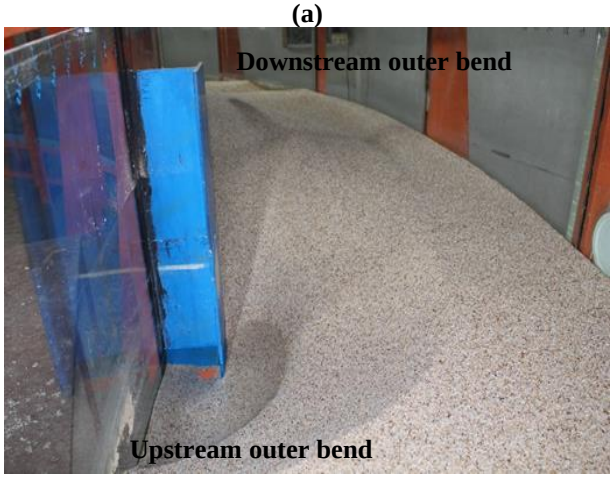
An analysis of the research findings of Chooplou et al. [46] indicated that when the pier was oriented at a 90-degree angle within a sharp 90-degree bend, the maximum scour reduction occurred with the implementation of submerged vanes positioned at a distance of 2.5 times the pier diameter from the centerline of the pier, as well as at distances of 1 and 1.5 times the pier diameter. This arrangement resulted in a 30% and 25% decrease in local scour around the bridge pier.

3.2 Effect of T-shaped Spur Dike

Numerous researchers have shown interest in studying the behavior of rivers while using spur dikes to protect the walls against erosion, Bora and Kalita [47]. Since T-shaped spur dikes have the least amount of scour and the best performance in protecting river walls against erosion among spur dikes of different geometries Vaghefi et al. [15], Akbari et al. [34], this type of spur dike was selected to be used in this study. Figure 14 illustrates an instance of the bed variations in the meandering channel while using a T-shaped spur dike at the 180-degree angle of the upstream inner and outer bends. These impermeable spur dikes are made of Plexiglas with a thickness of 1 cm and a wing and web length of 15 cm under non-submerged conditions. These dimensions were selected based on the recommendations of Ghodsian and Vaghefi [13].



(a)



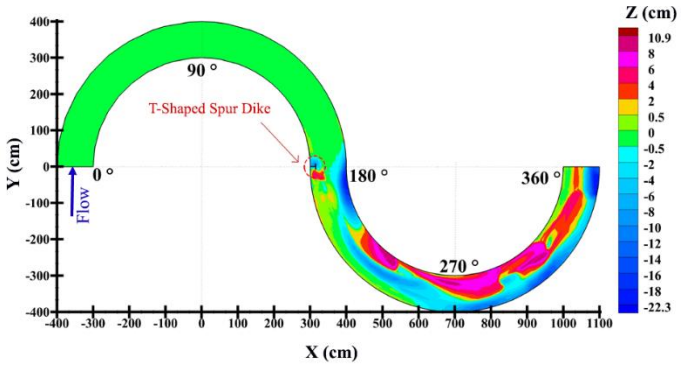
(b)

Figure 14. Bed variations with the T-shaped spur dike installed at the 180-degree angle: (a) the upstream inner bend and (b) the upstream outer bend

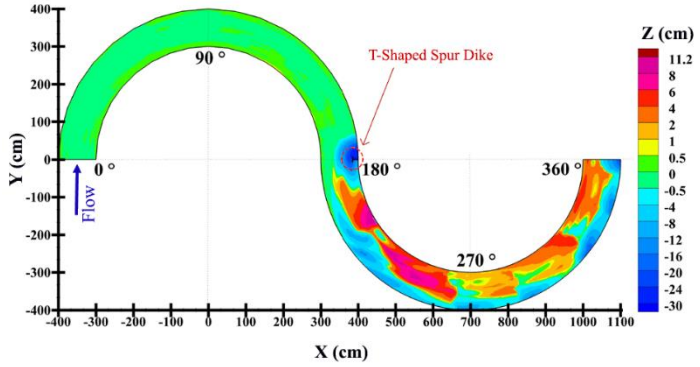
Figure 15 shows the effect of the T-shaped spur dike installed perpendicular to the inner and outer walls of the upstream bend on bed topography variations of the meandering channel. According to Fig. 15-a, it can be seen that the maximum scour depth, equal to 22.3 cm, at a distance of 5% of the channel width from the outer bank of the downstream bend occurs within the 353-degree angle. The maximum scour around the spur dike, equal to 11.1 cm, was also

observed at the 179-degree angle near the inner wall of the upstream bend. The maximum sedimentation height in this case, equal to 10.9 cm, occurred within the range of 233 to 236 degrees of the inner wall of the downstream bend.

The findings from the research conducted by Ghodsian and Vaghefi [13] regarding the impact of T-shaped spur dikes in a 90-degree channel bend on alterations in bed topography indicated that the extent of scouring occurring upstream of the spur dike was significantly greater than that experienced downstream. This observation was confirmed by the results of the current study.



(a)



(b)

Figure 15. Bed topography variations of the meandering channel bed with the installation of a T-shaped spur dike at the 180-degree angle: (a) the upstream inner bend and (b) the upstream outer bend

This is because the duration of the experiments was initially predicted to be 4 hours, but in the case of the spur dike installed at the outer wall (Fig. 15-b), the maximum scour around the web and wing of the spur dike was skewed toward upstream after 2.5 hours into the experiment. According to this figure, it is observed that the maximum scour depth, equal to 30 cm, occurs at a distance of 10% of the channel width from the outer bank of the upstream bend at the 179-degree angle. The maximum scour depth in the downstream bend, equal to 21.5 cm, occurred at a distance of 10 to 20% of the channel width from the inner bank of this bend and at the 181-degree angle. The maximum sedimentation height, equal to 11.2 cm, was reported at the 212-degree angle and close to the inner wall of the downstream bend.

Comparison of these two figures indicates that the maximum scour near the spur dike, with

the spur dike located in the external bend, is 2.7 times greater than its position in the upstream internal bend. By repositioning the T-shaped spur dike to a 180-degree angle from the outer bend to the inner bend, an increase of nearly 35% was observed in the maximum scour within the bend.

In the study conducted by Tripathi, Pandey [48], an in-depth examination was performed regarding the local scour phenomena surrounding T-shaped spur dikes positioned at various locations along the external bend of a meandering channel. Their tests were executed within a meander characterized by a rectangular cross section, featuring two successive bends arranged in reverse order, each measuring sharp 180 degrees with a relative radius of 1. The channel width was also set at 1.0 units with the central radius of both bends equal to 1.0 meters, specifically designed for this purpose. Notably, both the bottom and walls of the rectangular channel were constructed using impermeable cement material. A bed sediment layer with a thickness of 0.25 meters, exhibiting a mean particle diameter of 2 millimeters and a standard deviation of 1.8 millimeters, was uniformly distributed throughout the channel. The spur dike was constructed from a perspex sheet with a thickness of 10 millimeters and a height of 200 millimeters, positioned perpendicular to the curve of the flume bend. The length of the spur dike wing was typically considered to be 20% of the channel's width (200 millimeters); however, for the purposes of this study, this ratio was adjusted to 15% of the channel's width (150 millimeters). The findings of this research indicated that the extent of local scour surrounding the spur dike was positively correlated with both the Froude number and the positions along the meandering pathway from the entrance to the bends. Furthermore, the transition stage (curvy region) exhibited a clear and stable configuration when assessed at an angle of 30 degrees. Conversely, as the spur dike was positioned nearer to the conclusion of the initial bend, the transition stage became sharper or more unstable.

3.3 Effect of Bridge Pier

Bridge piers represent one of the most practical and important structures utilized in rivers, the failure of which causes many casualties and financial losses annually. Figure 16 shows an example of bed topography variations at the site of a single cylindrical pier in the laboratory. A PVC pipe with a diameter of 6 cm was used to represent the pier ,based on the recommendation of Chiew and Melville [4], which was placed at the 180-degree angle.



Figure 16. Installation of a cylindrical bridge pier in a laboratory channel and bed variations near it

Bed topography variations along the whole meandering path and around this pier are presented in Fig. 17. According to this figure, the maximum scour depth around the bridge pier is reported to equal to 10.8 cm, while the maximum sedimentation height, equal to 11.1 cm, occurs at a distance of 5% of the channel width from the inner bank of the downstream bend within the range of 235 to 245 degrees. The maximum scour depth in the channel also occurred affected by the bend geometry at 5% of the channel width from the outer bank of the downstream bend and at the 348-degree angle equal to 16.1 cm (1.49 times the maximum scour around the pier). Different parameters (change of position, geometry, angle, flow conditions, etc.) in relation to bridge pier and bridge pier influence on bed topography variations have their effects, which have received less discussion regarding meandering channels.

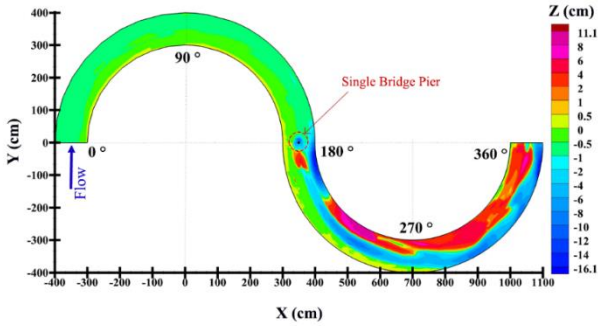


Figure 17. Bed topography variations of the meandering channel with the installation of a cylindrical bridge pier.

Upon examination of the findings presented by Moghaddassi et al. [49] concerning a meandering channel, it became evident that in the downstream bend, from the inception to the midpoint of the bend, there was a discernible trend of increasing maximum scour at the pier, which paralleled the observations made in the upstream bend. However, commencing from the angle of 315 degrees, a diminishing trend was noted. Specifically, there was a significant reduction of approximately 90% in the maximum scour at the pier as the angle was changed from 270 degrees to 315 degrees.

Asadollahi et al. [50] conducted a numerical and experimental analysis of the flow dynamics and scour patterns surrounding both individual and grouped bridge piers within a sharp 180-degree bend. The findings from their research revealed that the maximal scour depth and sedimentation height associated with the bend with a single pier were found to be 3.4 and 1.8 times the pier diameter, respectively. Furthermore, a comparative assessment of the current study's outcomes indicated that, for a U/UC ratio of 0.98 and the positioning of the single pier at 90 degrees of the mild bend, the maximum scour approximately equated to 2.1 times the pier diameter.

The study conducted by Sedighi et al. [51] on a single bend channel featuring a sharp 180-degree bend indicated that, in scenarios without a pier, the highest level of scour was observed from angles ranging from 40° to 80°, specifically at a location 20% of the channel width from the inner bank. Conversely, in the present research, due to the relatively mild 180° bend, no significant alterations were detected during the same timeframe in this region. Instead, the most pronounced scouring was identified at the end of the 180° bend at the junction with the downstream section.

According to the results presented by Sedighi et al. [51], Keshavarz et al. and Dehghan et al. [52], it was observed that within a sharp 180-degree bend, the maximum sediment height at the pier location exceeded that recorded at 90 and 120 degrees for all pier shapes. Conversely, in the current study, focusing on a mild 180-degree bend, it was determined that for a single pier positioned at an angle of 135 degrees, the maximum sedimentation surpassed that at 90 degrees, which in turn exceeded that at 45 degrees. Notably, within the mild bend under consideration, variations in pier position throughout the bend indicated that the maximum sedimentation observed in the latter half of the bend was greater than that in the initial half.

3.4 Effect of Gate

Figure 18 illustrates the gate in the meandering channel. The effect of parameters on bed variations can be analyzed by altering the water depth beneath the gate and the positioning at different points in the meandering channel.

In this figure, the gate is placed at the 176-degrees angle and the upstream bend, so that it is 3.5 cm away from the channel bed material at the onset of the test. Bed topography variations with the installation of the gate in the meandering channel are shown in Fig. 19. In this case, under the presence of the gate in the channel, the maximum scour depth occurred at the gate site after 1.5 hours into the experiment. This figure shows that the maximum scour depth, equal to 30 cm, occurs within the range of 10% of the channel width from the outer wall of the upstream bend at the 178-degree angle, and continues up to 5% of the inner wall of the downstream bend at the 181-degree angle. The maximum sedimentation height was equal to 18.2 cm at the 232-degree angle at mid-channel and at the 247-degree angle at a distance of 20% of the channel width from the outer wall of the downstream bend. This was the highest amount of sedimentation observed under the influence of the structures used in this study.



Figure 18. Installing a gate at the meandering path

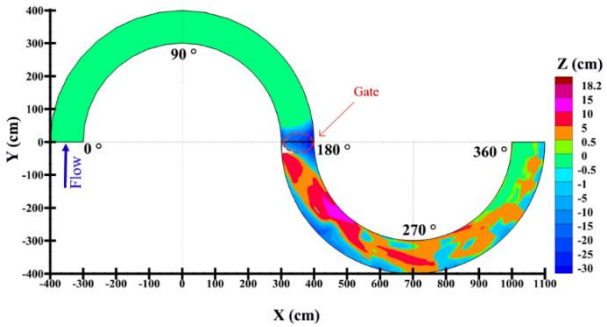


Figure 19. Bed topography variations of the meandering channel with the installation of the gate

3.5 Effect of Wide-Edged Spillway

Figure 20 illustrates the installation of a wide-edged spillway at the junction of two meandering channel bends. This spillway is 16 cm wide and installed at a 180-degree angle. The discharge in this test is 30 liters per second and the water depth in the direct upstream direction is 16 cm. The depth changes were such that the water depth was 16 cm at the upstream bend entrance, 15.5 cm at the end of the upstream bend before the spillway, 6 cm at the beginning of the spillway edge, and 4 cm at the spillway outlet. Test duration was 4 hours, as in other tests.

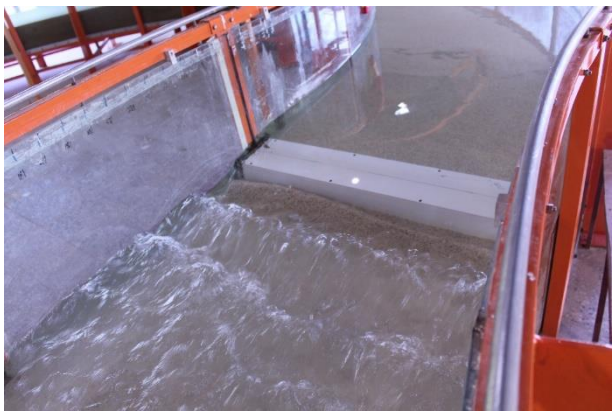


Figure 20 Installation of the wide-edged spillway in the meandering channel

Figure 21 indicates bed topography variations along the meandering channel in the presence of the wide-edged spillway. The maximum scour depth at the upstream bend, equal to 3 cm, occurred near the outer wall at the 174-degree angle, while that at the downstream bend, equal to 10.2 cm, occurred at the 194-degree angle near the outer wall. The maximum sedimentation height, equal to 5.4 cm, happened at a distance of 5% of the channel width from the inner wall of the downstream bend at the 200-degree angle. As can be seen in this figure, from the 230-degree angle of the downstream bend to the end of the bend, there are no significant changes in bed topography.

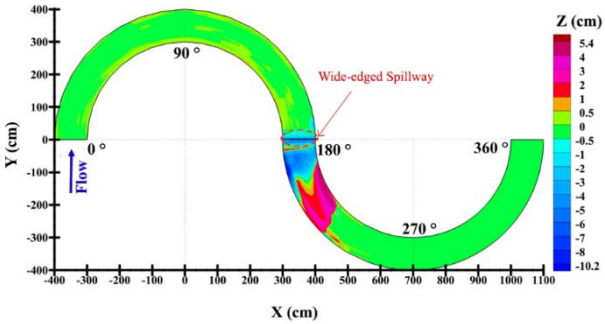


Figure 21. Bed topography variations of the meandering channel with the wide-edged spillway installed

3.6 Effect of Sharp-Edged Spillway

Figure 22 depicts the installation of a sharp-edged spillway with a thickness of 16 mm (0.1 times the width of the wide-edged spillway) at the junction of the two bends. In this case, as in the previous case, the discharge is 30 liters per second and the water height over the spillway is 5 cm.

Figure 23 shows bed topography variations around the sharp-edged spillway with other parts of the channel for comparison. As can be seen, the maximum scour depth, equal to 14.3 cm, occurred in the channel at the 226-degree angle and at the outer wall of the downstream bend, while this maximum value occurred around the spillway at the 181-degree angle with a height of 12.2 cm. The maximum sedimentation height began at a distance of 10 to 20% of the channel width from the inner wall of the downstream bend and reached a height of 5.4 cm towards the outer wall at the 224-degree angle.



Figure 22. Installation of the sharp-edged spillway in the meandering channel

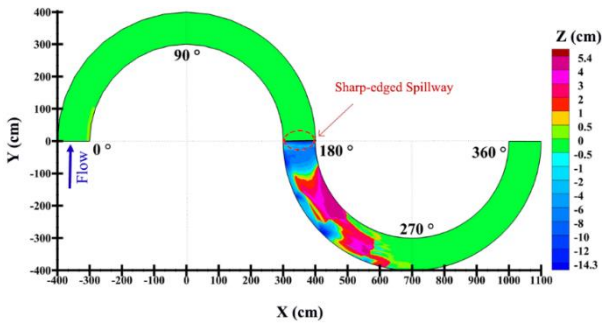


Figure 23. Bed topography variations of the meandering channel with the sharp-edged spillway

Comparison of Fig.21 and Fig.23 indicated that if this sharp-edged spillway is used with a ratio of 0.1 times the width of the wide-edged spillway, the maximum sedimentation height along the path remains constant. With both spillways, under the influence of bend geometry, the maximum scour depth took place near the outer bank of the downstream bend. Furthermore, implementing a sharp edge Spillway instead of a wide edge at the junction of the two bends resulted in a maximum scour increase of approximately 40%.

As mentioned above, these are merely examples presented here on the use of these structures in a meandering channel. In fact, for more extensive and practical research, the combination of these structures can be used to study the flow status and changes in bed topography in a meandering channel to examine the interaction effect of these structures.

4. Conclusions

Considering the importance of investigating meandering rivers' behavior, a meandering, double-bent channel was designed and constructed. This channel comprises a straight path upstream, two consecutive 180-degree bends, and another straight path downstream. The circular flow system is developed by the pump and the side reservoir attached along the channel, and a semi-automatic system controls this flow. Further, a butterfly gate implemented at the channel outlet is responsible for adjusting the flow properties. In addition to the stages of designing and constructing this channel, this study presented instances of performance of different hydraulic structures, including a T-shaped spur dike, a gate, a sharp-edged and a wide-edged spillway, a bridge pier, and submerged vanes installed in the channel, and their effect on meandering paths. All these experiments were performed under incipient motion conditions. A summary of the most important results is as follows:

- Installation of submerged vanes created two maximum scour holes near the inner and outer walls of the downstream bend. These maximum values were 17.9 and 18.5 cm occurring at 182 and 358-degree angles, respectively.
- The maximum scour around the T-shaped spur dike in the external bend was 2.7 times greater than that around this spur dike in the internal bend.
- The maximum scour in the channel, with the cylindrical pier placed in it, was equal to 16.1 cm, which was 1.49 times the maximum amount of scour around the pier itself.
- The highest amount of sediment bars observed in the channel, equal to 18.2 cm, was associated with the condition in which the gate was implemented.

- In the sharp-edged spillway experiment, the maximum scour depth increased by approximately 40% compared to the wide-edged spillway experiment.
- As witnessed here, the different hydraulic structures will have different effects on river bed topography variations. Predicting the behavior of rivers under the influence of different structures using experimental results will help reduce the damage caused by implementing those structures in reality.

Statements and Declarations
The authors declare that they have no conflict of interest.

Competing Interests
This research work is not supported by any funding agency.

Financial Disclosure Statement
The author(s) received no specific funding for this work.

Funding
This research did not receive any specific grant from funding agencies in the public, commercial, or not-for-profit sectors.

Authors' contributions
N.M: flume construction, preparation of material, performing laboratory tests, collecting data, preparing graphical illustrations, and the first draft of the manuscript. M.V: flume designer, Methodology, collecting data, data analysis and editing of manuscript. All authors reviewed the manuscript.

Data Availability
The data presented in this study are available on request from the corresponding author.

Consent for Publication
All the authors have read and agreed to the submitted version of the manuscript.

Acknowledgments
The authors would like to express their most sincere gratitude to **Azar Ashena Ab & Pumpiran Co** as they cooperated in different construction stages of this channel.

References

1. Akbari M, Vaghefi M, (2017). Experimental investigation on streamlines in a 180º sharp bend. Acta Sci Tech 39:425-432. https://doi.org/10.4025/actascitechnol.v39i4.29032
2. Peakall J, Ashworth P, Best J, (1996). Physical modelling in fluvial geomorphology: principles, applications and unresolved issues. The Scientific Nature of Geomorphology. Wiley, New York.
3. Raudkivi AJ, Ettema R, (1983). Clear-water scour at cylindrical piers. J Hydraul Eng 109:338-350. https://doi.org/10.1061/(ASCE)0733-9429(1983)109:3(338)
4. Chiew YM, Melville BW, (1987). Local scour around bridge piers. J Hydraul Res 25:15-26. https://doi.org/10.1080/00221688709499285
5. Chiew YM (1992). Scour protection at bridge piers. J Hydraul Eng 118:1260-1269. https://doi.org/10.1061/(ASCE)0733-9429(1992)118:9(1260)
6. Shakibaeinia A, Tabatabai MRM, Zarrati AR, (2010). Three-dimensional numerical study of flow structure in channel confluences. Can J Civil Eng 37: 772-781. https://doi.org/10.1139/L10-016
7. Nazari-Giglou A, Jabbari-Sahebari A, Shakibaeinia A, Borghei SM, (2016). An experimental study of sediment transport in channel confluences. Int J Sediment Res 31:87-96. https://doi.org/10.1016/j.ijsrc.2014.08.001
8. Vaghefi M, Ghodsian M, Salimi S, (2016). The effect of circular bridge piers with different inclination angles toward downstream on scour. Sadhana 41:75-86. https://doi.org/10.1007/s12046-015-0443-x
9. Wang H, Zhou G, Shao X, (2010). Numerical simulation of channel pattern changes Part I: Mathematical model. Int J Sediment Res 25:366-379. https://doi.org/10.1016/S1001-6279(11)60004-8
10. Yagci O, Celik M.F, Kitsikoudis V, Kirca VO, Hodoglu C, Valyrakis M, Duran Z, Kaya S, (2016). Scour patterns around isolated vegetation elements. Adv Water Resour 97:251-265. http://dx.doi.org/10.1016/j.advwatres.2016.10.002
11. Chavan R, Kumar B, (2017). Experimental investigation on flow and scour characteristics around tandem piers in sandy channel with downward seepage. J Mar Sci Appl 16:313-322. https://doi.org/10.1007/s11804-017-1426-6
12. Zou X, Wang C, Song H, Han Z, Ma Z, Hu W, (2018). Applications of ultrasound imaging system for measuring water-sand parameters during sediment transport process in hydraulic model experiments. J Hydroinform 20:410-423. https://doi.org/10.2166/hydro.2017.025
13. Ghodsian M, Vaghefi M, (2009). Experimental study on scour and flow field in a scour hole around a T-shape spur dike in a 90 bend. Int J Sediment Res 24:145-158. https://doi.org/10.1016/S1001-6279(09)60022-6
14. Vaghefi M, Ghodsian M, Akbari M, (2017). Experimental investigation on 3D flow around a single T-shaped spur dike in a bend. Period Polytech-Civ 61:462-470. https://doi.org/10.3311/PPci.7999
15. Vaghefi M, Ghodsian M, Neyshabouri SAAS, (2012). Experimental study on scour around a T-shaped spur dike in a channel bend. J Hydraul Eng 138:471-474. https://doi.org/10.1061/(ASCE)HY.1943-7900.0000536
16. Wang H, Tang H, Liu Q, Wang Y, (2016). Local scouring around twin bridge piers in open-channel flows. J Hydraul Eng 142:06016008. https://doi.org/10.1061/(ASCE)HY.1943-7900.0001154
17. Abdolahpour M, Yasi M, Behmanesh J, Vaghefi M, (2011). Construction of a concrete bend channel as a hydraulic model. Adv Natural Appl Sci 5:34-40.

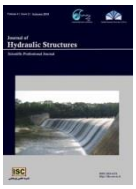
18. Dugue V, Blanckaert K, Qiuwen CHEN, Schleiss AJ, (2013). Reduction of bend scour with an air-bubble screen–morphology and flow patterns. Int J Sediment Res. 28, 15-23. https://doi.org/10.1016/S1001-6279(13)60014-1
19. Khosronejad A, Hill C, Kang S, Sotiropoulos F, (2013). Computational and experimental investigation of scour past laboratory models of stream restoration rock structures. Adv Water Resour 54:191-207. https://doi.org/10.1016/j.advwatres.2013.01.008
20. Moharana S, Khatua KK, (2014). Prediction of roughness coefficient of a meandering open channel flow using Neuro-Fuzzy Inference System. Measurement 51:112-123. https://doi.org/10.1016/j.measurement.2014.01.026
21. Termini D, (2015). Momentum transport and bed shear stress distribution in a meandering bend: Experimental analysis in a laboratory flume. Adv Water Resour 81:128-141. https://10.1061/ASCEHY.1943-7900.0000046
22. Binns AD, da Silva AMF, (2015). Meandering bed development time: Formulation and related experimental testing. Adv Water Resour 81:152-160. https://doi.org/10.1016/j.advwatres.2014.11.007
23. Mera I, Franca MJ, Anta J, Peña E, (2015). Turbulence anisotropy in a compound meandering channel with different submergence conditions. Adv Water Resour 81:142-151. https://doi.org/10.1016/j.advwatres.2014.10.012
24. Pagliara S, Kurdistani SM, Palermo M, Simoni D, (2016). Scour due to rock sills in straight and curved horizontal channels. J Hydro-Environ Res 10:12-20. https://doi.org/10.1016/j.jher.2015.07.002
25. Liu C, Shan Y, Liu X, Yang K, Liao H, (2016). The effect of floodplain grass on the flow characteristics of meandering compound channels. J Hydrol 542:1-17. http://dx.doi.org/10.1016/j.jhydrol.2016.07.037
26. Akhtari AA, Seyedashraf O, (2018). Experimental and numerical investigation on vanes' effects on the flow characteristics in sharp 60° bends. KSCE J Civ Eng 22:1484-1495. https://doi.org/10.1007/s12205-017-1743-y.
27. Vaghefi M, Akbari M, (2019). A procedure for setting up a 180-degree sharp bend flume including construction and examinations with hydraulic structures. Sci Iran Trans A 26:3165-3180. https://doi.org/10.24200/sci.2018.5033.1054
28. Moghanloo, M., Vaghefi, M., Ghodsian, M. et al. (2024). The influence of collar parameters on local scour mechanism around the circular pier at the bend. Appl Water Sci 14, 194 https://doi.org/10.1007/s13201-024-02257-5
29. Keshavarz, A., Vaghefi, M. & Ahmadi, G. (2024). Collars for Scour Reduction Around Different Shapes of Bridge Piers in a 180° Sharp Bend. Int J Civ Eng 22, 1733–1751. https://doi.org/10.1007/s40999-024-00994-x
30. Solati S, Vaghefi M, & Ahmadi G, (2023). Scour pattern around a pier in a 180° sharp bend: influence of pier shape under unsteady currents. Hydrological Sciences Journal, 68(12), 1711-1723.
31. Vaghefi, M, Zarei, E, Ahmadi, G, Behroozi, A. M, (2023). Experimental analysis of submerged vanes' configuration for mitigating local scour at piers in a sharp bend: Influence of quantity, length, and orientation, Ocean Engineering, Volume 289, Part 1, 2023, 116267, ISSN 0029-8018, https://doi.org/10.1016/j.oceaneng.2023.116267.
32. Keshavarz, A., Vaghefi, M. & Ahmadi, G, (2022). Effect of the Shape and Position of the Bridge Pier on the Bed Changes in the Sharp 180-Degree Bend. Iran J Sci Technol Trans Civ Eng 46, 2449–2467 .https://doi.org/10.1007/s40996-021-00787-5
33. Sedighi, F., Vaghefi, M. & Zarei, E, (2022). Experimental investigation of flow pattern at

180° bend with rigid bed in effect of twin convergent bridge piers. J. Eng. Appl. Sci. 69, 58 https://doi.org/10.1186/s44147-022-00110-7
34. Akbari M, Vaghefi M, Chiew YM, (2021). Effect of T-shaped spur dike length on mean flow characteristics along a 180-degree sharp bend. J Hydrol Hydromech 69:98-107. https://doi.org/10.2478/johh-2020-0045
35. Park SW, Ahn J, (2019). Experimental and numerical investigations of primary flow patterns and mixing in laboratory meandering channel. Smart Water 4:1-4. https://doi.org/10.1186/s40713-019-0016-y
36. Serajian MT, Kamanbedast AA, Masjedi A, Heidarnejad M, Hasonizadeh H, (2020). Laboratory evaluation of the combined effect of convergence and submerged vanes on lateral Intakes' sediment input at 90° river bends. Ain Shams Eng J 11:245-252. https://doi.org/10.1016/j.asej.2019.09.008
37. Moghaddassi N, Musavi-Jahromi SH, Khosrojerdi A, (2021a). Effect of Duration on Variations in Bed Topography and Water Surface Profile in a Meandering Channel. J Hydraul Struc 7:22-45. https://doi.org/10.22055/jhs.2021.37497.1173
38. Moghaddassi N, Musavi-Jahromi SH, Vaghefi M, Khosrojerdi A, (2021b). Effect of Mean Velocity-to-Critical Velocity Ratios on Bed Topography and Incipient Motion in a Meandering Channel: Experimental Investigation. Water 13:883. https://doi.org/10.3390/w13070883
39. Patel, H. kumar, & Kumar, B, (2024). Experimental study on the optimal spur dike shape under downward seepage. Water Science, 38(1), 172–191. https://doi.org/10.1080/23570008.2024.2321423
40. Pradhan, T. K., Malasani, G. C., Krishna Reddy, S., & Chandra, V. (2024). Investigation on scouring and turbulence characteristics around T-head spur dike. Journal of Applied Water Engineering and Research, 1–16. https://doi.org/10.1080/23249676.2024.2330044
41. Dehghan D, Vaghefi M, Ghodsian M, (2023). Effects of increasing the width of collar on reduction of scouring surrounding the rectangular piers in a 180-degree bend. Appl Water Sci 13:76. https://doi.org/10.1007/s13201-023-01884-8
42. Parsaie A, Shareef SJS, Haghiabi AH, Irzooki RH, Khalaf RM, (2022). Numerical simulation of flow on circular crested stepped spillway. Appl Water Sci 12:215. https://doi.org/10.1007/s13201-022-01737-w
43. Odgaard, A. Jacob, Wang Yalin, (1991). Sediment Management with Submerged Vanes. I: Theory Journal of Hydraulic Engineering, Volume 117, Issue 3, https://doi.org/10.1061/(ASCE)0733-9429(1991)117:3(267)
44. Ouyang, Huei-Tau, Jihn-Sung Lai, Hsin Yu, and Chin-Huang Lu, (2008). Interaction between Submerged Vanes for Sediment Management. Journal of Hydraulic Research 46 (5): 620–27. doi:10.3826/jhr.2008.3160.
45. Safaripour, N., vaghefi, M., Mahmoudi, A, (2024). The influence of the submergence ratio of submerged vanes on the slope of the hole around the pier groups in a sharp bend. *Journal of Hydraulic Structures*; 10(3): 90-118. doi: 10.22055/jhs.2024.46967.1300.
46. Chooplou, C.A., Vaghefi, M. & Akbari, M, (2023). Effect of repositioned submerged vanes on local scour variations around a pier in a bend: experimental investigation. Int. J. Environ. Sci. Technol. 20, 8627–8640 . https://doi.org/10.1007/s13762-023-05031-3
47. Bora K, Kalita HM, (2019). Determination of best groyne combination for mitigating bank erosion. J Hydroinform 21:875-892. https://doi.org/10.2166/hydro.2019.151
48. Tripathi, Ravi Prakash, Pandey, K. K, (2021). Experimental study of local scour around T-shaped spur dike in a meandering channel. Water Supply; 21 (2): 542–552.

doi:https://doi.org/10.2166/ws.2020.331
49. Moghaddassi N, Vaghefi M, Akbari M (2024). Experimental Study: Effects of Pier Position and Critical Velocity Ratio on Scour Pattern in Two Consecutive Bends Under Clear Water Condition. Iran J Sci Technol Trans Civ Eng. DOI: https://doi.org/10.1007/s40996-024-01434-5
50. Asadollahi, M., Vaghefi, M. and Tabibnejad Motlagh, M.J., (2021). Experimental and numerical comparison of flow and scour patterns around a single and triple bridge piers located at a 180-degree sharp bend. Scientia Iranica, 28(1), pp.1-14.
51. Sedighi, F., Vaghefi, M. & Ahmadi, G, (2021). The Effect of Inclined Pair Piers on Bed Topography: Clear Water, Incipient Motion and Live Bed. Iran J Sci Technol Trans Civ Eng 45, 1871–1890 https://doi.org/10.1007/s40996-020-00481-y.
52. Dehghan D, Vaghefi M, Ghodsian M (2021). Experimental study of the effect of the length-to-width ratio and skewness angles of the pier installed at the bend on scour pattern. J Braz Soc Mech Sci Eng 43(3):1–17. https:// doi. org/ 10. 1007/ s40430- 021- 02884-y

© 2024 by the authors. Licensee SCU, Ahvaz, Iran. This article is an open access article distributed under the terms and conditions of the Creative Commons Attribution 4.0 International (CC BY 4.0 license) (http://creativecommons.org/licenses/by/4.0/).

Journal of Hydraulic Structures
J. Hydraul. Struct., 2024;11(2):28-43
DOI: 10.22055/jhs.2024.47806.1319



OPEN ACCESS

Simulation of Tsunami Waves Using Mike 3 Flow Model FM

Vahid Naderkhanloo [1]
Mohammad Hemmati [*1]
Hojjat Ahmadi [1]

Abstract

Tsunamis are a series of ocean waves with exceptionally long wavelengths and can be incredibly destructive when they reach coastal areas. These waves are typically triggered by underwater earthquakes, volcanic eruptions, or landslides. The immense force and energy of a tsunami wave can result in widespread devastation, flooding, and loss of life. It is crucial to comprehend the behavior of tsunami waves in order to develop effective early warning systems and strategies for managing such disasters. Numerical modeling has become a valuable tool for simulating the propagation of tsunamis and the processes of inundation. This research focuses on utilizing the Mike3 Flow Model FM for numerical modeling of tsunami waves. The model was tested using the results of solitary wave theory solutions and basic tsunami wave experiments conducted at the hydraulic laboratory of Changsha University in China. Statistical analysis of the numerical simulation results showed that the Mike3 Flow Model FM can provide accurate calculation of complex tsunami wave flows and deliver important results such as tsunami wave height, wave run-up length, flow volume, and temporal-spatial velocity profiles. Notably, the study observed an improvement in the accuracy of the numerical model as the ratio of wave height to water depth (H/h) decreased. Furthermore, it was confirmed that the accuracy of the numerical model in simulating wave velocity (RMSE $\leq$ 0.14) surpassed its performance in simulating wave surface elevation (RMSE $\leq$ 2.29), compared to experimental data.

Keywords: Tsunami Waves, Numerical Modeling, Mike3 Flow Model FM, Wave velocity, Wave surface elevation.

Received: 21 August 2024; Accepted: 14 September 2024

[*] Email: m.hemmati@urmia.ac.ir (**Corresponding Author**)
[1] Department of Water Engineering, Urmia University, Urmia, Iran.

CC BY

1. Introduction

One way to reduce the damage caused by tsunami waves is to simulate the mechanism of wave formation and propagation in order to predict the magnitude of inundation, overtopping, control, design of flood protection structures, and the impact of wave forces in coastal areas [1, 2]. The results obtained from tsunami wave modeling, such as wave run-up height, wave overtopping from the coastline, volume of water crossing the coastline, flow velocity, and water depth, significantly influence the extent of coastal damage. Controlling each of these factors can be a crucial step in reducing the damage.

Tsunami waves act as shallow-water waves due to their long wavelength even in deep waters [3]. The velocity of tsunami waves decreases as they approach shallow coastal waters, depending on the coastal slope, coastal environment, and existing structures. This reduction in velocity, combined with the constant period and reduced wavelength, leads to an increase in wave height due to phenomena such as shoaling and refraction [4, 5]. Due to their long period and long wavelength, tsunami waves are approximated as a single wave [6, 7]. The single wave has a crest that is entirely above the water surface. Water particles in the single wave move forward and become motionless without returning to complete a full cycle. In comparison to oscillatory waves, the single wave has a transitional state and has unlimited wave length and period, thus remaining unchanged in shape and height at a constant depth over time [8, 9].

Numerous laboratory experiments and numerical models have been conducted to simulate solitary wave behavior. Synolakis [10] measured the maximum wave run-up on the shore for 76 waves of specific heights at constant water depth using a two-dimensional simulation of solitary waves in a rectangular channel with a wave maker at one end. Zelt [11] simulated the breaking of solitary waves in a laboratory experiment conducted in a channel, with a water height of 0.21 meters and a wave height-to-water depth ratio of 0.28. They presented a numerical method for calculating water surface elevation and validated the results with experimental data. Honarmand et al. [12] simulated two-dimensional solitary wave generation on a sloping beach using a numerical method without mesh and exponential basis functions. Honarmand et al. [13] simulated the two-dimensional propagation of solitary waves on a sloping beach using the Flow 3D model and validated the results by comparing them with the experimental data from Synolakis [10] for wave run-up and tsunami wave propagation on a steep coast.

Chen et al. [15] investigated the reflection of solitary waves after colliding with a vertical barrier using high-speed cameras and image processing technology. The researchers conducted numerical modeling based on the experimental results, comparing the accuracy of the numerical modeling with existing theoretical methods. The study by Zaqian et al. [16] focused on the flow structure resulting from the propagation of solitary waves on a thin submerged plate. The impact of the submerged plate angle was examined, revealing additional vortices in experiments with a positive angle, while no vortices were observed for a negative angle. Investigation of clockwise vortices behind the submerged plate indicated a decrease in vortex strength with increasing angles in both directions. Wang et al. [17] conducted a study on the interaction between solitary waves and a vertical submerged wave breaker using a numerically developed method based on constrained interpolation profile (CIP), capable of examining the influence of viscosity. After validation, the impact of the submerged wave breaker on the transmission coefficient of solitary waves was assessed. The researchers concluded that the width of the wave breaker has the least effect on the transient characteristics of solitary wave transmission through a submerged structure, while the height of the wave breaker effectively reduces the transmitted wave height. Finally, comparison of output results from semi-analytical relationships with experimental data and real information from the coasts of Vaticano in Italy indicated acceptable results .

Cavaliere et al. [18] presented a semi-analytical relationship for predicting the location of solitary wave breaking on a sloping beach. They conducted an experimental study to propose this relationship. He et al. [19] focused on investigating the influence of bed roughness on the characteristics of solitary wave transmission in their study. They reported that, contrary to the influence of bed roughness on the shape of solitary waves, the peak of the solitary wave is not significantly affected by the roughness. The effect of solitary waves on a submerged floating tunnel was examined by Zou et al. [20]. In this study, the solitary wave amplitude, distance of the submerged tunnel from the wave rising point, cross-sectional geometry of the tunnel, and relative density of two fluids were considered as the study variable parameters. The results showed that using a parametric cross-section for the submerged tunnel instead of circular and elliptical sections can significantly reduce the wave-induced force. A comprehensive investigation was conducted by Huang and Dong [21] utilizing a numerical model to analyze the dynamic interaction between a solitary wave and a submerged dike. The study focused on examining the influence of the solitary wave height and the dimensions of the dike on various factors such as drag force, flow field characteristics above the dike, and wave transformation features. The researchers identified the presence of two distinct vortexes at the right toe and the lee side of the dike, highlighting these locations as potential sites for scour. In a related study, Huang et al. [22] explored the interaction between solitary waves and emergent rigid vegetation. This investigation involved experimental procedures, with the modified Boussinesq equations employed to simulate the laboratory experiments. Key parameters under scrutiny included wave height, vegetation length, and vegetation density. The researchers derived an empirical expression for the mean drag coefficient and observed a notable increase in maximum wave height immediately prior to the vegetation, while also noting a reduction in wave transmission in the presence of dense vegetative cover.

The utilization of the Mike 3D Flow Model FM has become ubiquitous in the realm of hydraulic engineering due to its ability to accurately simulate a wide array of complex hydraulic phenomena. This powerful computational tool has been effectively employed in various studies to address challenges such as scour, sedimentation, flow pattern, and salinity, among others [23, 24, 25, 26]. In addition, numerous research studies in the literature investigated solitary waves and their characteristics. Despite the widespread usage of the MIKE model in study of the hydraulic of coastal structures, less attention was paid to simulate solitary waves by this model. In the present study, the capability of the model for solitary waves simulation is investigated. The validation of the model is done using experimental data presented by Chen et al. [14]. The results of the present study are used to assessment the MIKE model capabilities in the study of the hydraulic of solitary waves and coastal structures.

2. Materials and Methods

2.1. Numerical model

The MIKE 3D Flow Model FM employs the cell-centered finite-volume method and unstructured flexible mesh to discretize the primitive equations in both Cartesian and Sigma-coordinates. This model is based on numerical solutions for the 3D incompressible Reynolds-Averaged Navier–Stokes equations, incorporating the Boussinesq and hydrostatic pressure assumptions. It includes continuity, momentum, heat, salinity, and density equations for comprehensive simulation of fluid flow [27].

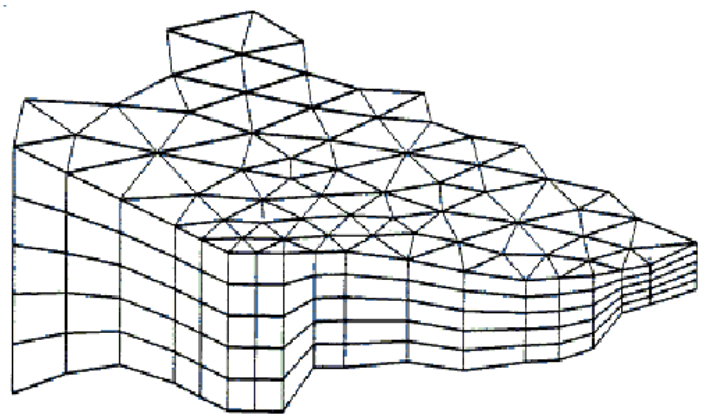


Figure 1. Schematic of unstructured (horizontal direction) and structured (vertical direction) mesh in Mike 3 Flow Model FM [27]

2.2. The governing equations

The continuity and momentum equations in the Cartesian coordinate system are expressed as follows:

The continuity equation is written as:

$$\frac{\partial u}{\partial x}+\frac{\partial v}{\partial y}+\frac{\partial w}{\partial z}=S \tag{1}$$

The momentum equation is written as:

The momentum equation in X direction is written as:

$$\frac{\partial u}{\partial t}+\frac{\partial u^2}{\partial x}+\frac{\partial uv}{\partial y}+\frac{\partial uw}{\partial z}= fv-g\frac{\partial \eta}{\partial x}-\frac{1}{\rho_0}\frac{\partial P_a}{\partial x}-\frac{g}{\rho}\int_z^{\eta}\frac{\partial \rho}{\partial x}dz \tag{2}$$

$$-\frac{1}{\rho_0 h}\left(\frac{\partial s_{xx}}{\partial x}+\frac{\partial s_{xy}}{\partial y}\right)+F_u+\frac{\partial}{\partial z}\left(v_t\frac{\partial u}{\partial z}\right)+u_s S$$

Where t is the time; x, y, and z are the Cartesian coordinates; η is the water surface elevation; d is the still water depth; $h=\eta+d$is the total water depth; u, v, and w are the velocity components in the x, y, and z directions; $f=2\Omega\sin\varphi$ is the Coriolis parameter (Ω is the angular rate of revolution and φ: the geographic latitude); g is the gravitational acceleration; ρ is the water density; S_{xx}, S_{xy}, S_{yx}, and S_{yy} are components of the radiation stress tensor; υ_t is the vertical eddy viscosity; P_a is the atmospheric pressure; and $\rho_0$is the reference density of water. S is the magnitude of the discharge due to point source, u_s and v_s are the velocities of point source in x and y directions, and F_u and F_v are horizontal stress terms.

2.2.1. Turbulence *Models*

Turbulent stress can be modeled based on a concept called eddy viscosity. Eddy viscosity is divided into two types: horizontal eddy viscosity and vertical eddy viscosity. In many numerical modeling approaches, small-scale turbulence cannot be captured by choosing fine spatial discretization. However, this type of turbulence can be accounted for by considering turbulence models.

2.2.2. Vertical eddy viscosity

The viscosity of a vortex is computable based on the logarithmic law (Eq. 3)

.

$$\upsilon_t = U_\tau h\left(c_1\frac{z+d}{h}+c_2\left(\frac{z+d}{h}\right)^2\right) \tag{3}$$

where $U_\tau = max(U_{\tau s}, U_{\tau b})$ and $U_{\tau b}$ and $U_{\tau s}$ are shear of the bed and water surface, as well as the coefficients c_1 and c_2, are 0.41 and -0.41, respectively; h and z represent the water depth and the vertical distance from the bed, respectively.

In the context of the RANS equations for Reynolds stresses, the eddy viscosity plays a crucial role in capturing the turbulent behavior of fluid flow. In the current model, a constant value of 10^{-5} m^2/s has been adopted for the horizontal component of the eddy viscosity. It has been observed that the model's sensitivity to variations in this constant is negligible, indicating a robustness in its predictive capabilities.

2.2.3. Horizontal eddy viscosity

In many cases, the value of horizontal eddy viscosity is considered constant. However, the Smagorinsky relationship expresses turbulence based on characteristic length and deformation ratio, which is a function of flow velocity, as follows:

$$A = c_S^2 l^2 \sqrt{2S_{ij}S_{ij}} \tag{4}$$

$$S_{ij} = \frac{1}{2}\left(\frac{\partial u_i}{\partial x_j}+\frac{\partial u_j}{\partial x_i}\right) \tag{5}$$

Where, c_s is the constant Smagorinsky coefficient; l is a characteristic length; S_{ij} is a deformation ratio and A is a horizontal eddy viscosity value.

2.3. Evaluation of the Numerical Model

Solving the theory of solitary waves

The water surface elevation in solitary waves is determined by solving analytical equations 6 and 7, While the flow velocity is calculated using equation 8 [28, 29].

$$SE(t) = H\sec h^2\left[\left(\frac{3H}{4h}\right)^{1/2}\frac{C}{h}(t-t_{\max})\right] \tag{6}$$

$$C = [g(H+h)]^{1/2} \tag{7}$$

$$u(t) = C\frac{SE(t)}{SE(t)+h} \tag{8}$$

Where, $SE(t)$ is a water surface level, h represents the water level, H denotes the wave height, c stands for the solitary wave velocity, t represents time, t_{max}signifies the wave crest occurrence time, g represents the acceleration due to gravity, and $u(t)$ denotes the water current velocity.

2.4. Numerical Simulation Components

The solution domain on the plane (Figure 2) is discretized using flexible rectangular structured meshes with dimensions of 1 square centimeter per element and 15 uniform vertical layers of the sigma type. In optimizing the mesh dimensions for our study, careful consideration was given to ensure independence from grid sizes and minimize computational time. To achieve this, a series of tests were conducted using both small and large mesh sizes, with the resulting wave velocity fluctuations meticulously recorded. Ultimately, the mesh size yielding the minimum velocity fluctuations was selected for our analysis. In the simulation, the effect of shear stress between water and walls due to the smoothness of the walls, as well as the effect of shear stress between water and air, were not considered. Additionally, in order to ensure numerical stability and accuracy in the results, a Courant number of 1 was chosen, and the simulation was executed with a time step of 0.05 second.

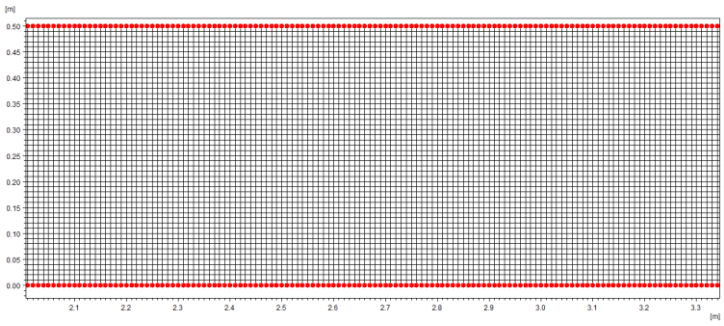


Figure 2. A plan view of computational domain mesh

In this study, the potential of the MIKE 3 Flow Model FM in simulating tsunami waves was evaluated using experimental data provided by the Hydraulic Engineering Department of Changsha University in China by Chen et al. [14]. Figure (3) illustrates a cross-section of the experimental model. The canal has 40 meters long, 0.5 m wide, and 0.8 m high. At the beginning of the canal, a tsunami wave is generated using a piston, while at the channel end, a sedimentary beach with a length of 7.5 m is located. The beach has a variable slope ranging from 1:10 over a length of 3.5 m to 1:20 over a length of 4 meters towards the beginning of the canal. Natural sediment particles with an average diameter of 0.368 mm were used as the beach sediment bed in the experimental model. The generated wave height was 0.15 m, and the initial water depth was 0.35 m. For wave surface elevation, water level changes, and flow velocity measurements, 7 wave gauges (Canadian RBR Limited Liability Company model), 4 ultrasonic water level gauges (Beijing Sinfotek Science and Technology Co., Ltd), and 3D acoustic Doppler velocity sensors (Norway Nortek AS) were utilized. Additionally, a Logitech C910 HD Webcam with a resolution of 1MP was used to capture momentary images of the advancing and receding wave flow alongside the flume. The positioning of the gauges is as shown in Figure (3).

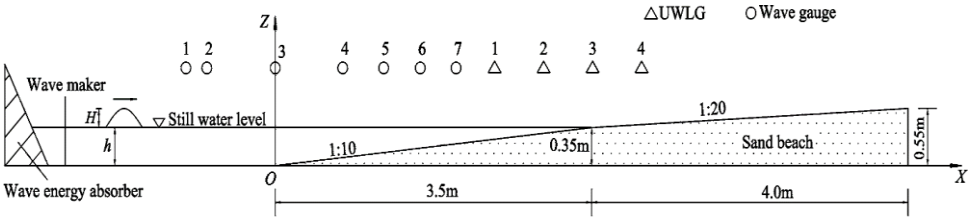


Figure 3. Cross-sectional view of experimental set-up [14].

In order to discern the disparities in values between the outcomes derived from simulation and analytical relationships and experimental data, various evaluation indicators such as Mean Absolute Deviation (MAD), Mean Squared Error (MSE), Root Mean Squared Error (RMSE), and Coefficient of Determination (CD) R^2 were employed. When considering the first three indices, values approaching zero signify an enhancement in the accuracy of the modeling outcomes. Furthermore, a coefficient of determination nearing 1 indicates a favorable correspondence between analytical and modeling results. It is possible to quantify the four performance assessment parameters used in this research using Equations (9) to (12).

$$\mathrm{MAD}=\frac{1}{N}\sum_{i=1}^{N}(p_i-\bar{p}) \tag{9}$$

$$\mathrm{MSE}=\frac{1}{N}\sum_{i=1}^{N}(P_i-O_i)^2 \tag{10}$$

$$\mathrm{RMSE}=\sqrt{\frac{1}{N}\sum_{i=1}^{N}(P_i-O_i)^2} \tag{11}$$

$$\mathrm{CC}=\frac{\sum_{i=1}^{N}(P_i-\bar{P})(O_i-\bar{O})}{\sqrt{\sum_{i=1}^{N}(P_i-\bar{P})^2\sum_{i=1}^{N}(O_i-\bar{O})^2}} \qquad -1\le CC\le 1 \tag{12}$$

where O_i and P_i are, respectively, the observed and the predicted values, $\bar{O}$ is the average of observed values and N is the quantity of observations.

3. Results and Discussion

3.1. Numerical Model Validation

In the initial phase, a comparison was conducted between the outcomes derived from the existing analytical calculations (Eqs. 6-8) and the results obtained from numerical simulations, with the aim of validating and confirming the software. The water depth utilized in these calculations and simulations was standardized at 35 cm, while the ratio of wave height to water depth was simulated at 0.28, 0.42, and 0.57. In order to ensure the numerical software's precision and dependability, several models were assessed to determine adjustable coefficients within the software. This was done to align the simulation results as closely as possible with the analytical values. After several rounds of trial and error, specific values were assigned to the Smagorinsky coefficient (c_S), maximum vertical eddy viscosity, and bed roughness height, as detailed in Table (1). This was carried out to minimize discrepancies between the modeling results and the analytical findings.

The simulation results pertaining to wave velocity and wave surface elevation, as well as their comparison with the output of analytical equations (equations 6 to 8), are depicted in Figure 4. Upon examination of the results presented in this figure, it is evident that while the flow velocity (u) and wave surface elevation (SE) obtained from the software demonstrate a reasonable level of agreement with the results derived from analytical equations, the accuracy of the modeling results diminishes somewhat in comparison to the analytical results as the wave height to water depth ratio (H/h) increases.

Table 1. Calibration of the Numerical Model Coefficients

Parameter	Value	Dimension
Smagorinsky coefficient (c_S)	0.18	-
Maximum vertical eddy viscosity	0.4	**m^2/s**
Manning coefficient (n)	0.01	-

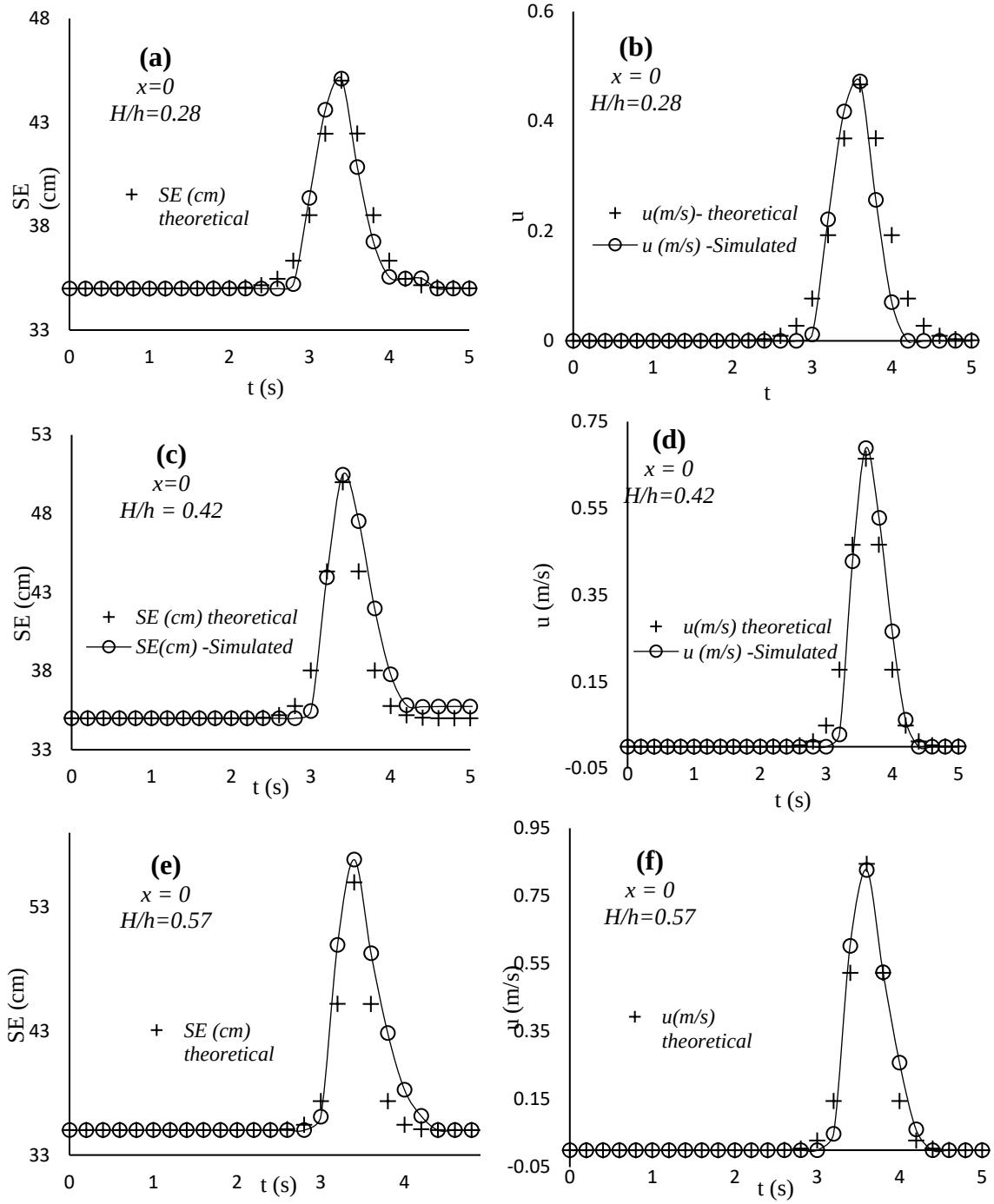


Figure 4. (b, d, f): a comparison of wave velocity (*u)* and (a, c, e): wave surface elevation (*SE*) obtained from numerical simulation and analytical solutions

A comparative analysis of the results derived from analytical relationships and modeling using the aforementioned evaluation indices is delineated in Table (2). Upon scrutiny of the indices for two parameters, wave velocity and wave surface elevation, it is apparent that while the software generally yields satisfactory results in solitary wave modeling, the accuracy of modeling outcomes diminishes with an escalation in the ratio of wave height to water depth (*H/h*). Additionally, based on the findings presented in Table (2), the software demonstrates relatively greater proficiency in computing wave velocity as opposed to modeling wave surface elevation, given that the errors accrued in the wave surface elevation segment are more pronounced for a constant *H/h* ratio. It is imperative to note that the term "n" in Table (2) pertains to the quantity of data points utilized for result comparison.

Table 2. The output indicators of evaluation for comparing the results of simulation and analytical relationship results.

-	**H/h= 0.57 u(m/s)**	**H/h= 0.57 SE (cm)**	**H/h= 0.42 u (m/s)**	**H/h= 0.42 SE (cm)**	**H/h= 0.28 u(m/s)**	**H/h= 0.28 SE (cm)**
n	31	31	31	31	31	**31**
MAD	0.048	1.15	0.033	0.78	0.017	**0.25**
MSE	0.015	10.84	0.006	2.88	0.0013	**0.27**
RMSE	0.124	3.29	0.077	1.69	0.037	**0.52**
R^2	0.79	0.78	0.89	0.90	0.95	**0.97**

3.2. Investigating the potential of numerical model in wave simulation

The study delves into the potential of numerical modeling in simulating wave behavior, with a particular focus on its application in assessing tsunami waves. The accuracy and limitations of the numerical model are rigorously evaluated through statistical analysis and comparison with experimental data. Upon validation of the numerical model using established wave theory equations, the investigation progresses to the examination of its capability in replicating tsunami waves based on experimental results. The findings, analyzed using specified evaluation indicators, reveal a strong concordance between the model's output and the actual data, particularly at specific positions along the simulated channel.

Notably, the highest degree of modeling accuracy is observed at certain positions, such as x = 3.5 m for water surface elevation estimation and x = 0.5 m for flow velocity estimation. These findings are supported by the lowest root mean square error (RMSE) and the highest coefficient of determination (R^2). However, it is crucial to acknowledge that the utilized numerical model, the Mike 3 Flow Model FM, rendering it incapable of accurately simulating severe water surface elevation and flow velocity oscillations. The comparison between the numerical results and experimental data highlights minor discrepancies, particularly evident in the inability of the model to precisely replicate extreme water surface elevation and flow velocity oscillations, as depicted in Figures 5 (d) and (f). The examination extends to the analysis of water surface elevation and flow velocity at various sections along the channel length. The results demonstrate a discernible reduction in water surface elevation as the wave encounters the shoreline slope, followed by a substantial decrease upon crossing the shoreline. Specifically, there is a gradual decrease in wave crest height from 15 cm to 10.5 cm over a 3.5 m initial slope length, and a further reduction from 10.5 to 7.5 cm over a 0.5 m distance after the shoreline (Figs 5 a, b, c).

Conversely, the water flow velocity exhibits an increase as it traverses the shoreline slope, from 0.8 to 1.4 m/s (Fig. 5 e). Furthermore, the presence of negative velocity values indicates instances of wave flow reversal at specific positions along the channel, signifying complex wave dynamics (Figs. 5 e, f, g, h).

Table 3. A comparative analysis of numerical model results and experimental data utilizing statistical characteristics

	u (m/s)				***SE* (cm)**			
-	x=2.5 m	x=2.2 m	x=1.5 m	x=0.5 m	x=4m	x=3.5m	x=2.5m	**x=0**
n	51	51	51	51	51	51	51	**51**
MAD	0.09	0.05	0.08	0.04	0.98	0.29	0.94	**0.25**
MSE	0.02	0.01	0.02	0.00	1.96	0.24	5.26	**0.27**
RMSE	0.13	0.11	0.14	0.07	1.40	0.49	2.29	**0.52**
R^2	0.93	0.91	0.77	0.92	0.97	0.99	0.75	**0.97**

In the context of flow rate per unit width, the value at position x=0 decreases from 0.55 m^3/s-m due to the slope of the shore. At distances x=3.5 m and x=7 m, the value further decreases to 0.14 m3/s-m and 0.02 m3/s-m, respectively. The flow experiences a reversal at distance x=0 starting at 2.5 seconds and continues until the end of the simulation, with a maximum value of 0.04 m^3/s-m (Figure 6). The maximum flow velocity varies with wave position, as illustrated in Figure (7a) it reaches 0.72 m/s in the middle part of the wave crest, 1.3 m/s at the shore slope position (Figure 7b), and 2.1 m/s when crossing the shoreline (Figure 7c). A backflow velocity of 0.96 m/s is observed at the shoreline (Figures 7d and e).

Figure 8 provides a visualization of the vectors and streamlines of water velocity for the central section of the flow at the 7th second of simulation. The vectors depict the path of water flow in different depth layers, indicating the wave flow reversal at the 7th second along the shoreline (at a distance of x=3.5 m). However, it is noteworthy that the maximum flow velocity according to the numerical results is 2.1 m/s, occurring at a distance of 30 cm from the shoreline (Fig. 7c). The observed increase in flow velocity can be attributed to the decrease in water surface elevation at the shoreline.

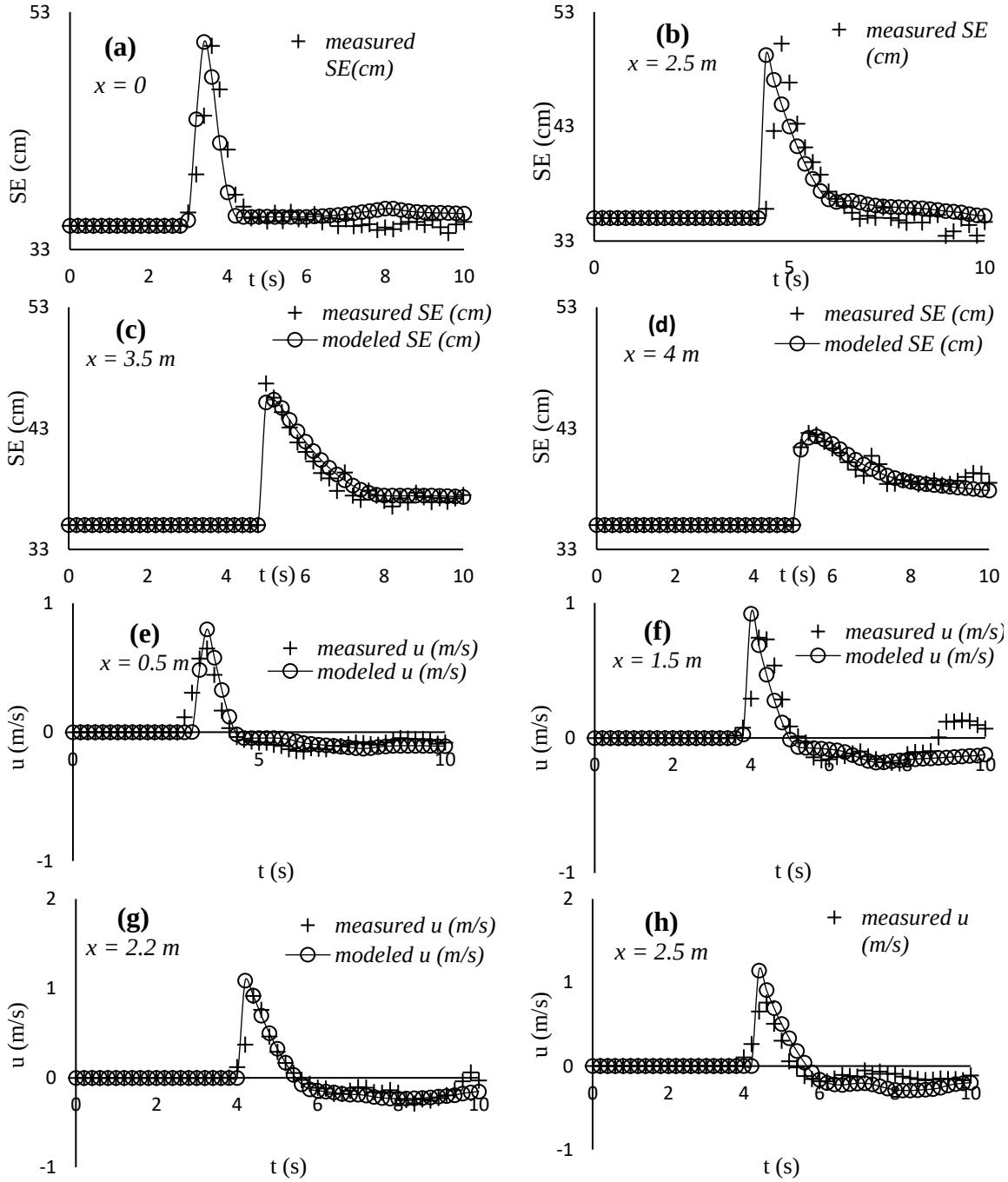


Figure 5. A comparison of wave velocity (u) and wave surface elevation (se) obtained from numerical modeling and experimental results

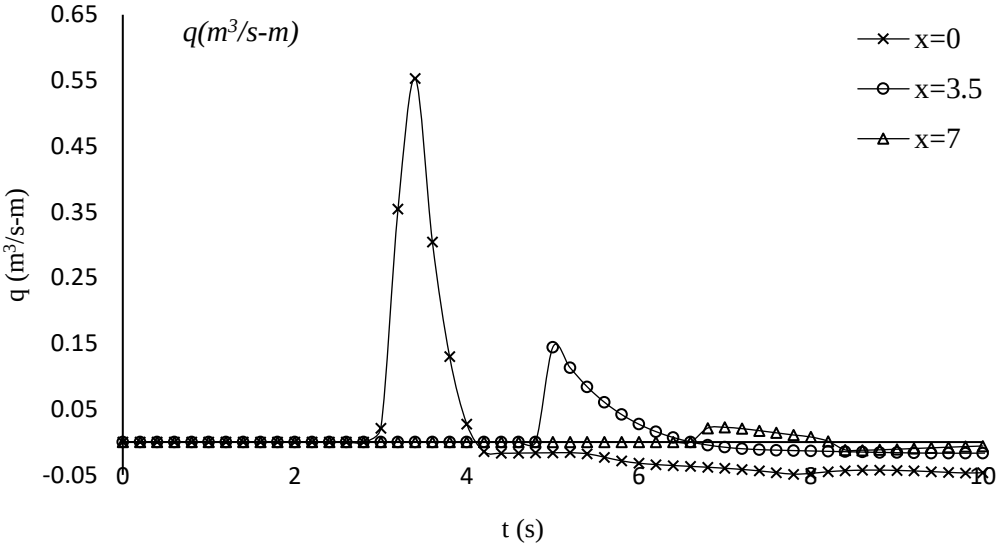
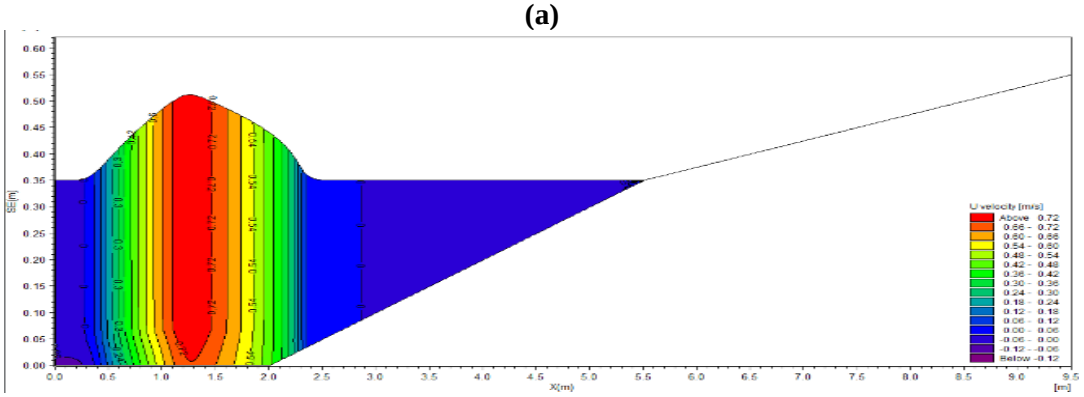
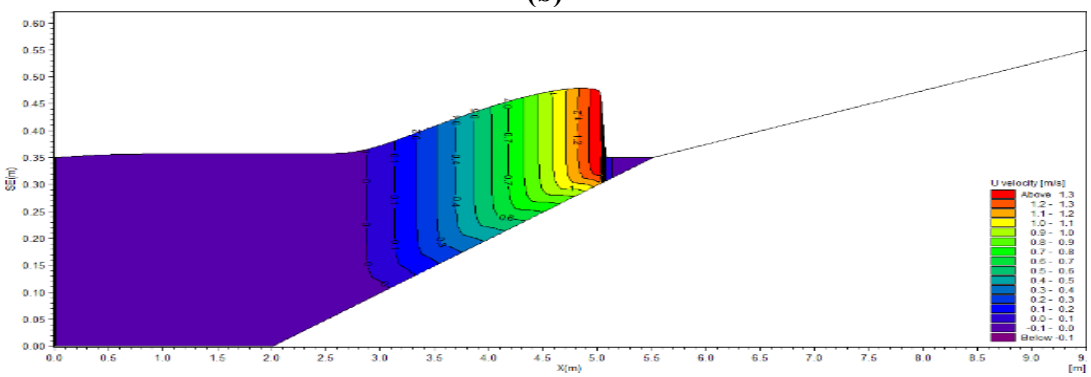


Figure 6. Flow rate per unit width at x=0, x=3.5 m and x=7 m

(a)



(b)



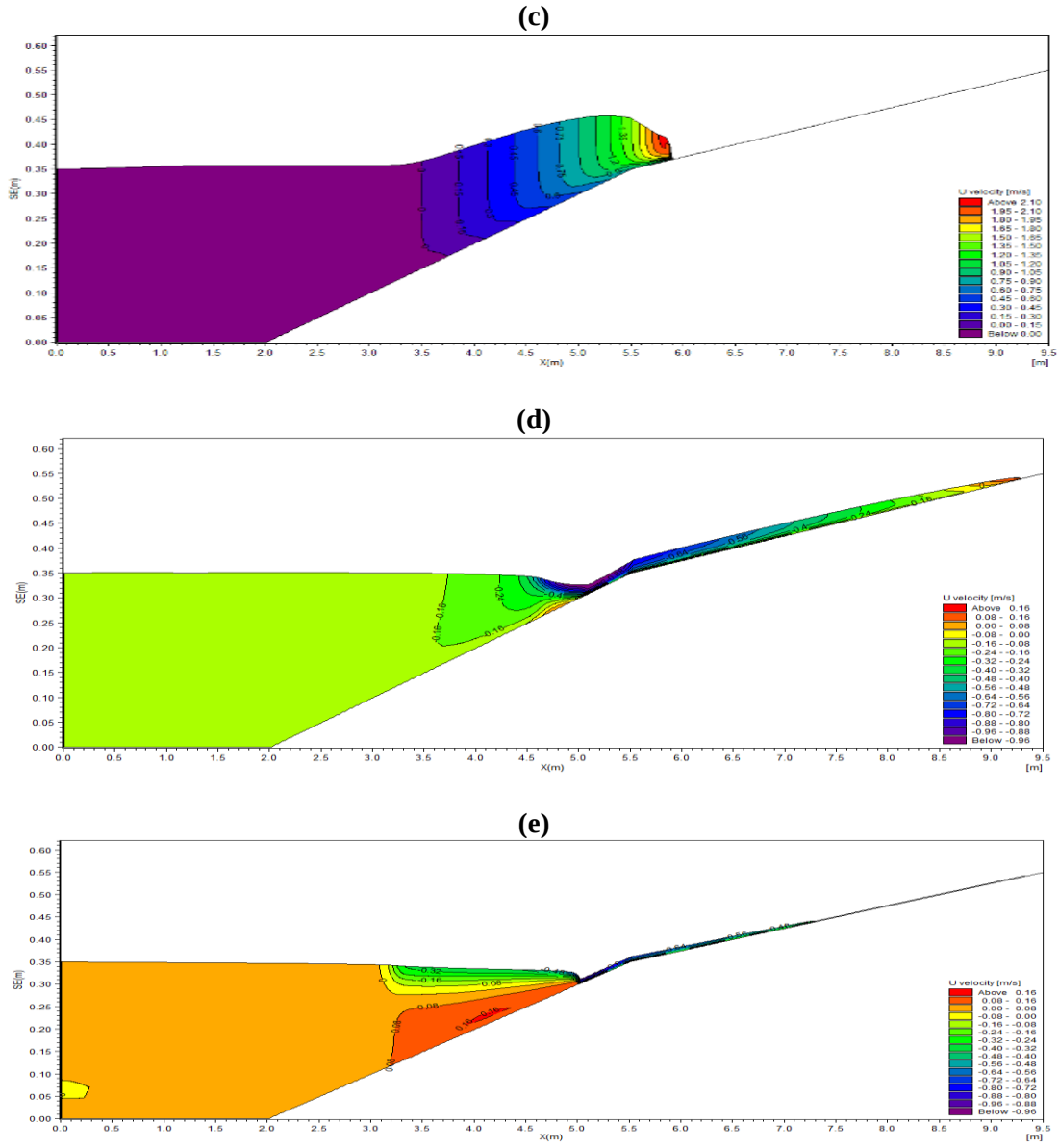


Figure 7. Profile of flow velocity and water surface elevation; a) before the wave reaches the shore slope, b) inside the shoreline, c) Crossing the coastline, d) Rising wave on the beach, e) returned wave (In the longitudinal axis, positive values represent velocity in the forward direction, while negative values represent velocity in the opposite direction).

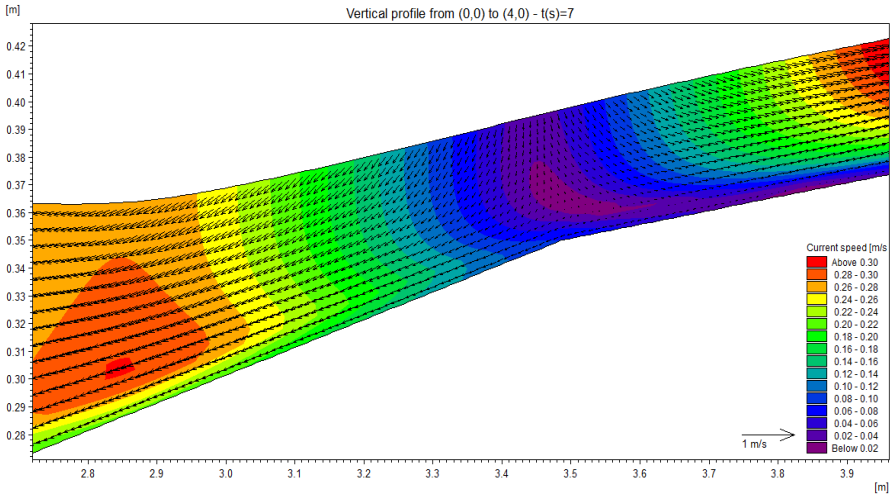


Figure 8. Profile of flow velocity and velocity vectors in 7th seconds of simulation

4 Conclusion

In the current investigation, the study focused on evaluating the ability of the Mike 3 Flow Model FM in accurately simulating free-surface flows, particularly tsunami waves. The numerical model underwent calibration and validation using experimental data conducted by Chen et al. [14] at Changsha University, China, in 2015. Evaluation indices including Mean Absolute Deviation (MAD), Mean Squared Error (MSE), Root Mean Squared Error (RMSE), and Coefficient of Determination (R^2) were utilized to assess the variance between the simulation results and the experimental data.

While minor disparities were noted at certain points between the simulation results and the experimental data, the comparison distinctly demonstrates that the three-dimensional model adeptly captures the dynamics of non-steady flows throughout the entire observation period. Furthermore, the three-dimensional model has the capability to furnish comprehensive and precise insights into the physical parameters of wave evolution in both spatial and temporal dimensions, encompassing water depth, wave height characteristics, flow velocity, wave front propagation distance, and other pertinent factors.

Upon comparing the numerical results with experimental data, it became evident that the accuracy of the numerical model in simulating wave velocity (RMSE $\leq$ 0.14) surpassed its performance in simulating wave surface elevation (RMSE $\leq$ 2.29). This disparity underscores the nuanced nature of wave dynamics and highlights the need for continued refinement in numerical modeling approaches. Overall, these findings underscore the potential of the numerical model in capturing wave dynamics, particularly in scenarios where the ratio of wave height to water depth is low. However, further research and validation against diverse experimental datasets are warranted to fully ascertain the robustness and generalizability of the numerical package. In light of the current investigation, it is imperative to recognize that our focus has been primarily on analyzing the flow pattern. However, it is essential to emphasize the necessity for additional research to assess the efficacy of the aforementioned numerical model in simulating erosion and sedimentation patterns. This further exploration will provide a more comprehensive understanding of the model's capabilities and limitations in replicating real-world scenarios. Consequently, such research will contribute to the advancement of knowledge in this field and facilitate the development of more accurate and reliable numerical models for practical applications.

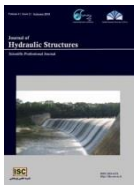
5 References

1. Camfield, F.E., 1980. Tsunami Engineering. Special Report No. 6. US Army Corps of Engineers, CERC, Ft. Belvoir, VA.
2. Xie, J., (2007). Numerical modeling of tsunami waves (Doctoral dissertation, University of Ottawa (Canada)).
3. Bandyopadhyay, A., Manna, S. and Maji, D., (2021). Hydrodynamic aspects of tsunami wave motion: a review. Ocean Dynamics, 71(5), pp.613-629.
4. Harbitz, C.B., Løvholt, F., Pedersen, G. and Masson, D.G., (2006). Mechanisms of tsunami generation by submarine landslides: a short review. Norwegian Journal of Geology/Norsk Geologisk Forening, 86(3).
5. Yavari-Ramshe, S. and Ataie-Ashtiani, B., (2016). Numerical modeling of subaerial and submarine landslide-generated tsunami waves—recent advances and future challenges. Landslides, 13, pp.1325-1368.
6. Madsen PA, Fuhrman DR, Schaeffer HA (2008) On the solitary wave paradigm for tsunamis. J Geophys Res. doi:10.1029/2008jc004932.
7. Costa, P.J. and Andrade, C., (2020). Tsunami deposits: present knowledge and future challenges. Sedimentology, 67(3), pp.1189-1206.
8. Hammack, J.L. and Segur, H., (1974). The Korteweg-de Vries equation and water waves. Part 2. Comparison with experiments. Journal of Fluid mechanics, 65(2), pp.289-314.
9. Oetjen, J., Sundar, V., Venkatachalam, S., Reicherter, K., Engel, M., Schüttrumpf, H. and Sannasiraj, S.A., (2022). A comprehensive review on structural tsunami countermeasures. Natural Hazards, 113(3), pp.1419-1449.
10. Synolakis, C.E., (1987). The runup of solitary waves. Journal of Fluid Mechanics, 185, pp.523-545.
11. Zelt, J. (1991). "The run-up of nonbreaking and breaking solitary waves." Coastal Engineering **15**(3): 205-246.
12. Honarmand M, Shanehsazzadeh A, Zandi M, Vahida A. Numerical Simulation and Experimental Study on Tsunami Propagation and Run-up and the Influence of Submerged Breakwater on Run-up. Journal of Oceanography 2019; 9 (36) :31-38. URL: http://joc.inio.ac.ir/article-1-1248-fa.html.
13. Honarmand M , Zandi M, Shanehsazzadeh A., (2016). 2D Numerical simulation of solitary waves propagation nearly beach in order to determination of tsunami waves run-up. Civil engineering conference 2016. Ferdowsi university of Mashhad, Mashhad, Iran.
14. Chen, J., Huang, Z., Jiang, C., Deng, B. and Long, Y., (2012). An experimental study of changes of beach profile and mean grain size caused by tsunami-like waves. Journal of Coastal Research, 28(5), pp.1303-1312.
15. Chen, Y.Y., Kharif, C., Yang, J.H., Hsu, H.C., Touboul, J. and Chambarel, J., (2015). An experimental study of steep solitary wave reflection at a vertical wall. European Journal of Mechanics-B/Fluids, 49, pp.20-28.
16. Zaqian, R., et al. (2017). Experimental study of flow structures of a solitary wave propagating over a submerged thin plate in different angles using PIV technique. International Journal of Heat and Fluid Flow 66: 18-26.
17. Wang, J., et al. (2018). Numerical study on interaction of a solitary wave with the submerged obstacle. Ocean engineering 158: 1-14.
18. Cavaliere, D., la Forgia, G., Adduce, C., Alpers, W., Martorelli, E. and Falcini, F. (2021). Breaking location of internal solitary waves over a sloping seabed. Journal of Geophysical Research: Oceans 126(2): e2020JC016669.

19. He, J.H., Qie, N. and He, C.H., (2021). Solitary waves travelling along an unsmooth boundary. Results in Physics, 24, p.104104.
20. Zou, P.X., Bricker, J.D. and Uijttewaal, W.S., (2021). The impacts of internal solitary waves on a submerged floating tunnel. Ocean Engineering, 238, p.109762.
21. Huang, C. J., & Dong, C. M. (2001). On the interaction of a solitary wave and a submerged dike. Coastal Engineering, 43(3-4), 265-286.
22. Huang, Z., Yao, Y., Sim, S. Y., & Yao, Y. (2011). Interaction of solitary waves with emergent, rigid vegetation. Ocean Engineering, 38(10), 1080-1088.
23. Soudi, Mina, Hojjat Ahmadi, Mehdi Yasi, Stefano Sibilla, Andrea Fenocchi, and Sajad Ahmad Hamidi (2019). Investigation over the capability of MIKE 3 flow model FM to simulate the hydrodynamics and salinity distribution of hypersaline lakes: Lake Urmia (Iran) as case study." Coastal Engineering Journal 61, no. 4. 486-501.
24. Hemmati, Mohammad, Hojjat Ahmadi, Sajad Ahmad Hamidi, and Vahid Naderkhanloo. (2021). "Environmental effects of the causeway on water and salinity balance in Lake Urmia." Regional Studies in Marine Science 44. 101756.
25. Bigdeli-Tabar-Sahreini, H., Hemmati, M., Ahmadi, H., Naderkhanloo, V. (2018). 'Numerical Investigation of the Effect of Groins and Bendway Weirs on Flow and Sediment Pattern Using Mike 3 Flow Model FM', Water and Soil Science, 28(1), pp. 159-171.
26. Naderkhanloo, V., Soudi, M., Hemmati, M. and Hamidi, S.A., 2017. 3D Numerical simulation of dam-break flows with sediment transport over movable beds. In World Environmental and Water Resources Congress 2017 (pp. 161-170).
27. MIKE 3 User Guide and Reference Manual, Danish Hydraulic Institute (DHI) (2007). Water and Environment, Denmark.
28. Goring, D.G., (1979). Tsunamis-The propagation of long waves on to a shelf. California Institute of Technology, Pasadena.
29. Li, Y., and F. Raichlen (2003), Energy balance model for breaking solitary wave run-up, J. Waterway, Port, Coast Ocean Eng., 47, 47–59.

© 2024 by the authors. Licensee SCU, Ahvaz, Iran. This article is an open access article distributed under the terms and conditions of the Creative Commons Attribution 4.0 International (CC BY 4.0 license) (http://creativecommons.org/licenses/by/4.0/).

Journal of Hydraulic Structures
J. Hydraul. Struct., 2025; 11(2): 44-60
DOI: 10.22055/jhs.2024.46910.1299



OPEN ACCESS

An investigation on the parameters affecting the behavior of broadly graded, dispersive base soil-filter systems in earth dams

Amir Hossein Vakili[1]
Amin Falamaki[2]

Abstract

Designing appropriate filter materials is as important as ensuring the safety factor of the entire body of earth dams. The performance of the downstream filter zone in earth dams could be significantly influenced by base soil features, particularly in the case of cohesive broadly graded cores. The effects of several variables, such as base soil plasticity, fine content, and clay content, on the properties of effective filter materials were investigated experimentally in the current study. Results obtained through the no erosion filter (NEF) test indicated that the plasticity of base soil materials had no apparent correlation with the corresponding filter materials. However, fine content was found to have significant effects on the boundaries of the no erosion filter, especially for soils classified as Group 1. Although there was a decreasing tendency in D_{15f} size with increasing clay content of the base materials, the effects of clay content on the required filter materials were not as significant as those of fine content. In conclusion, designing filter materials by concurrently considering d_{85} and fine content (F) of base materials appears to be more logical than separately utilizing these effective parameters. In this scenario, the new filter design criterion was derived using regression techniques based on experimental results.

Keywords: cohesive soils; effective filter; soil plasticity; fine content; clay content

Received: 14 May 2024; Accepted: 30 September 2024

List of notations

$PP \leq$	Percentage finer than 0.002 mm;
$PP \leq$	Percentage finer than 0.005 mm;
F	Fine content (%)
PI	Plasticity index (%)
PSD	Particle size distribution;
D_{15f}	Size of filter material of which 15% of the material passes;

*Email: a_falamaki@pnu.ac.ir **(Corresponding Author)**
[1] Department of Civil Engineering, Faculty of Engineering, Zand Institute of Higher Education, Shiraz, Iran.
[2] Department of Civil Engineering, Payame Noor University, P.O. Box 19395-3697, Tehran, Iran.

CC BY

D_{15bdy}	D_{15f} size of filter material found from no erosion filter test to be the boundary between successful and unsuccessful test;
d_n	Size of base soil materials of which n percentage of the material passes;
n	The percentage passing diameter d_n;
NEF	No - erosion filter;
CL	Low plasticity clay;
CH	High plasticity clay;
ML	Low plasticity silt;
D	Percent dispersion or degree of dispersion;
MDD	Maximum dry density (gr/cm^3);
OMC	Optimum moisture content (%);
K_f	Coefficient of permeability of filter material (cm/sec);
USCS	Unified soil classification system;
Base soi Group 1	A base soil with a fine content of 85% or more;
Base soil Group 2	A base soil with a fine content of less than 85%;
Fine content	Percentage finer than 0.075 mm;
Clay content	Percentage finer than 0.002 mm.

1. Introduction

The phenomenon of soil erosion and sediment transport are among the key hydrodynamic processes recognized as one of the major challenges and an important potential failure mode in the exploitation of surface water resources worldwide [1,2]. Therefore, research has been carried out regarding the design of filters [3]. Generally speaking, the performance of an earth dam is equally dependent on the performance of the core as well as the protective filter. Designing the filter can thus be considered as important as designing the core, and in fact, the two are inseparable as reflected by the way established design criteria have been presented [4,5]. Filter materials must be sufficiently fine to prevent the migration of erodible particles of the base soil, and at the same time, they must be adequately coarse to allow drainage of seepage water without the accumulation of excessive pore water pressure [6]. Hence, filter materials are designed based on two general criteria: retention criterion and permeability criterion. Filter retention criteria are usually expressed in three forms - the geometric grading criterion, the constriction-based criterion, and the hydraulic criterion [7]. The design of filter based on geometric grading criterion basically involves particle size distributions (PSDs) of the base soil and the filter, and is presented in the form of filter-base soil grain size ratios [8-12]. D15f and d85 sizes are often specified as representative sizes for the filter and base soil, respectively, in geometric grading criteria. The phenomenon of internal soil erosion is significantly influenced by relative density, relative particle size distribution of base soils and filters and applied hydraulic gradient [13,14]

On the other hand, the required permeability of filter materials should be specified within the hydraulic criteria. Thus, designing filters based on hydraulic criteria involves considering both the PSD of the base soil and the permeability of the filter. In this approach, the filter's permeability (k_f) and the d_{85} size of the base soil are commonly used as representative parameters. Unlike grading criteria, hydraulic criteria emphasize the relationship between filter permeability and the PSD of the base materials [5].

To address the challenges associated with traditional filter design criteria, the state-of-the-art design criteria known as constriction-based criteria were introduced. This method simultaneously

considers the effects of various parameters such as PSD, compaction, grading, surface area, porosity, and uniformity coefficient of filter materials during the design process. The approach involves applying a programming subroutine to convert the filter's PSD curve into constriction size distribution (CSD) curve. After determining the CSD curve of filter materials, two key parameters, namely the controlling constriction size (D_{c35}) and self-filtering constriction size (D_{c95}), are measured. The procedure continues by modifying the PSD curve of the base materials, removing particles larger than D_{c95} size, and measuring the new representative size (d^*_{85}) form the modified PSD curve of the base soil materials. Finally, this criterion emphasizes the relationship between the controlling constriction size of the filter and the modified PSD of the base materials [5].

In the traditional filter design criteria, the actual or modified d_{85} size of base materials is usually used as a representative of the base soil in filter design practices. However, significant questions arise regarding whether the effectiveness of the filter could be influenced by other base soil features such as plasticity, clay content, fine content, etc. It is well known that the process of internal erosion for cohesive base materials is more complex than for non-cohesive ones [15]. This complexity arises because the internal erosion process can be significantly influenced not only by the particle size distribution of core and filter materials but also by the erodibility of base soils [16]. Vakili et al. [17] investigated several base soils, including cohesive, broadly graded and dispersive soils, and found that the erodibility and dispersivity of the base soil significantly impact the formation of internal erosion and, consequently, the required filter materials. They reported the strong and adverse relationship between dispersivity degree of core materials and their corresponding no-erosion filter boundaries [17]. Furthermore, the effects of water quality on the NEF test results, when the base soil materials were broadly graded, cohesive, and dispersive, were examined by Vakili et al. [7] using two different waters including distilled and Malaysian river waters. It has been found that the chemistry of water reservoirs can change the erosion rate of dispersive base materials and, therefore, the required D_{15f} size of filter materials [7].

For the case of broadly graded, cohesive, dispersive base materials, the geometric grading criteria of $D_{15f}/d_{85} = 0.6037(d_{85})^{-0.66}$ and $D_{15f}/d_{85} = 10.0\exp(-0.009D)$ were introduced by Vakili et al. [17]. They believe that the former criterion could predict the no-erosion filter boundary better than traditional filter design criteria if only the d_{85} size of base materials is taken into account. However, the latter criterion was considered relatively new because, in addition to particle size distribution, the dispersivity degree of core materials is also considered concurrently in the filter design process.

By and large, there are still uncertainties in designing suitable materials for the case of broadly graded, cohesive, dispersive base materials. To highlight the current problem statement, consider two different base soils, each having the same d_{85} and dispersion degree but differing properties such as different clay and contents. In such cases, materials with similar gradation curves, specifically similar D_{15f} values, might be considered appropriate filters according to universally accepted existing filter design criteria, such as the Sherard and Dunnigan [18] criteria. In other words, the D_{15f}/d_{85} ratios would be identical for both cases, irrespective of other base soil features. Therefore, due to the differing characteristics of base soils, there is a general question: do these base soil-filter combinations exhibit similar behavior in terms of mass retention capability and flow rates? Alternatively, could identical filter materials be effective in both cases? Or do factors like plasticity, fine content, and clay content render the filter system ineffective? Hence, further investigations are necessary to examine the influential parameters of cohesive base soil on the characteristics of required filter materials. In the majority of filter design criteria, only the effects

of d_{85} size of base materials are considered. Therefore, the main objective of this study was to assess the effects of base soil features on filter effectiveness, if any.

2. Materials and Methods

The results from the experimental tests program were analyzed to determine:

1- The effect of base soil plasticity on filter effectiveness;
2- The effect of base soil fine content on filter effectiveness;
3- The effect of base soil clay content on filter effectiveness.

To achieve the aforementioned aims, twenty-two base soils with varying characteristics were collected from Batu Gajah, Malaysia. To assess the characteristics of the base materials, all collected samples were tested for particle size distribution in accordance with ASTM D 422 [19], plasticity index following ASTM D 4318 [20], double hydrometer as per ASTM D 4221-99 [21], and standard compaction tests according to ASTM D 698 [22]. Based on the aforementioned tests, the main features of the samples were determined, including fine content, clay content, plasticity index, soil dispersivity, soil class according to the Unified Soil Classification System (USCS), optimum moisture content (OMC), and maximum dry density (MDD), as presented in Table 1.

To assess the performance of various filter-base soil combinations, the NEF tests were carried out. The NEF test, originally developed by Sherard and Dunnigan [18], was followed in this study according to the procedures described by Sherard and Dunnigan [18] and Soroush and Shourijeh [23]. Figure 1 shows a photo of the actual experimental setup of the NEF test equipment.

The NEF test cylinder was transparent, with a diameter of 11 cm and a height of 30 cm. In the test procedures, a drainage layer made of gravel-sized material was placed at the bottom of cylinder, separated from the filter layer by a wire screen. The filter material was 10 cm thick and consisted of 4 compacted sub-layers. The fabricated filter materials were initially saturated and thoroughly mixed. The filter materials placed into the NEF cylinder were compacted using both vibration and tamping techniques. A relative density of 75% was used for the compaction of the filter materials in the NEF test.



Figure 1. A view of the NEF equipment arrangement under test

Instead of using granular-sided materials, a plastic ring was used to intrude into the final filter layer; this plastic ring, which intruded into the final filter layer, also known as water-tight plastic. The overlying base soil was 2.5 cm thick and consisted of 2 sub-layers, each compacted to maximum dry density. Note that the base soil samples were first mixed with distilled water before being compacted in the NEF test cylinder. The amount of water added was equal to the required value to achieve the optimum moisture content determined by the standard Proctor test. The prepared samples were placed in an airtight plastic bag and stored for 24 hours to allow equilibrium between the dissolved salts in the soil pore water. A 1 mm diameter perforation was made through the base soil layer and extended 1 cm into the filter layer. Another wire screen separated the base soil layer from the upper drainage layer, which, like the lower drainage layer, also made up of gravel size material. At the beginning of the test, the inlet valve and air vent were slightly opened while the outlet valve remained closed. After saturating the gravel drain with water and de-aerating it, the air vent was closed and the outlet valve opened. The water pressure of 400 kPa or 4.0 kg/cm^2 was applied during the procedure. In other words, the applied hydraulic gradient was approximately 1600 due to water flow through the perforation.

The performance of filter-base soil system was assessed by collecting the effluent, measuring the flow rate every minute, inspecting the effluent turbidity, and determining the perforation size after each test. A filter material was considered successful in protecting the base soil if no visible erosion occurred- i.e., no enlargement in the initial size of perforation. The duration of each test was typically about 20 minutes. Longer tests were not necessary, as erosion of the base material usually occurs within the first 20 minutes of the test (Delgado Ramos and Locke, 2000).

For filters, 14 different types of clean sandy samples with various PSDs or D_{15f} sizes were artificially prepared. The filter materials placed into the NEF cylinder were compacted using both vibration and tamping techniques. Granular soils, such as filter materials, are typically compacted to achieve a desired relative density. Relative density serves as a compaction index for granular soils [24]. Relative densities of 75% were utilized for compacting the filter materials in the NEF test. It's noteworthy that relative densities of 70% have been observed to suffice in field conditions to mitigate the risk of flow liquefaction during earthquakes [25]. Conversely, Fell et al. [25] argue that there are no discernible benefits in using relative densities exceeding 80% for the filter zone of earth dams. Moreover, employing relative densities greater than 80% can lead to excessive breakdown of filter materials [25]. Therefore, it appears reasonable to apply a relative density of 75% in the test procedure.

Table 1: Characteristics of base materials collected for the current study

Base soil Group	d_{85} (mm)	Fine content (%)	Clay content (%)	D (%)	PI (%)	Soil class based on USCS
1-S_1	0.03	91.0	40	93.0	16	CL
1-S_2	0.065	88.0	35	51.0	17	CL
1-S_3	0.038	92.0	40	61.0	24	CL
1-S_4	0.02	96.0	48	82.0	35	CH
1-S_5	0.015	100.0	41	45.0	31	CH
1-S_6	0.062	86.0	37	32.0	13	CL
1-S_7	0.055	90.0	20	69.0	8	ML
1-S_8	0.050	92.0	35	41.0	12	CL
1-S_9	0.044	88.0	40	82.0	17	CL
1-S_{10}	0.060	88.0	36	75.0	24	CL
1-S_{22}	0.065	87	44	96.0	34	CH
2-S_{11}	0.20	83.0	35	65.0	16	CL
2-S_{12}	0. 10	82.0	33	74.0	20	CL
2-S_{13}	0. 30	76.0	3.5	32.0	15	CL
2-S_{14}	0.15	78.0	7.0	15.0	25	CL
2-S_{15}	0.15	75.0	33	50.0	16	CL
2-S_{16}	0.090	83.0	34	43.0	31	CH
2-S_{17}	0.091	83.0	32	81.0	17	CL
2-S_{18}	0.13	71.0	14	89.0	11	ML
2-S_{19}	0.18	80.0	31	56.0	18	CL
2-S_{20}	0.09	82.0	30	37.0	17	CL
2-S_{21}	0.23	75.0	25	9.0	13	CL

For the preparation of base materials, the base soil samples were thoroughly mixed with water. The quantity of water added was adjusted to achieve their optimum moisture content, as determined by the standard Proctor test (by referring to Table 1). The prepared samples were placed into airtight plastic bags and maintained for 24 hours to achieve equilibrium between dissolved salts in the soil pore water. The base soil was then compacted inside the cylinder using a tamper. The compaction process continued until reaching a final thickness of 25 mm. Note that all base materials were compacted at their maximum dry density (MDD) and optimum moisture content (OMC).

The pressure of water applied in the NEF test procedure was 400 kPa or 4.0 kg/cm^2. In other words, the applied hydraulic gradient was about 1600 due to water flow through the performed hole. Considering the geometry and reservoir heights of large dams, pressures of over 350 kPa must be applied in filter test procedures for a highly accurate simulation of large dams [12]. Note that the duration of each test is normally about 20 minutes and tests for a longer period are not compulsory because erosion of the base materials usually takes place within the first 20 minutes after starting the test [27].

Based on the NEF test results, the boundary between successful and unsuccessful filter materials could be determined for any given core materials with specific properties [18,25]. In this study, the D_{15bdy} values were determined for all base soil specimens.

3. Results and Discussions

3.1. Effects of plasticity of base materials on filter effectiveness

The influence of base soil plasticity on the no-erosion filter boundary is illustrated in Figure 2. The plasticity of the collected base materials was found to have little effect on the no-erosion filter boundary, as already reported by Sherard and Dunnigan [18], Foster and Fell [25], and Zomorodian and Moghadam [28]. However, Delgado et al. [16] found a strong correlation between the plasticity of base materials and the D_{15f} size of required filter materials. Delgado et al. [16] believed that base soil plasticity increases directly with its fine content, thus leading to a decrease in the D_{15f} size of required filter materials. Although there is a general trend of increasing D_{15bdy}/d_{85} ratio with increasing plasticity index, the correlation obtained is not as strong as those obtained by Soroush et al. [29] and Delgado et al. [16].

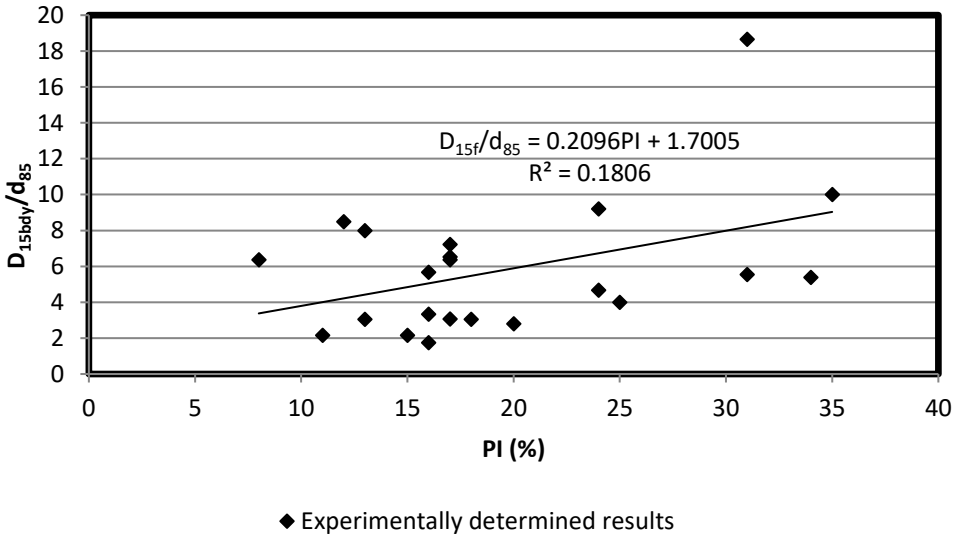


Figure 2. Variation of the plasticity index of the base soils against ratio of D_{15bdy}/ d_{85} for broadly graded, dispersive core materials

Nevertheless, the given endorsement comes with the following remarks:

1- The plasticity of almost all base soils tested by Soroush et al. [29] was less than 10. However, the plasticity index of base materials collected for the current study ranged from 8% to 35%. Thus, the results obtained in the current study may not be compatible with those of Soroush et al. [29], as the current study covers a wider range of base materials.

2- The compatibility of the NEF test results against the criterion suggested by Delgado et al. [16] is illustrated in Figure 3. The experimentally determined results were found to be incompatible with the criterion suggested by Delgado et al. [16], as the majority of the plots are placed below the line. The criterion becomes questionable, especially for those base materials with a plasticity index less than 20%. In other words, the criterion suggests a D_{15f} size of more than 0.9 mm for base materials with a PI less than 10. However, all base materials tested by Soroush et al.

[29] required filter materials with a D_{15f} size less than 0.4 mm, illustrating the inaccuracy of the criterion. Further evidence from the current study supports this. For instance, sample 1-S7 had an ML classification with a PI of 8%. The criterion suggests a D_{15f} of 1.15 mm as a no-erosion filter boundary. However, the experimentally determined no-erosion filter boundary was 0.35 mm, which is 3.3 times smaller than the criterion. Thus, the base soil features could not be effectively represented by plasticity in filter design purposes.

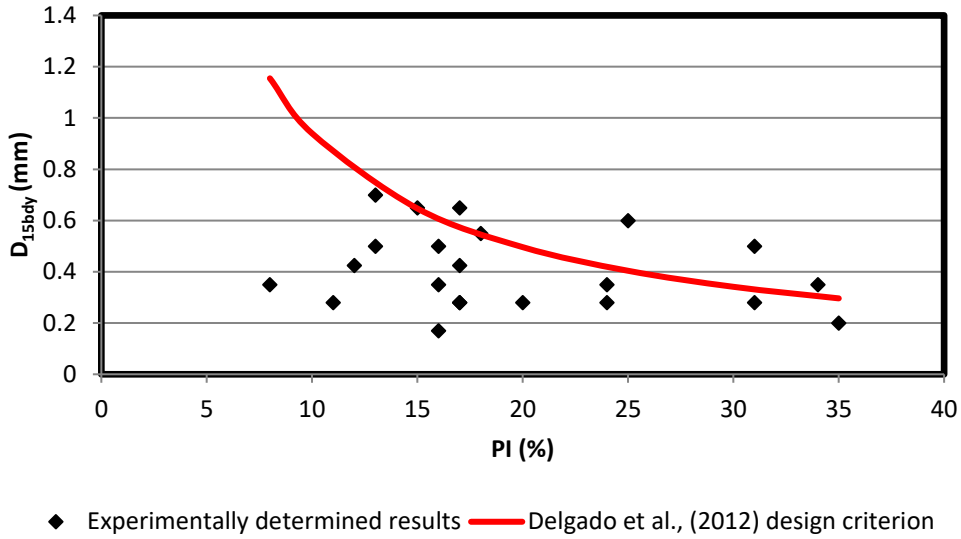


Figure 3. Comparison of the NEF test results with design criterion suggested by Delgado et al., (2012)

3.2. Effects of clay content of base materials on filter effectiveness

The effect of clay content of base soil materials on the no-erosion filter boundary is given in Figures 4 and 5. Generally, the D_{15bdy} size of filter materials tends to decrease, and the D_{15bdy}/d_{85} ratio tends to increase as the clay content of base materials increases. This general tendency could be attributed to the susceptibility of the clay particles to dispersion and de-flocculation. In other words, the extent of eroded particles increases as the degree of segregation of the clay particles increases, thus diminishing the filter effectiveness.

Two definitions exist for clay particles in the literature. Clayey soils are usually defined as soils with particles less than 0.002 mm. However, particles in the range of 0.002 to 0.005 mm are sometimes considered as clay [24]. The better trend could be observed between clay content and required filter materials when particles less than 0.005 mm are considered as clayey soils, as shown in Figures 6 and 7.

The best fit expression obtained by Foster and Fell [25] is compared with the best fit expression derived from the current study for base soils Group 1, as observed in Figure 8. The best fit expression proposed by Foster and Fell [25] could not successfully predict the appropriate filter

materials in terms of D_{15f} size, as 10 out of 11 plots are placed below the line, reflecting a no-erosion probability of only 9%.

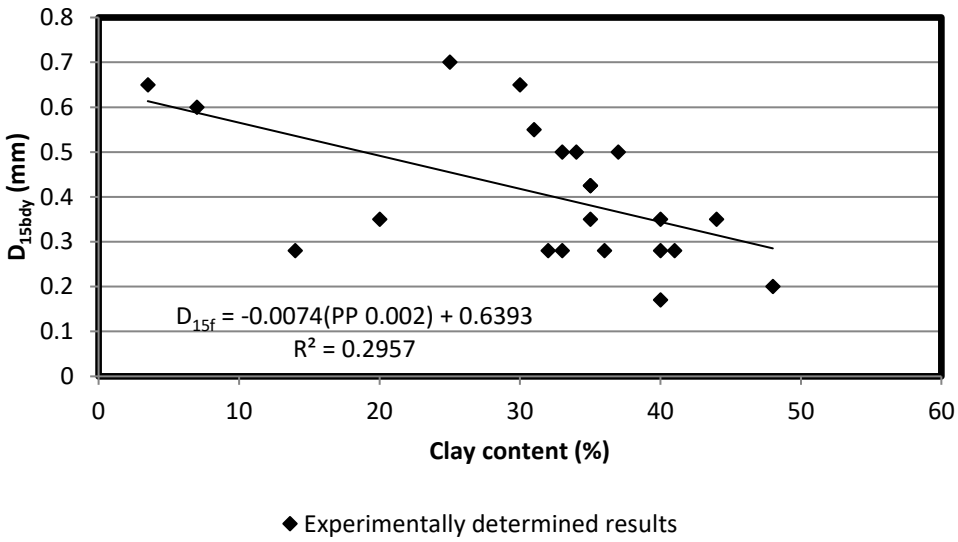


Figure 4. Variation of the clay content (PP ≤ 0.002) of the base soils against experimentally determined filter boundary (D_{15bdy}) for broadly graded, dispersive core materials

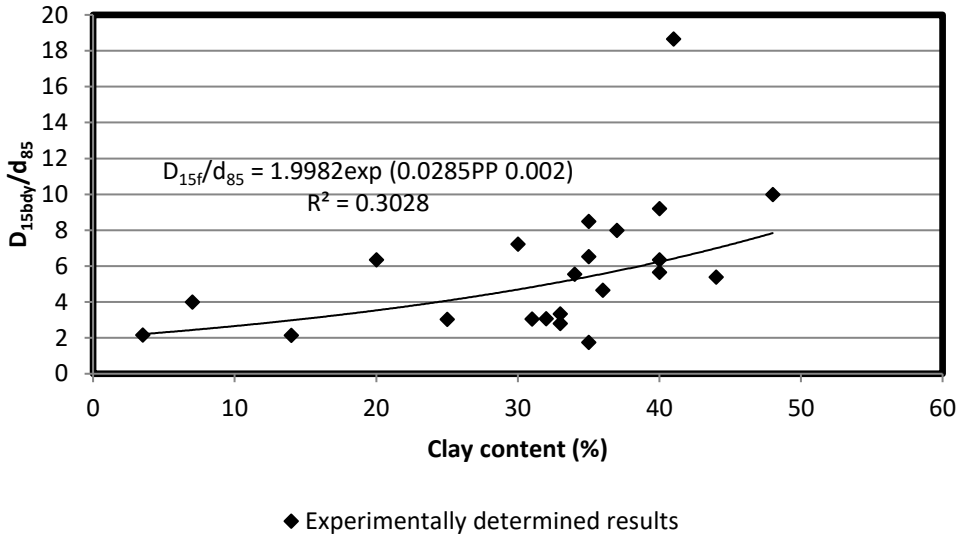


Figure 5. Variation of the clay content (PP ≤ 0.002) of the base soils against ratio of D_{15bdy}/ d_{85} for broadly graded, dispersive core materials

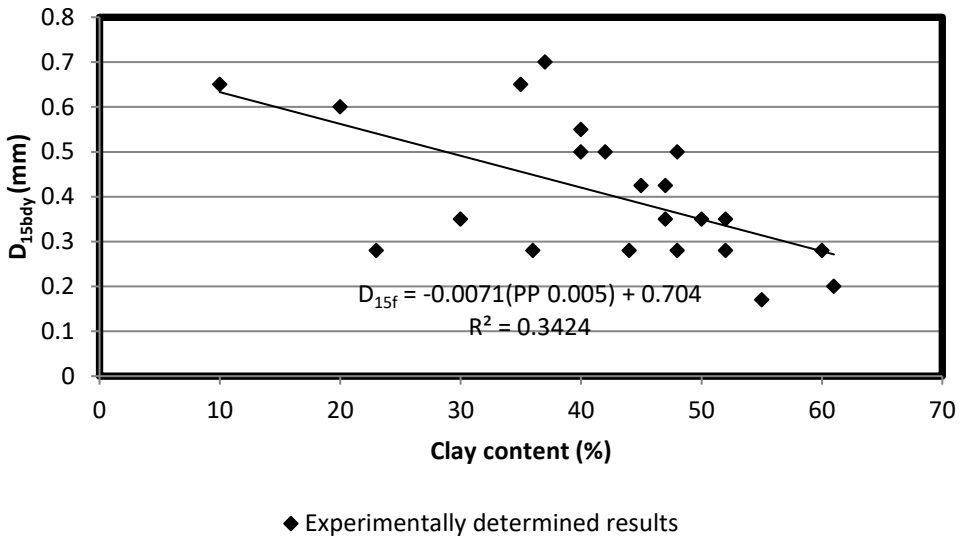


Figure 6. Variation of the clay content (PP ≤ 0.005) of the base soils against experimentally determined filter boundary (D_{15bdy}) for broadly graded, dispersive core materials

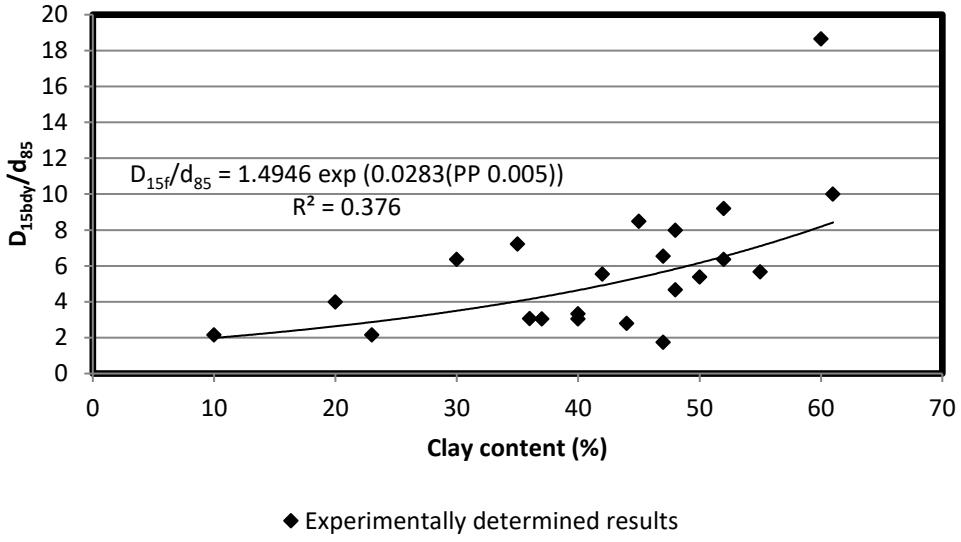


Figure 7. Variation of the clay content (PP ≤ 0.005) of the base soils against ratio of D_{15bdy}/ d_{85} for broadly graded, dispersive core materials

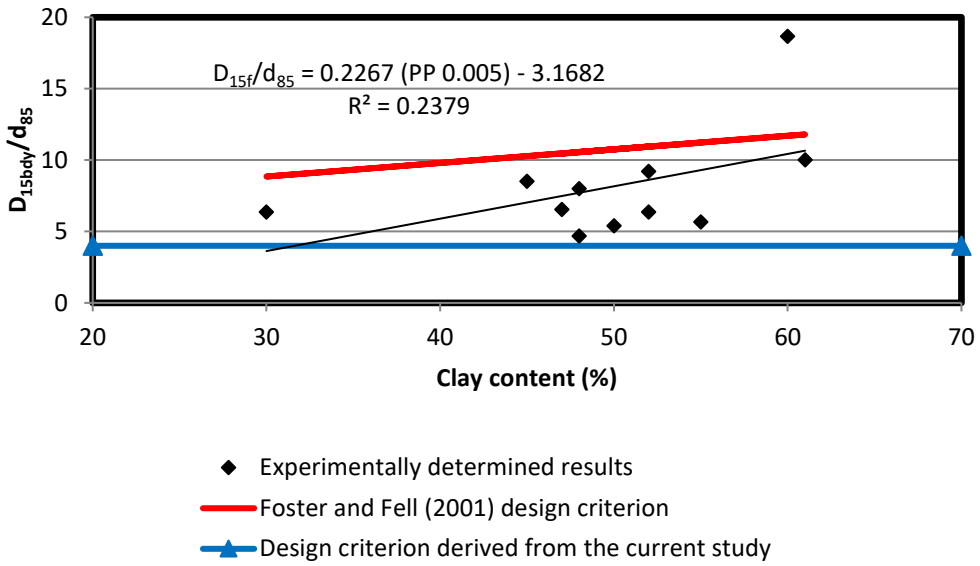


Figure 8. Comparison of the NEF test results with Foster and Fell [25] design criterion for base soil of Group 1

Consequently, as experimentally determined by the current study, selecting the criterion of D_{15f}/d_{85} = 4.0 as the no-erosion lower bound could be logical for various broadly graded, cohesive, dispersive base materials of Group 1 with different clay content.

3.3. Effects of fine content of base materials on filter effectiveness

The influence of fine content of base soil materials collected on the required filters is diagrammatically illustrated in Figure 9.

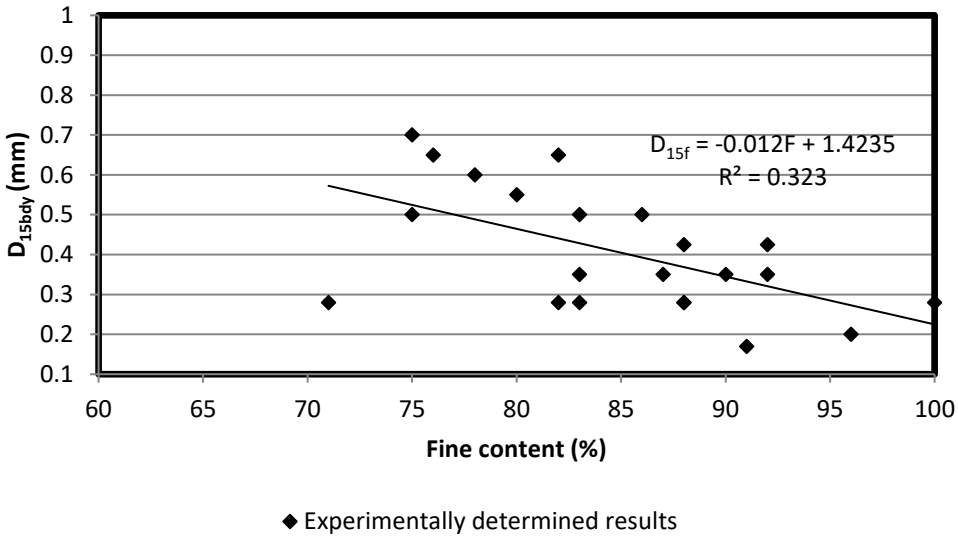


Figure 9. Variation of the fine content of the base soils against experimentally determined filter boundary (D_{15bdy}) for broadly graded, dispersive core materials

Although there is a general tendency for decreasing D_{15bdy} size of filter materials with increasing fine content of base materials, the effects of fine content may be observed more appropriately in Figure 10, where the scattering of D_{15bdy}/d_{85} versus fine content has been plotted. In other words, Figure 10 illustrates the concurrent effects of particle size distribution (PSD) and fine content of base materials on the no-erosion filter boundary. The correlation between these variables is governed by an exponential function and can be expressed as follows:

$$D_{15f} = d_{85} \times (0.0164 \times \exp(0.0672\ F) \quad (1)$$

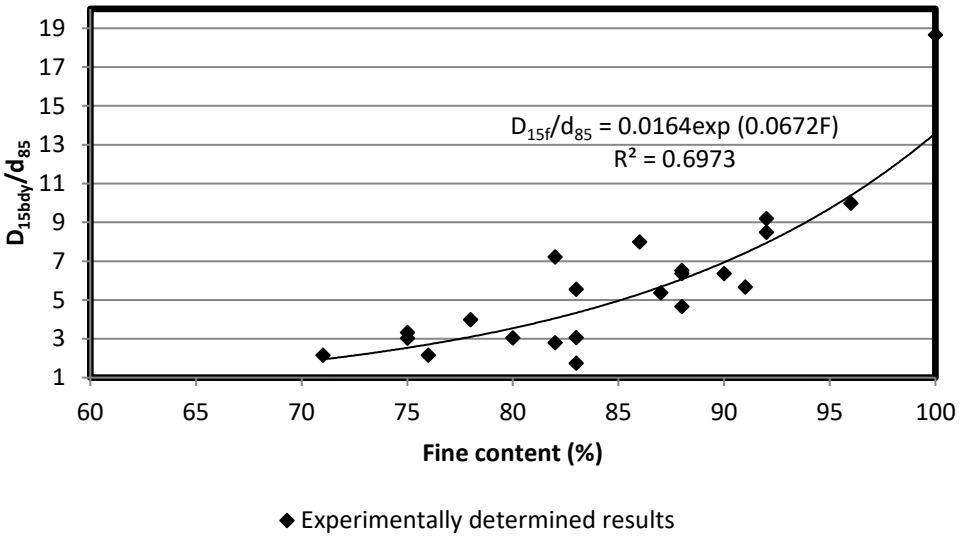


Figure 10. Variation of the fine content of the base soils against ratio of D_{15bdy}/ d_{85} for broadly graded, dispersive core materials

Decreasing D_{15bdy} size of required filter materials with increasing fine content of base soil materials was as expected. In other words, the base soil becomes finer or smaller as its fine content increases, and thus, finer filter materials are needed for retaining the erodible particles of base soil materials.

Variations in fine content were found to have significant effects on the no-erosion filter boundaries of base soils of Group 1, as observed in Figures 11.

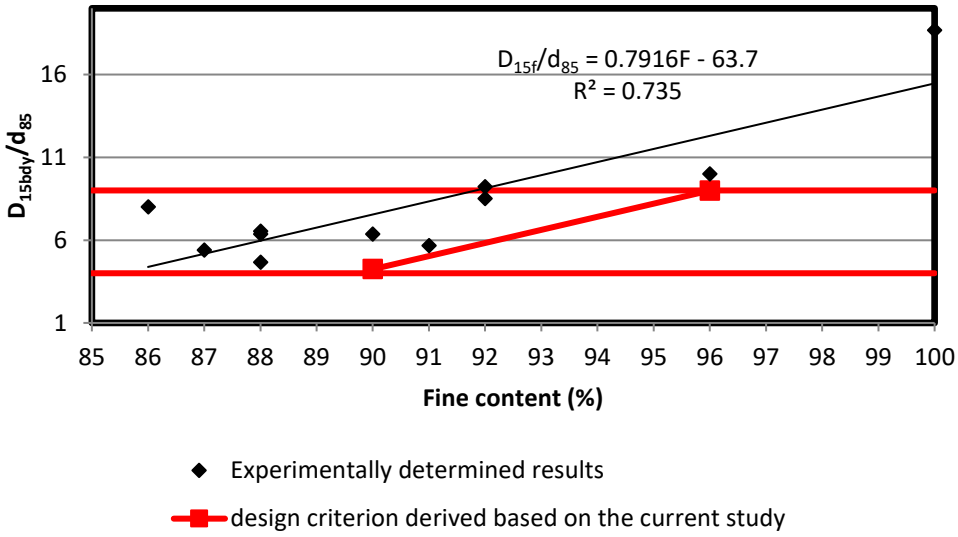


Figure 11. Suggestion a new design criterion for base soils of Group 1

Based on results plotted in Figure 11, safe filter materials could be designed by considering fine content and d_{85} size of base materials simultaneously as follows:

1- As long as the fine content of base materials is more than 85% but less than 90%, the criterion of D_{15f}/d_{85} = 4.0 could be applied.

2- For base soil material with fine content in the range of 90% to 96%, the criterion of D_{15f}/d_{85} = 0.7916F - 67.0 could be applied.

3- For base material with fine content more than 96%, the criterion of D_{15f}/d_{85} = 9.0 could be applied.

It is interesting to note that, although fine content was found to significantly determine the characteristics of required filter materials for base soils of Group 1, as observed in Figure 12, its effect on the no-erosion filter boundary of soil Group 2 is negligible.

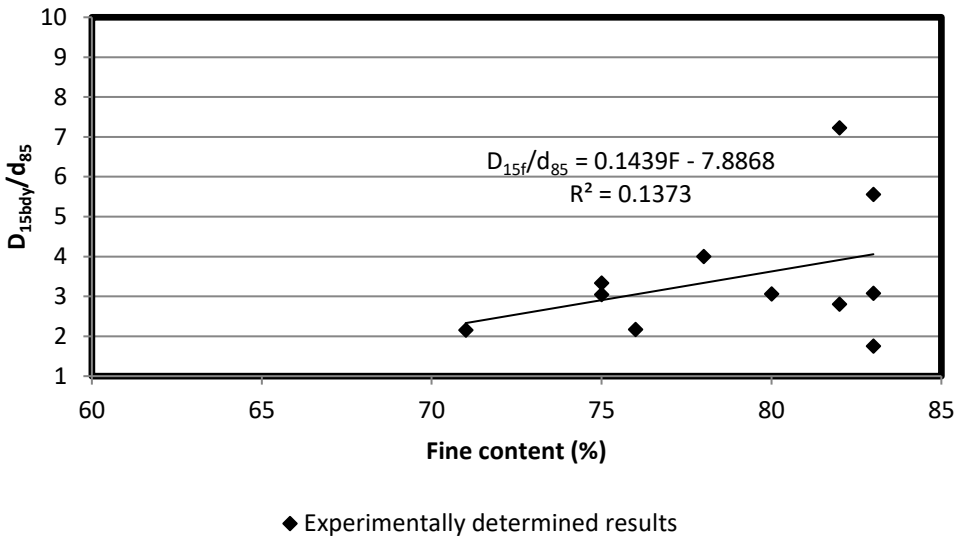


Figure 12. Variation of the fine content against ratio of D_{15f}/ d_{85} for Group 2

The hydraulic filter design criterion by Delgado et al. [30] for soils of Groups 1 and 2 is given together with experimentally determined filter requirements in Figure 13. Since only 2 out of 22 plots are placed below the line, following the criterion would mean having an erosion probability of only 9.0%, demonstrating the accuracy of the criterion suggested by Delgado et al. [30]. Although the criterion suggested by Delgado et al. [30] had a considerable factor of safety in relation to the base materials tested in this study, its application could become questionable for base soils Group 2 as the criterion has suggested filters with high permeability values.

Finally, designing filter materials by concurrently considering d_{85} and fine content of base materials seems to be more logical than separately using these effective parameters. Otherwise, it is recommended to design the required permeability of filter materials by considering the fine content of base materials and following a hydraulic criterion like Delgado et al. (2006).

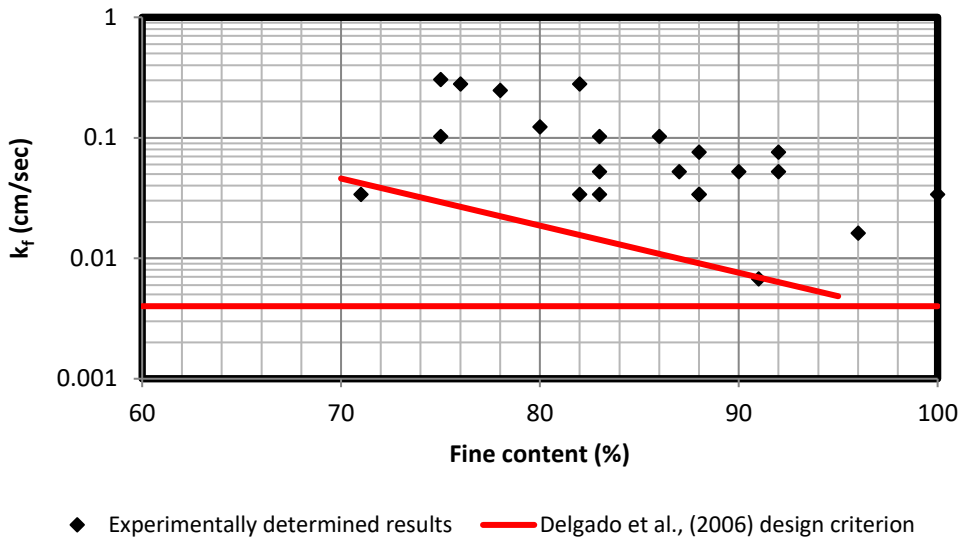


Figure 13. Comparison of the NEF test results with design criterion suggested by Delgado et al., [30]

4. Conclusions

As demonstrated in this research study, base soil plasticity was found to have negligible effects on no-erosion filter boundaries. In other words, results from the current study demonstrate that fine content could determine no-erosion filter boundary more substantially than clay content. Consequently, as experimentally determined by the current study, selecting the criterion of D_{15f}/d_{85} = 4.0 as the no-erosion lower bound could be logical for various broadly graded, cohesive, dispersive base materials of Group 1 with different clay content. Finally, only considering d_{85} as a base soil representative may result in inappropriate filter design. Therefore, in addition to the particle size distribution (PSD) of base materials, the effects of other base soil features such as fine content could be taken into consideration by using the formula $D_{15f} = d_{85} \times (0.0164 \times \exp(0.0672F))$. The study suggests categorizing base soils of Group 1 into several groups and designing filter materials as follows:

1- D_{15f}/d_{85}= 4.0 for 85%≤ F< 90%;
2- D_{15f}/d_{85} = 0.7916 F- 67.0 for 90%≤ F< 96%;
3- D_{15f}/d_{85}= 9.0 for F≥ 96%.

References

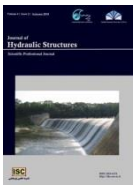
1. Falamaki A, Eskandari M, Baghlani A, Ahmadi SA (2013) Modeling total sediment load in rivers using artificial neural networks. Journal of Water and Soil Resources Conservation 2 (3)
2. Razavi SK, Hajialilue Bonab M, Dabaghian A (2020) Investigation into the internal erosion and local settlement of Esfarayen Earth-Fill Dam. Journal of geotechnical and geoenvironmental engineering 146 (4):04020006

3. Rather NA, Lone MA, Dar AQ, Mir BH (2021) Laboratory investigations for development of design criteria for varying shapes of protective filters. International Journal of Geotechnical Engineering
4. Vakili AH, Selamat MRb, Mohajeri P, Moayedi H (2018) A critical review on filter design criteria for dispersive base soils. Geotechnical and Geological Engineering 36:1933-1951
5. Vakili AH, Selamat MRB (2014) An assessment of veracity of filter criteria for earth dams. Proceedings of the Institution of Civil Engineers-Geotechnical Engineering 167 (6):574-584
6. Lone M, Hussain B, Asawa G (2005) Filter design criteria for graded cohesionless bases. Journal of geotechnical and geoenvironmental engineering 131 (2):251-259
7. Vakili AH, Selamat MRb, Salimi M, Farhadi MS (2021) Effect of water quality on the filtration of dispersive base soils. Arabian Journal of Geosciences 14:1-14
8. Reddi LN, Bonala MV (1997) Analytical solution for fine particle accumulation in soil filters. Journal of Geotechnical and Geoenvironmental Engineering 123 (12):1143-1152
9. Indraratna B, Vafai F (1997) Analytical model for particle migration within base soil-filter system. Journal of Geotechnical and Geoenvironmental Engineering 123 (2):100-109
10. Indraratna B, Trani LDO, Khabbaz H (2008) A critical review on granular dam filter behaviour–from particle sizes to constriction-based design criteria. Geomechanics and Geoengineering: An International Journal 3 (4):279-290
11. Indraratna B, Locke M (1999) Design methods for granular filters—Critical review. Proceedings of the institution of civil engineers-geotechnical engineering 137 (3):137-147
12. Indraratna B, Dilema E, Vafai F (1996) An experimental study of the filtration of a lateritic clay slurry by sand filters. Proceedings of the Institution of Civil Engineers-Geotechnical Engineering 119 (2):75-83
13. Falamaki A, Shafiee A, Eskandari M, Mohamadzadebabr K (2020) Choice of fiber-reinforced base material to reduce internal erosion mass transport. Arabian Journal of Geosciences 13:1-10
14. Khor CH, Yap SP, Leong GW (2024) Investigation of Piping Erosion in Embankment Dams with Downstream Filters. Journal of Geotechnical and Geoenvironmental Engineering 150 (6):04024041
15. Vakili AH, Salimi M, Keskin İ, Jamalimoghadam M (2024) A systematic review of strategies for identifying and stabilizing dispersive clay soils for sustainable infrastructure. Soil and Tillage Research 239:106036
16. Delgado-Ramos F, Poyatos JM, Osorio F (2012) Internal erosion of clayey soils protected by granular filters. La Houille Blanche 98 (4-5):42-47
17. Vakili AH, Bin Selamat MR, Abdul Aziz HB (2015) Filtration of broadly graded cohesive dispersive base soils. Journal of Geotechnical and Geoenvironmental Engineering 141 (5):04015004
18. Sherard JL, Dunnigan LP (1989) Critical filters for impervious soils. Journal of Geotechnical Engineering 115 (7):927-947
19. 422 AD (2000) Standard test method for particle-size analysis of soils. ASTM Intenational, West Conshohocken, PA, USA.

20. 4318 AD (2000) Standard test method for liquid limit, plastic limit, and plasticity index of soils. ASTM Intenational, West Conshohocken, PA, USA.
21. 4221-99: AD (2000) Standard test method for dispersive characteristics of clay soil by double hydrometer. ASTM Intenational, West Conshohocken, PA, USA.
22. 698 AD (2000) Standard test method for laboratory compaction characteristic of soil using standard effort (12400 ft-1br/ft3 (600 kN.m/ m3)). ASTM Intenational, West Conshohocken, PA, USA.
23. Soroush A, Shourijeh PT (2009) A review of the no erosion filter test. Geotechnical Testing Journal 32 (3):209-218
24. Das BM, Sobhan K (1990) Principles of geotechnical engineering.
25. Foster M, Fell R (2001) Assessing embankment dam filters that do not satisfy design criteria. Journal of Geotechnical and Geoenvironmental Engineering 127 (5):398-407
26. Lafleur J (1984) Filter testing of broadly graded cohesionless tills. Canadian Geotechnical Journal 21 (4):634-643
27. Ramos FD, Locke M (2000) Design of granular filters: Guidelines and recommendations for laboratory testing. Balkema, Rotterdam
28. Ali Zomorodian S, Moghadam MJ (2011) Investigation of effective parameters on the embankment dam filter behavior in simultaneous cracking in the core and filter. Geotechnical and Geological Engineering 29:637-644
29. Soroush A, Shourijeh P, Mohammadinia A (2011) Controlling internal erosion in earth dams and their foundations: Case studies. Criterion 15:9d85
30. Delgado F, Huber N, Escuder I, De Membrillera M Revised criteria for evaluating granular filters in earth and rockfill dams. In: Transactions of the International Congress on Large Dams, 2006. vol 3. p 445

© 2025 by the authors. Licensee SCU, Ahvaz, Iran. This article is an open access article distributed under the terms and conditions of the Creative Commons Attribution 4.0 International (CC BY 4.0 license) (http://creativecommons.org/licenses/by/4.0/).

Journal of Hydraulic Structures
J. Hydraul. Struct., 2024;11(2):61-86
DOI: 10.22055/jhs.2024.47416.1310



OPEN ACCESS

Investigating the Behavior of Jacket Offshore Steel Structure under Blast Loading

Farhad Hosseinlou [*1]
Wissam Asaad Ibrahim [1]
Mojtaba Labibzadeh [1]

Abstract

Given the hostile nature of offshore environments, ensuring the structural stability of offshore platforms is crucial to their design. A computer program was developed for the preliminary stability analysis of offshore platforms under significant environmental loads. The program output was applied to a minimum facility platform under extreme storm conditions, providing insight into its structural resilience. A comprehensive framework for experimental studies of the platform's stability was also established using a scaled physical model. This research investigates the effect of blasting loads and the distance of explosions on Steel Jacket Type Offshore Platforms (JTOPs) in both air and water environments. Simulations were conducted using Abaqus 2023, where four blasting loads (1, 2, 5, and 10 tons) were applied at varying distances (10, 20, 50, and 100 meters) from the structure. Results indicate that in water, the blasting wave increased by over 11 times as the distance from the platform increased, highlighting the significant amplification effect of the water medium. In contrast, the influence of the blasting load was considerably reduced in air, suggesting a notable difference in the platform's response to underwater versus atmospheric explosions. The displacement over time for different blast scenarios. At 0.5 seconds, the main model (2,000 kg at 20 meters) recorded the highest displacement, around 1.65 meters. Case 1, 2, 3, and 4 follow with displacements of approximately 1.35 m, 1.2 m, 0.95 m, and 0.7 m, respectively. Results indicate that displacement increases with higher blast loads and proximity, particularly in the water medium.

Keywords: Blast Loading; Jacket Offshore Structure; Strengthening; Numerical Analysis; Shock Wave.

Received: 11 July 2024; Accepted: 23 October 2024

[*] E-mail: F.hosseinlou@scu.ac.ir **(Corresponding Author)**
[1] Faculty of Civil Engineering and Architecture, Shahid Chamran University of Ahvaz, Ahvaz, Iran.

CC BY

1. Introduction

The increasing demand for alternative energy sources has led to significant rivalry between fossil fuels and other renewable energy sources since fossil fuels are considered non-renewable [1], [2]. Nevertheless, several contemporary platforms have included advanced technology derived from the preexisting offshore platforms (OSP) utilized in gas and oil exploration [3], [4], [5]. Significant progress has been achieved in ocean engineering, including a diverse array of inventive offshore structure configurations spanning from stationary to buoyant platforms. The structures encompassed in this category consist of floating liquid natural gas vessels, units of mobile offshore production, floating drilling production storage and offloading, units of floating generation, units of floating storage, units of floating offloading and storage, floating offshore wind turbines, jack-up rigs, and deep-water semi-submersible platforms [6], [7].

In recent decades, significant focus has been placed on studying the behavior of engineered structures when subjected to blast or impact loads [8]. Terrorist organizations worldwide are increasingly using explosives to target civilian buildings and infrastructure, posing a rising concern in contemporary communities [9]. Explosive devices have decreased in size and risen in power over the years, resulting in greater mobility of the explosive material and expanded range effects. The casualties from an explosion are often caused not just by immediate deaths resulting from the direct release of energy but primarily by structural collapses that may develop and lead to significant loss of life [10].

The issue of structural resistance to likely to explode loads was extensively studied for several years and made significant progress within the military community [11]. For this reason, most of these discoveries are not available to the public and are limited to military usage. However, design engineers may access documentation that enables them to forecast the impacts of an explosive detonation [12], [13].

The Steel Jacket Type Offshore Platforms (JTOPs) rank as one of the most utilized structures within the offshore oil industry of today [14]. As part of its design, JTOPs are generally intended to endure physical loads caused by waves, currents, wind, and earthquakes associated with the environment. As terrorist attacks have increased in recent decades, engineers have tended to pay more attention when designing structures to carry specific loads, such as explosives. In design codes, explosive loads are not considered comprehensively [15]. A variety of factors influence the effect of explosions, including the type of structure and its location, as well as the type, location, and intensity of the explosion. In the design of modern structures, it is necessary to prevent progressive collapse because of blasts [16], [17], [18]. Therefore, in the design of modern JTOPs, progressive collapse due to blast must be considered. It is essential to design so that the economic effects of failure are minimized as much as possible. The use of non-linear analyses can assist the designers in identifying weak points in structural systems subjected to blast and wave loads and reduce the likelihood of unfavorable Jacket platform failures [19], [20]. Pile-supported JTOPs are essential components of oil and gas exploration and production. It is important to note that pile-supported structures may face many lateral loadings; in some cases, they may also be subjected to strong waves and blasts, making assessing such structures' performance under blast loads an essential factor [21], [22], [23]. Considering the recent increase in terrorist attacks worldwide over the past few decades, researchers have begun to pay closer attention to specific loads, such as blast loads [17], [24]. Understanding the precise behavior of JTOPs under blast loads is necessary for developing methods for designing and fabricating structures resistant to explosive loads [25], [26].

Numerous research studies have examined the dynamic deformations of applying explosive blast stress on plates. The classification of failure modes of structures under impulse loading,

ranging from significant inelastic deformation to ripping and shear failure at the supports, was emphasized by Neuberger et al. [27], [28]. Shock tubes are a preferable alternative to explosives for generating shocks, and they are widely employed in shock/blast simulation research. The impact of blast loading on E-glass fiber-based composites and other materials was experimentally investigated by Tekalur et al. [29], [30], [31] via shock tubes and controlled explosive tube loading. The findings indicated that the E-glass fiber composite gradually deteriorated when subjected to high-rate loading, similar to the conditions reported by Hoo Fatt and Palla [32]. This deterioration was characterized by a progressive failure of the front face owing to indentation, followed by the entire collapse of the core. The investigations have been consistently advanced by the identical research group, yielding significant outcomes. These investigations have extensively investigated several factors, including the dispersion of blast energy throughout the impact procedure and the preservation of structural integrity in sandwich constructions subjected to blast pressures.

In comparison with previous study, the current study considered the first article that presents a strengthening for offshore structure against blasting load. As well as investigate the effect of the distance away from blasting location on the structural behavior under the blasting. This research is innovative as it bridges this gap by examining the behavior of JTOPs under different blast loads and explosion distances in both air and water environments. Using Abaqus 2023, this study performs comprehensive simulations of explosive loads on JTOPs, analyzing not only the structure's immediate response but also the progressive collapse mechanisms that might occur due to underwater explosions. By incorporating both media (air and water), the research brings new insights into the disparity of blast effects in different environments, an area not sufficiently addressed in current literature. This work could have profound implications for improving the design and safety of offshore platforms, minimizing the risk of catastrophic failure under blast loading, and guiding future non-linear analysis techniques for designing blast-resistant offshore structures. Using a 3-D model of the HE4 Platform in the Persian Gulf provides a detailed and realistic representation of the structure, crucial for accurate simulations of its behavior under environmental loads and blasting impacts. This approach accounts for the unique conditions of the Persian Gulf, such as water depth and wave patterns, ensuring the findings are region-specific. The model captures complex interactions between the platform and its environment, including the effects of blasting in both air and water, which enhances the accuracy of the analysis. By incorporating detailed geometries and structural components, the 3-D model allows for precise stress distribution and deformation analysis, leading to better design optimization and improved safety. This comprehensive approach ensures the study's conclusions are both relevant and practical for enhancing offshore platform resilience. However; the current study aims to investigate the effects of blast loading located on the behavior of jacket offshore steel structures as well as changing the blasting load with changing the distance to identify which load will effects more (small load near to structure or high load away the structure) to apply this idea 4 loads have been used (1, 2, 5 and 10) ton at (10, 20, 50 and 100)m away from the structure, the main reason for applying load on various distances to identify the effect of displacement, deformation and strength as well as identify the load amplification in water based on the distances. The responses of JTOP structure that subjected to blast loads induced by explosions on the water surface using three-dimensional (3D) Finite Element modeling and analysis as well as investigate the effect of structure strengthening by steel plate the behavior of JTOP under blasting load (2 ton at 20 m distance). As a method for representing JTOP behavior realistically, the present study uses numerical simulations based on non-linear material models.

2. Numerical Model and Simulation

2.1. Model Description

A case study is conducted using a 3-D model of a recently developed jacket platform in the Persian Gulf, known as the HE4 Platform. The platform's design and analysis adhere to the guidelines outlined in [33]. Given that several jacket platforms worldwide adhere to same design specifications, the findings of this study have the potential to be extrapolated to other comparable offshore platform behaviors. The water depth at the platform's position is 74.6 meters.

The vertical distance between the mudline elevation (elevation Ω74.4 m) and the top of the jacket elevation (elevation 9.2 m) of the jacket section of the platform is 83.6 m. Figure 1 depicts the configuration of the jacket as modeled in the ABAQUS program, as described by [34]. The platform under consideration is a jacket with four legs, exhibiting a damaged ratio of 1:10 in one row and a straight configuration in the other row. The absence of batter in a single row of legs is attributed to the presence of a Jack-up drilling platform in addition to the stationary platform [35]. The platform under consideration is representative of platforms often found in the Persian Gulf region [35], [36], [37].

The platforms used in other places have a similar arrangement of legs [38]. The jacket is comprised of four compartments that are reinforced. The jacket plan exhibits a square form at the working point level, measuring 23 m x 23 m. It is further expanded to 23 m x 31.53 m at the mudline height using the batter. A grouted section is formed by filling the space between the pile and leg with grout, resulting in a composite section. The cans and brace ends serve to enhance the structural integrity of all significant joints inside the jacket.

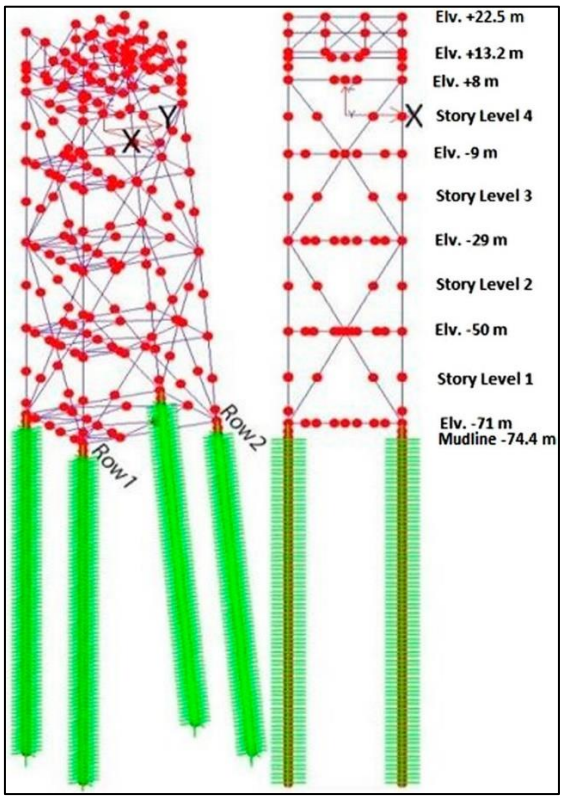


Figure 1. The configuration of the platform modeled in ABAQUS.

Four piles, each having a diameter =1.32 m and a wall thickness=5.5 cm, are used to support the jacket. It is significant to state that the analysis model utilizing ABAQUS software only includes the main structural features. The weight of the jacket under consideration in the analysis encompasses several components, such as the jacket construction, pile within legs, Boat Landing, Barge Bumpers, Anodes, and Mudmats. The weight of the deck encompasses several elements such as structural components, mechanical systems, electrical systems, instrumentation, and pipelines. These components are subjected to intense loads at all nodes of the deck.

2.1.1. Model Validation

It is crucial to comprehend both the UNDEX stresses and the reaction mechanisms of buildings that are most suitable for withstanding or reducing the impact of an explosion. The response of plates to a UNDEX event depends on many characteristics, including the peak pressure of the shock wave, the exponential decay, the effects of cavitation, the secondary and subsequent pulse loading, and the spatial and temporal fluctuation of the shock pulse on the structure. An intricate difficulty arises when attempting to describe and analyze the impact of UNDEX loads on structural elements/systems due to the combination of intense impact loading and a nonlinear structural response that includes both geometric and material non-linearities. Additionally, the characteristics of the material, including its sensitivity to strain rate, the influence of temperature, and metrics related to rupture and damage, change when subjected to dynamic loading and reaction.

The significant global conflicts of the world wars played a crucial role in advancing research related to UNDEX. Consequently, many controlled experiments were carried out aboard ships and submarines, with the results being systematically documented. Cole [39] provided one of the first extensive accounts, including experimental findings, theoretical assessments, and formulas to characterize the explosion and its pressure history. Shock Factor= 0.794, Charge mass=0.08kg, Standoff distance=0.15m. The current study dependent on Cole [39] to simulate the blasting load which is already taken from real explosion and the validation of the current structure under the selected blasting load is shown in Figure 2.

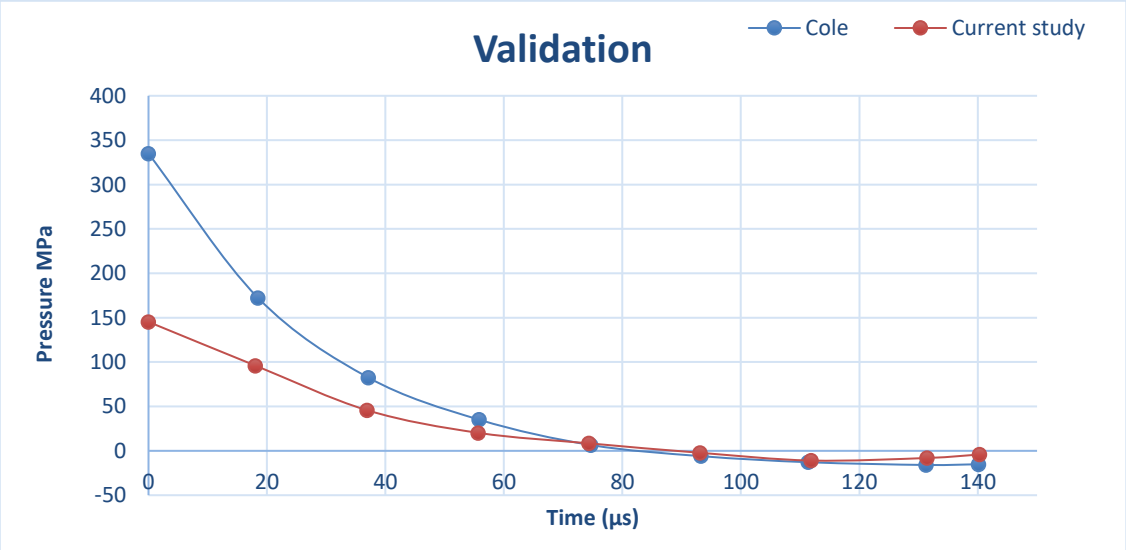


Figure 2. The validation model has been conducted based on Cole [39].

2.1.2. Finite element modeling

A Finite Element model of a newly deployed jacket platform in the Persian Gulf is used as a case study in this research. A numerical model of the experimental specimen is developed in ABAQUS, which is compared with the results in literature to validate the numerical model. A finite element model created in Abaqus is illustrated in Figure 3. Our next step was to mesh the model using B31 elements (A 2-node linear beam in space).

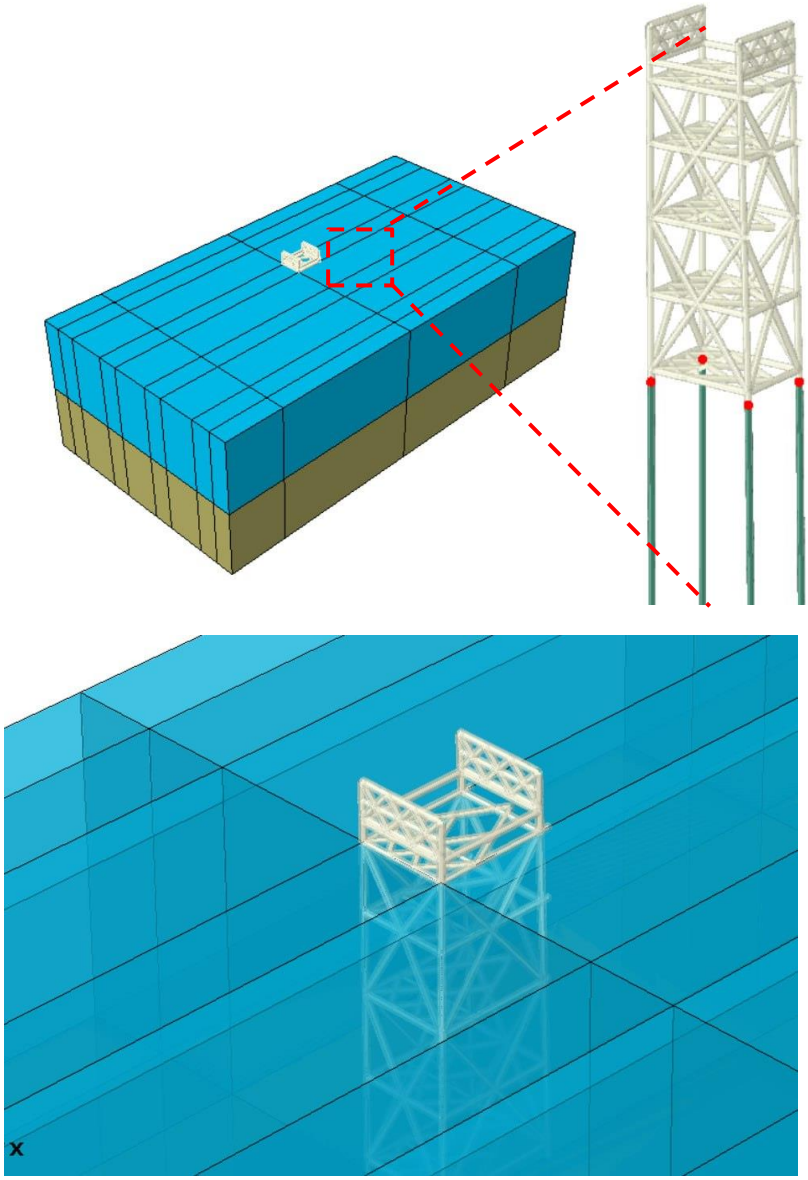


Figure 3. A finite element model designed in Abaqus.

The UNDEX Loading

Noncontact underwater explosions pose a significant risk to maritime vessels, including submarines and ships. Submerged structures may be classified into two groups based on the distance between the exploding charge and the target (standoff distance): far-field explosion and near-field explosion [40].

The pressure versus time history plot in Figure 3 illustrates the many events that took place throughout the UNDEX event [41]. Underwater explosions may result in many loading processes, such as hull cavitations, bulk, bubble-pulse loading, gas bubble oscillation, bottom reflection waves, free surface reflection waves and incident shock waves [42]. The compression wave resulting from the shock wave reflection from the ocean floor imposes an extra stress on the structure. The pressure generated by the shock wave is diminished due to the reflection of the shock wave from the surface of the open ocean [43], [44]. The shock wave generated by the UNDEX charge is referred to as the incident wave. The acoustic field produced by the interaction between the incident wave and the submerged structure is referred to as the dispersed wave. A spherical incident shock wave is used to describe the initial shock wave. This shock wave is delivered as a transient load on both the structural meshes and acoustic at their common surfaces, known as the wetted interface. The shock wave's distribution onto the plate is determined utilizing the incident pressure wave formulas, as illustrated in reference [45].

In this study, gravitational loading was considered as a critical factor in the overall structural analysis of the jacket offshore platforms. Gravitational loading, primarily due to the platform's self-weight and the additional weight of equipment and materials, was modeled as a constant vertical load acting on the structure. This includes both dead loads (permanent structural and equipment weight) and live loads (temporary or variable loads such as operational equipment and personnel). The gravitational load was incorporated in the simulations alongside other environmental forces (e.g., wave, wind, and blast loads) to assess the combined effects on the platform's structural performance. This approach ensures a comprehensive evaluation of the platform's stability, considering the influence of both static and dynamic loads on its integrity and resistance to collapse. Based on the API RP 2A-WSD (American Petroleum Institute) provides specific guidelines on calculating gravitational loads, which have been considered in this study. Furthermore, the ISO 19902 standard also addresses the treatment of gravitational forces in the design of offshore steel structures.

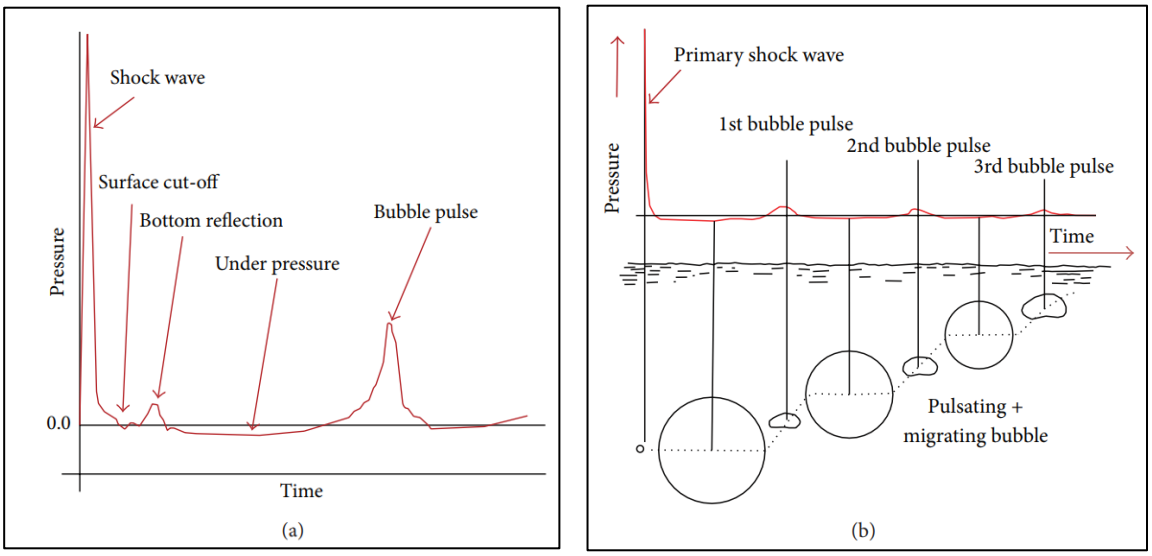


Figure 4. UNDEX Phenomenon: high pressure bubble and shock wave [41].

The pressure history of the shockwave at a stationary position, denoted as P(t), begins with an immediate pressure peak, P_{max}, and then a subsequent decrease that is often represented by an exponential function. The pressure profile equation, as obtained by empirical methods [39], [40], [46], may be expressed in a way that follows.:

$$P(t) = P_{\max} e^{-((t-t_1)/\theta)} (\text{MPa})\ t \geq t_1 \tag{1}$$

Whereas
t refers to the duration elapsed after the charge detonation in (msec)
t_1 refers to the arrival shock wave duration to the target after the charge detonation (msec);
$P_{\max}$ refers the peak pressure value (MPa) at the front wave shock;
θ refers to the decay duration constant that depicts the exponential decay in (m.sec) and is equal to the duration detected by the peak pressure to fall to $1/e$ durations its initial magnitude.

The magnitude of the blast and the distance from the charge where the pressure is recorded determine the decay constant and peak pressure. The expression for the peak pressure, denoted as $P_{\max}$, and the decay constant, denoted as θ, is as following [47]:

$$P_{\max} = K_1 \left(\frac{W^{1/3}}{R}\right)^{A_1} (\text{MPa})$$
$$\theta = K_2 W^{1/3} \left(\frac{W^{1/3}}{R}\right)^{A_2} (\text{millisecond (msec)}) \tag{2}$$

The max bubble radii of exploding gas, $R_{\max}$, and the initial pulsation periods, T, are presented in the case of TNT charge [48]:

$$\begin{aligned} R_{\max} &= 3.38\left(\frac{W}{(D+10.3)}\right)^{1/3} \text{ (m)} \\ T &= 2.1\frac{W^{1/3}}{(D+10.3)^{5/6}} \text{(sec)}, \end{aligned} \tag{3}$$

The constants K1, K2, and A1, A2 are contingent upon the kind of explosive charge used in the utilization of various explosives. The input constants listed in Table 1 [49] are as follows. The explosive charge weight is denoted as W in kilograms (Kg), the charge depth is represented as D in meters (m), and the distance between the exploding charge and the target is denoted as R in meters (m). In addition, Cole [39] offered more details on the methodical exposition of physical consequences linked to underwater explosives.

Table 1: The variables of shock waves for different exploding charges.

Constants	Explosive material kind			
	HBX-1	TNT	PETN	Nuclear
K1	53.51	52.12	56.21	1.06E4
A1	1.144	1.180	1.194	1.13
K2	0.092	0.0895	0.086	3.627
A2	-0.247	-0.185	-0.257	-0.22

Taylor's plate theory may be used to precisely forecast the reflecting pressure on the fluid-structure interaction surface once pressure from an underwater explosion impacts a flexible surface, including the hull of a surface ship [40]. In the case of an air-supported plate with a mass per unit area (m) and exposed to an incident plane shockwave, denoted as $P_i(t)$, a pressure reflection wave, denoted as $P_r(t)$, exits the plate while it is in motion at a velocity $v_p(t)$. The application of Newton's second law of movement,

$$m \cdot \frac{dv_p}{dt} = P_i + P_r \tag{4}$$

The velocities of the fluid particles behind the incident and reflected shockwave are denoted as $v_i(t)$ and $v_r(t)$, respectively. Consequently, the velocity of the plate is determined.

$$v_p(t) = v_i(t) - v_r(t) \tag{5}$$

The incident shockwave pressure $P_i = \rho_f c v_i$, whereas the reflecting shockwave pressure $P_r(t) = \rho_f c v_r$. In this equation, ρ_f represents the fluid density and c represents the acoustic velocity. By replacing the pressure in equation (4) and solving it with equation (1), the value of $P_r(t)$ is obtained.

$$P_r(t) = P_i(t) - \rho_f c v_p = P_{\max} e^{-((t-t_1)/\theta)} - \rho_f c v_p \tag{6}$$

Equation (4) can then be rewritten as

$$m \cdot \frac{dv_p}{dt} + \rho_f c v_p = 2P_{\max} e^{-((t-t_1)/\theta)} \tag{7}$$

Differentiating (7) yields the following expression for plate velocity, where $\psi = \rho_{fC\theta}/m$ and $t > 0$. The total pressure on the plate is

$$P_t(t) = 2P_i(t) - \rho_f c v_p = \frac{2P_{\max}}{1-\psi}\left[e^{-((t-t_1)/\theta)} - \psi e^{-\psi(t-t_1)/\theta}\right] \tag{8}$$

A shock factor (SF), which is proportional to the energy density of the shockwave arriving at a structure, due to various combinations of charge weight and standoff distance is derived by

$$\mathrm{SF} = \frac{0.45\sqrt{w}}{R}\left(\frac{\mathrm{Kg}^{1/2}}{\mathrm{m}}\right) \tag{9}$$

The study simulates underwater explosions (UNDEX) using Abaqus software, modeling the impact of varying blasting loads (1, 2, 5, and 10 tons) and explosion distances (10, 20, 50, and 100 meters) on the offshore structure. Key parameters include the magnitude of the blast, the distance from the structure, and the medium (air or water) to assess how these factors influence the impact. The simulation models the pressure waves generated by the explosion and their interaction with the platform. It also analyzes the structural response, focusing on stress distribution and deformation to evaluate stability and potential damage. This approach provides a comprehensive understanding of how different explosion scenarios affect the structural integrity of offshore platforms.

2.2. Elements mesh details

To determine the best mesh density (i.e., number of elements), selecting a suitable mesh size is a significant step in FEM. Structure models were subjected to a convergence analysis to obtain an appropriate mesh size by dividing Structure models into an appropriate number of elements. When the reduction in mesh size (increment in the elements' number) has no effect on the finding, the findings have reached a suitable convergence.

To identify the appropriate mesh size for each modeled component, a sensitivity analysis was conducted. This involved altering the mesh size in various sections of the system and obtaining the findings of the frequency analysis. By performing this sensitivity analysis, the optimal mesh size for each component could be determined, ensuring accurate and reliable frequency analysis findings as illustrated in Figure 5.

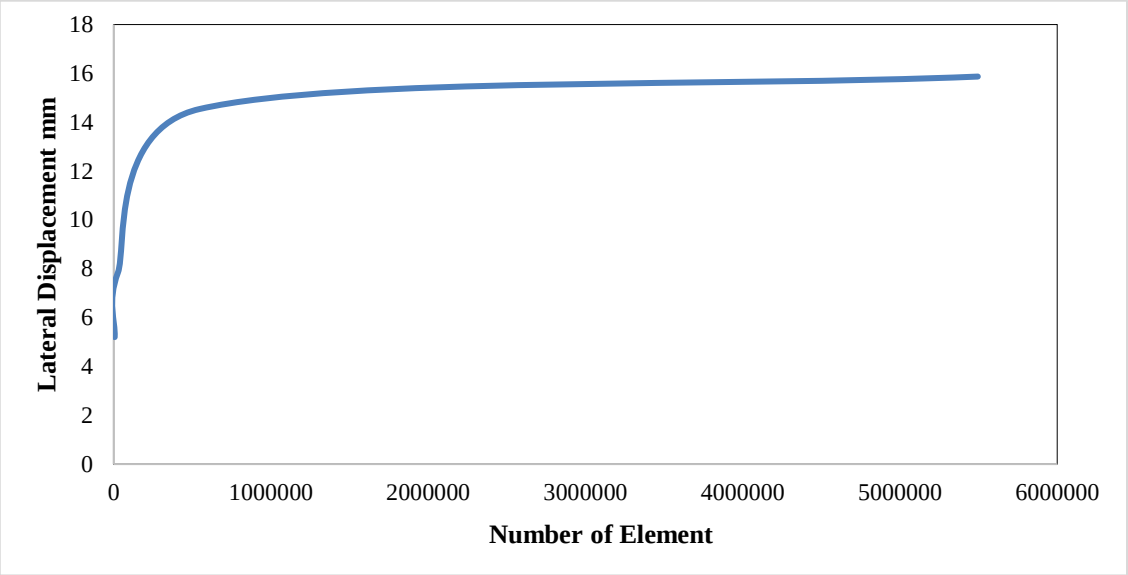


Figure 5. the mesh accuracy based on the lateral loading.

2.3. Assigning Boundary Condition

The jacket offshore steel structures analyzed in this study are designed and reinforced in accordance with internationally recognized standards and guidelines commonly adopted for offshore platforms, particularly within the oil and gas sector. **API RP 2A-WSD (American Petroleum Institute),** which recommended practice governs the planning, design, and construction of fixed offshore platforms, offering comprehensive guidelines on structural integrity, safety factors, and the consideration of environmental loads such as wind, wave, and seismic forces. And **ISO 19902 (International Organization for Standardization)**, which addresses the requirements for offshore steel jacket structures, including design, construction, and maintenance. It covers loads, materials, structural components, and fatigue analysis. Numerous elements for simulating the behavior of steel structure were applied. These components are commonly utilized in ABAQUS. The details of the elements and their descriptions are shown in the table below.

Table 2. The element type and description.

No.	Name of materials	Type of Element	Symbol	Descriptions
1	Steel	beam	B31	2-node beam element with linear interpolation formulations in three-dimensional space
2	Steel plate	Shell	S4R	4-node double curved thin of thick shell, reduced integration, hourglass control, finite membrane strain
3	Soil and waster	Deformable solid	C3D8R	8-node brick element

The boundary situations have an essential role in accurately forecasting the behavior of the model. In this thesis nine strengthen type had been made for each of the four model as can be seen in the attached excel file, the types of strengthen are describes below:

2.3.1. Case 1

In this Case two parallel steel plates that has placed at the 10 m away of the edge with 72 circular hole (with radius 0.5m) the distance between holes is (3 m horizontally and 2.5m vertically) as illustrated in Figure 5 and 6.

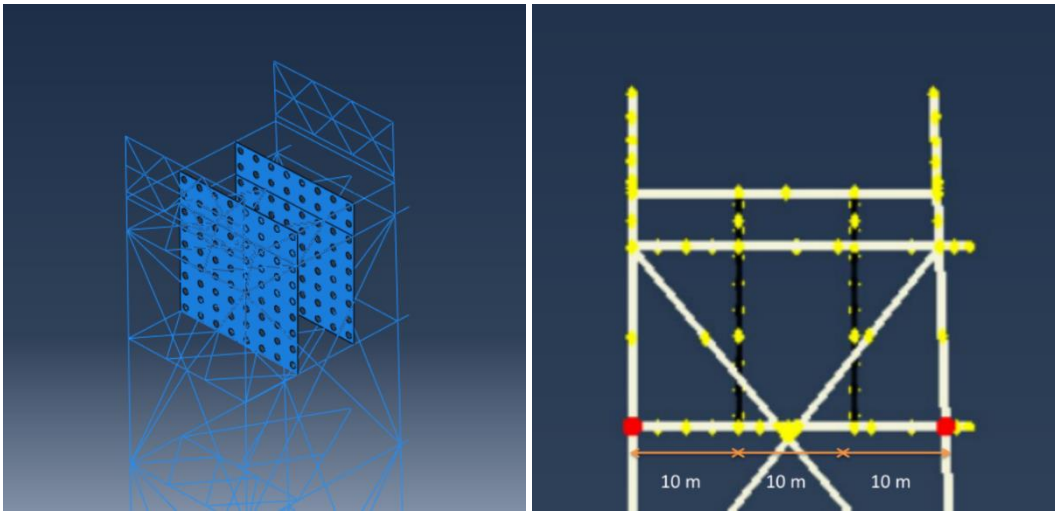


Figure 6. Front view of first strengthening case.

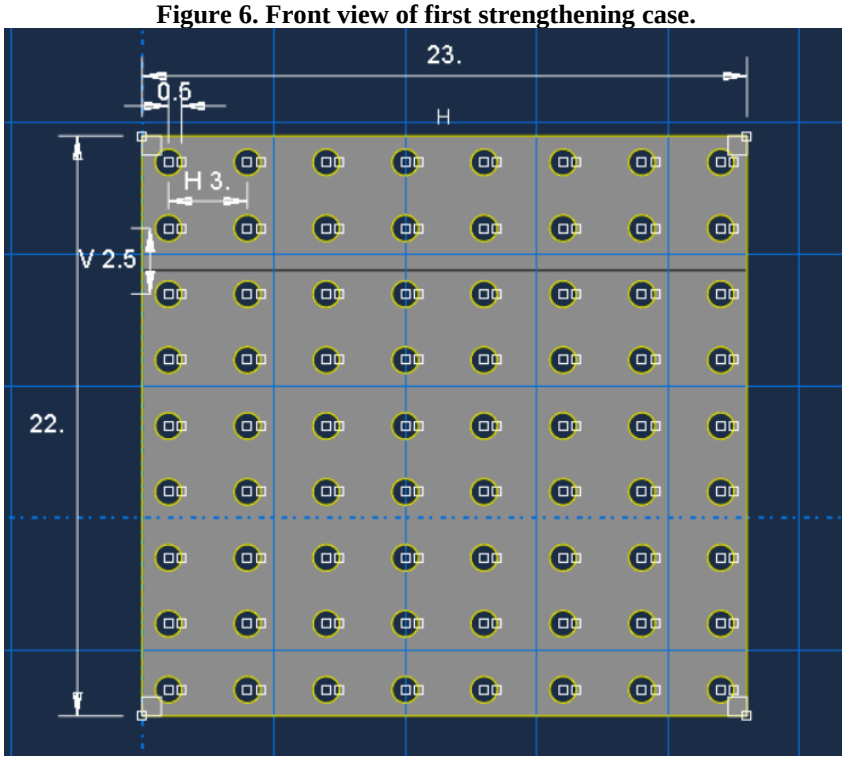


Figure 7. First strengthening case dimensions details.

2.3.2. Case 2

This Case consists of two parallel steel plates with same dimensions as case one (one of the plates placed at 5 m away of the edge and the other one placed at 15 m away from the structure edge the distance between two plates is 10 m) with 72 circular hole (with radius 0.5m) the distance between holes is (3 m horizontally and 2.5m vertically) as illustrated in Figure 7.

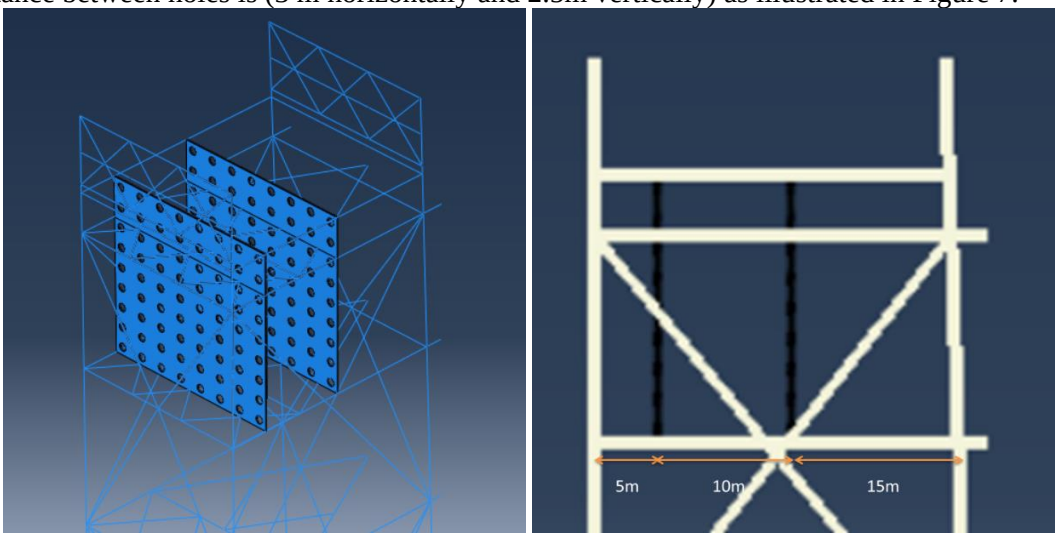


Figure 8. Front view of second strengthening case.

2.3.3. Case 3

This Case consists of two parallel steel plates with same dimensions as case one (both plates have been placed at the edge of the structure) with 72 circular hole (with radius 0.5m) the distance between holes is (3 m horizontally and 2.5m vertically) as illustrated in Figure 8.

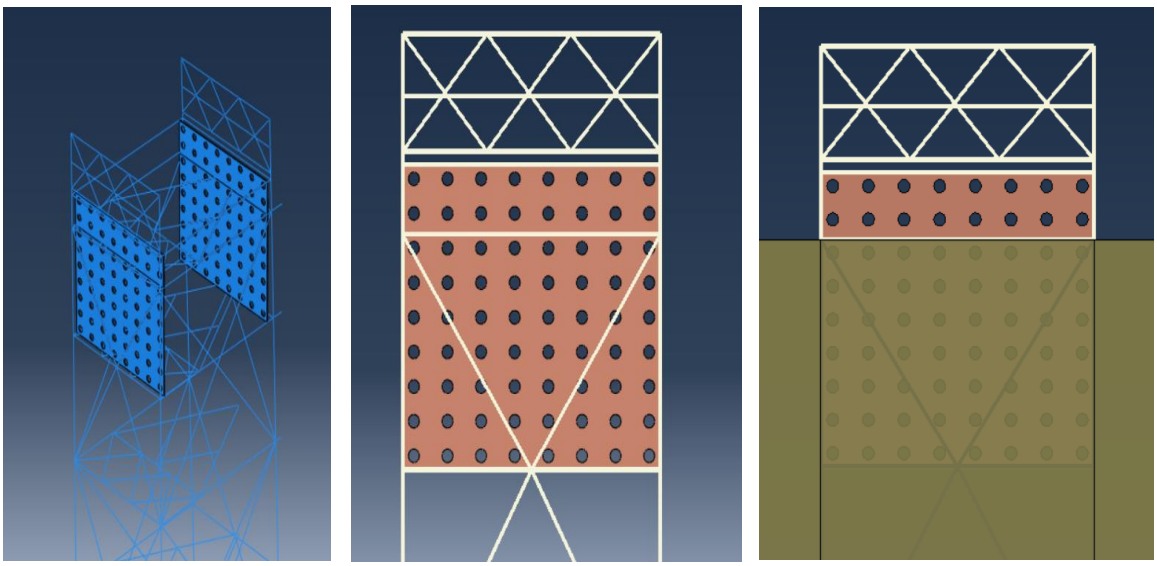


Figure 9: Front view of third strengthening case.

2.3.4. Case 4

This Case consists of four steel plates with same dimensions as case one (they placed at four structure edge one at each edge) with 72 circular hole (with radius 0.5m) the distance between holes is (3 m horizontally and 2.5m vertically) as illustrated in Figure 9.

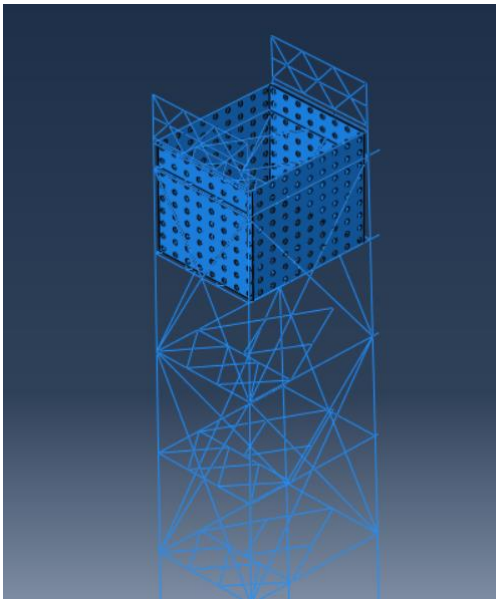


Figure 10. Front view of sixth strengthening case.

3. Results and Discussions

The obtained results from ABAQUS software program have been classified into the following sections:

3.1. Blast load and displacement

The relationship between displacement that occurred due to different blasting loads (1, 2, 5 and 10) ton and time as shown in Figures 10-13. Figure 10 shows that applying blasting load with 1 ton at 10 m distance away from the offshore steel structure was mainly affected by the transition media of load where the water increasing the impact load significantly from 0.223043 to 0.906891, which means the presence of water increase the blasting load more than 3 time its effect on air and this results are compatible with Jang et al., [50] they found that the water increase the blasting load with 2.6 time compare with air. The presence of water significantly amplifies the impact of blast loads compared to air. Water's higher density and lower compressibility facilitate more efficient transmission of blast energy, leading to increased structural displacement and deformation. The fluid nature of water also causes blast waves to expand, intensifying their effect on structures. Consequently, the same blast load results in a substantially greater impact when in water than when in air.

Figure 11 shows that applying blasting load with 2 ton at 20 m distance away from the offshore steel structure was mainly affected by the transition media of load where the water increasing the impact load significantly from 0.149723 to 1.65706, which means the presence of water increase the blasting load more than 11 time its effect on air and increasing the distance between the structure and source of explosion in air comparison with Figure 11, but in water

increasing the distance lead to expansive the wave [51] and this results are compatible with results obtained by [52] which show that the blasting wave has been expanded in water due to water fluidity. Same results have been shown in Figures 12 and 13 when applying 5 and 10 ton at 50 and 100 m distances, respectively. The amplification of blast loads in water is attributed to the medium's higher density and lower compressibility compared to air, which facilitates more efficient wave propagation. This results in greater energy transfer to the structure, intensifying the blast wave's effect. Additionally, the fluid properties of water cause the wave to disperse, further enhancing the overall impact on the structure.

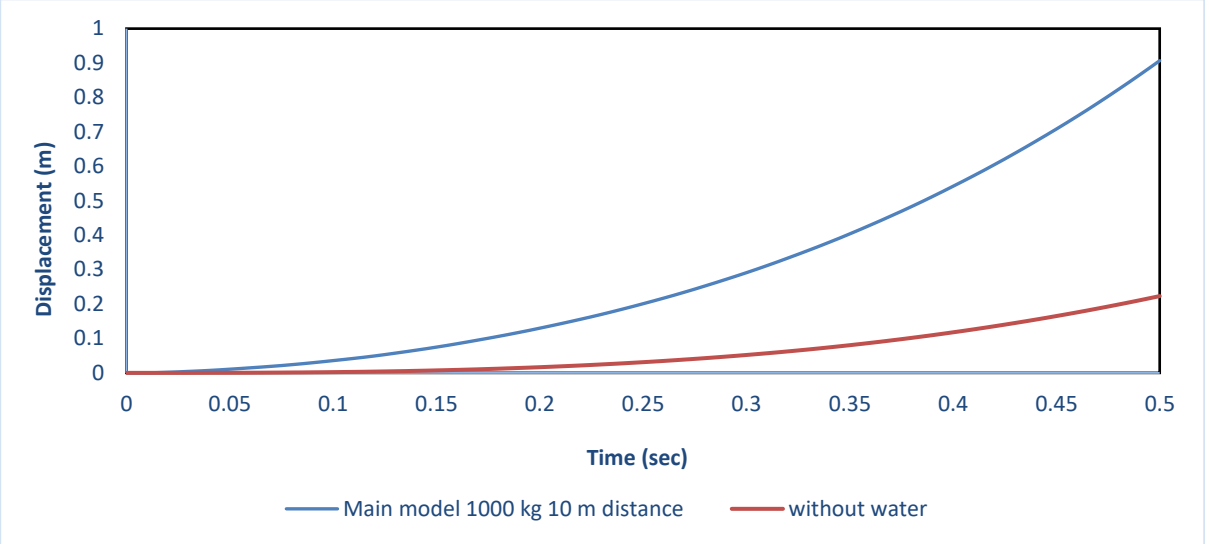


Figure 11. The relationship between displacement and time for JTOPs for blast load 1 ton at 10 m.

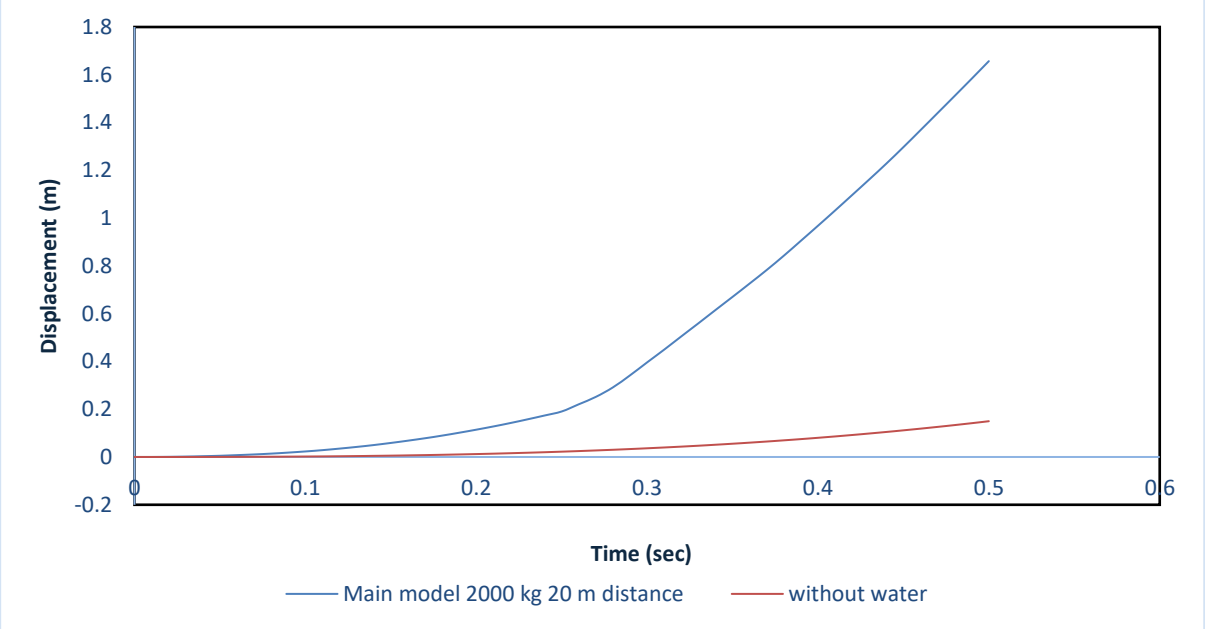


Figure 12. The relationship between displacement and time for JTOPs for blast load 2 ton at 20 m.

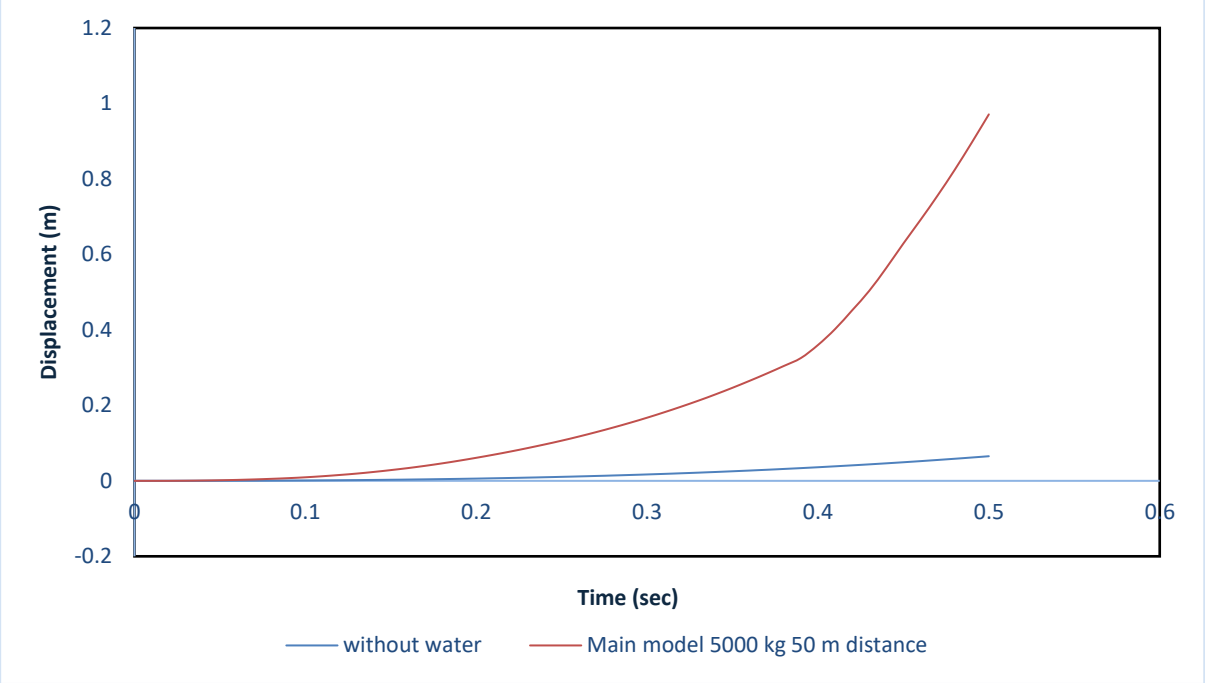


Figure 13. The relationship between displacement and time for JTOPs for blast load 5 ton at 50 m.

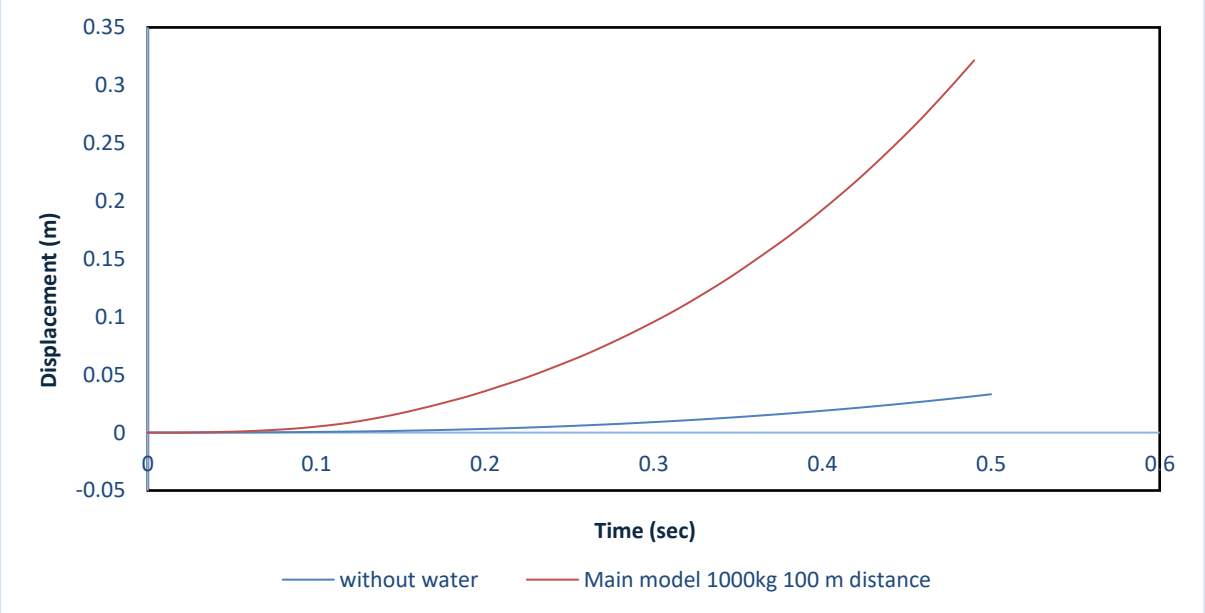


Figure 14. The relationship between displacement and time for JTOPs for blast load 10 ton at 100 m.

3.2. Structure Deformation

The structure deformation for all selected blasting loads (1, 2, 5 and 10) tons has been shown in figures 14-17. Based on Figure below increasing the distance between applying load and the source of applying lead to reduce the deformation of structure in air and increasing the deformation in water.

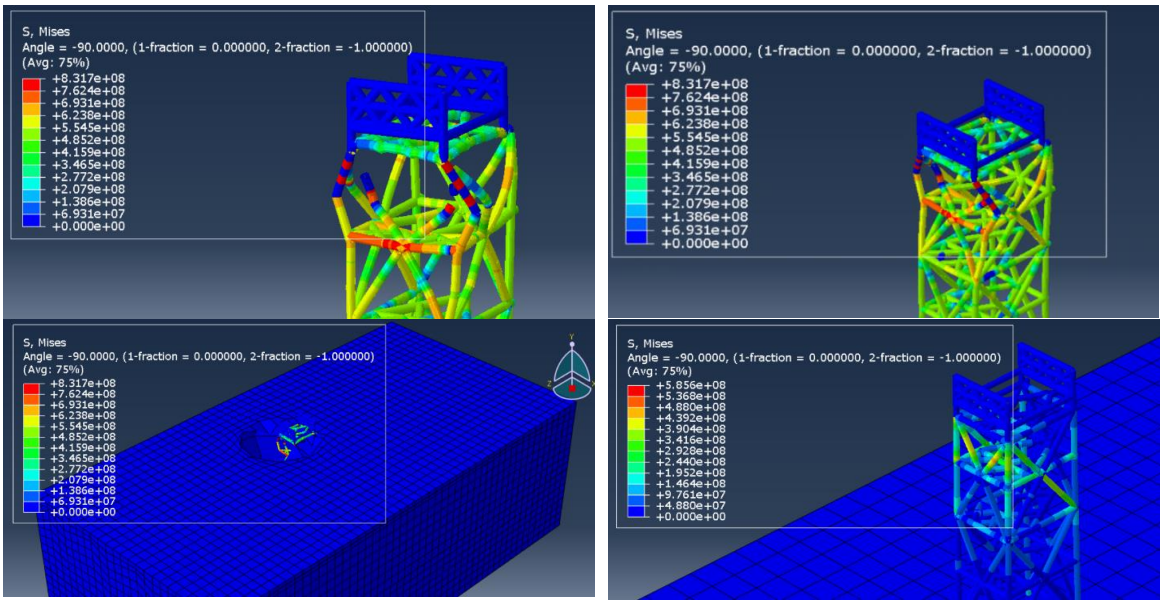


Figure 15. The deformation of JTOPs for blast load 1 ton at 10 m.

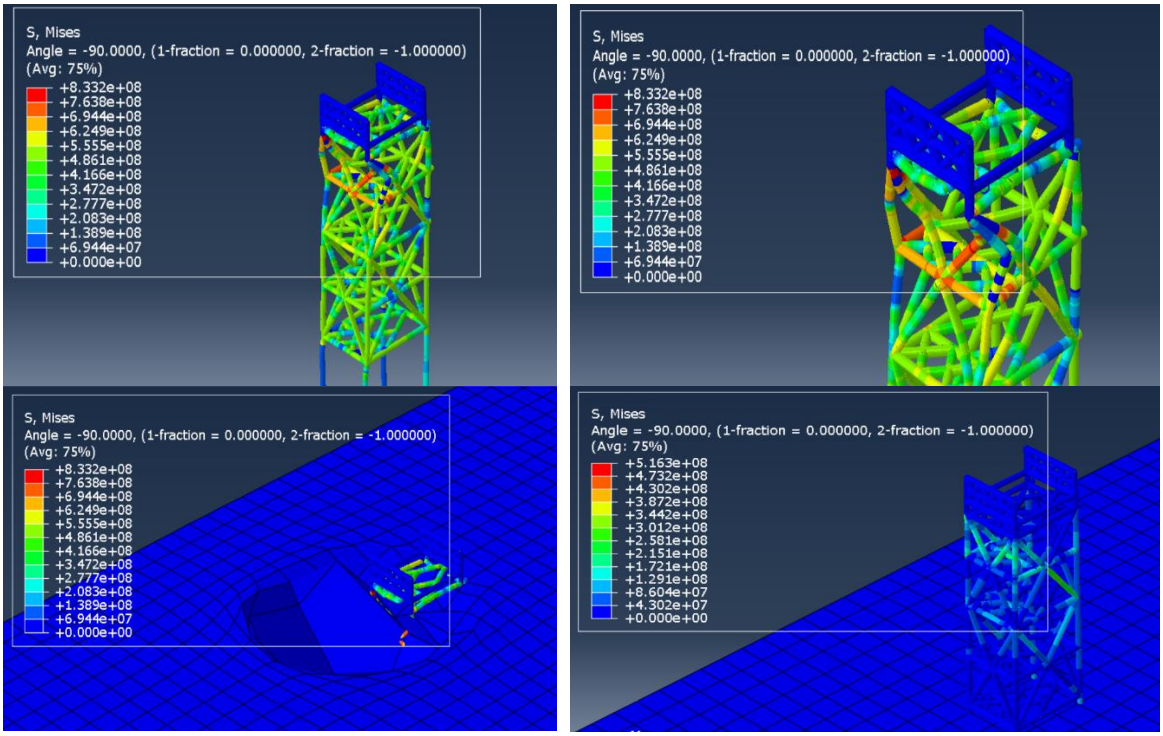


Figure 16. The deformation of JTOPs for blast load 2 ton at 20 m.

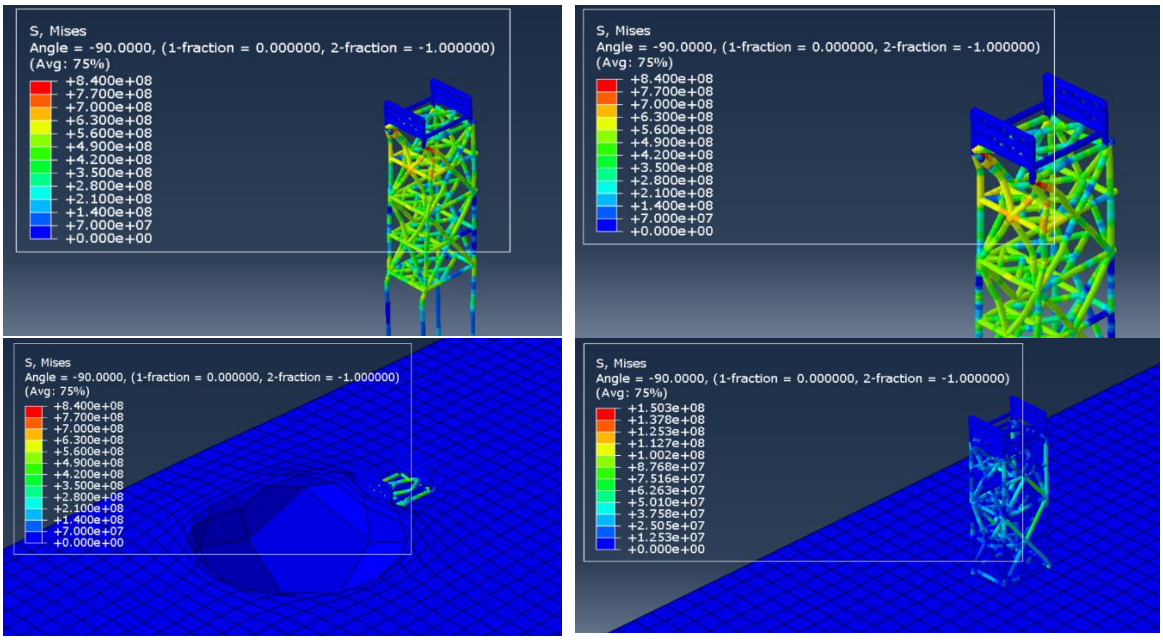


Figure 17. The deformation of JTOPs for blast load 5 ton at 50 m.

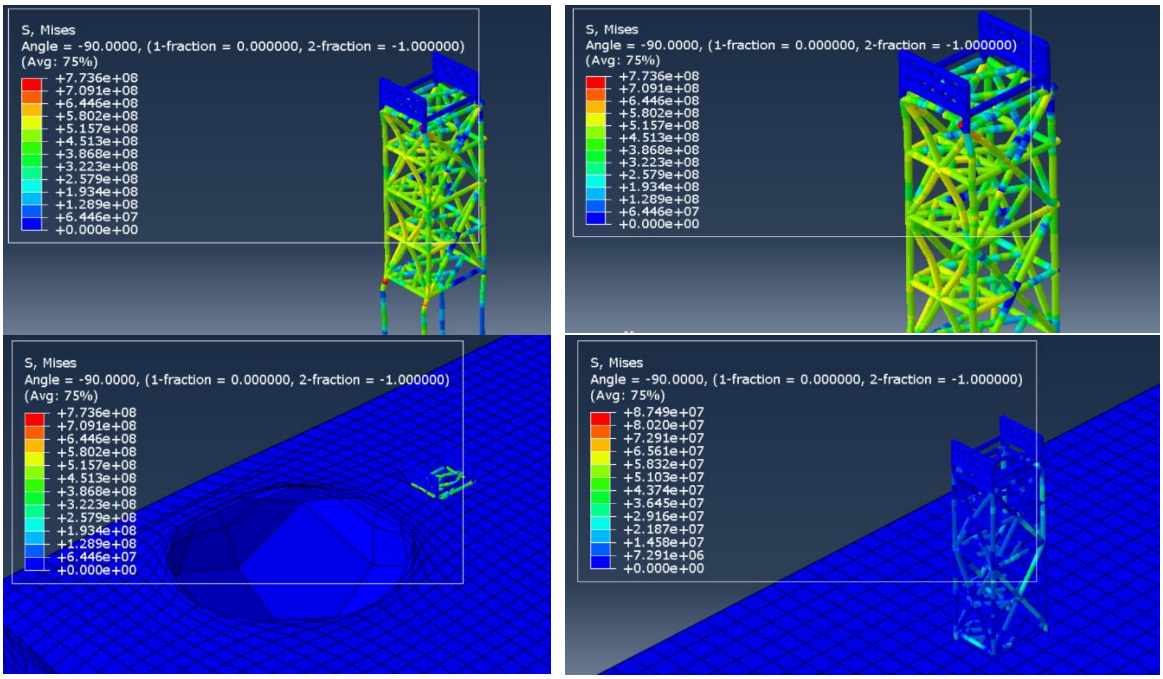


Figure 18. The deformation of JTOPs for blast load 10 ton at 100 m.

3.3. Strengthening Structure

3.3.1. Blast load and displacement

Figure 18 shows that applying blasting load with 2 ton at 20 m distance away from the offshore steel structure was changed based on the strengthening case, where case 5 with single parallel steel plate has the highest displacement, while case 8 with steel slices has been placed on four offshore structure's sides has the lowest displacement.

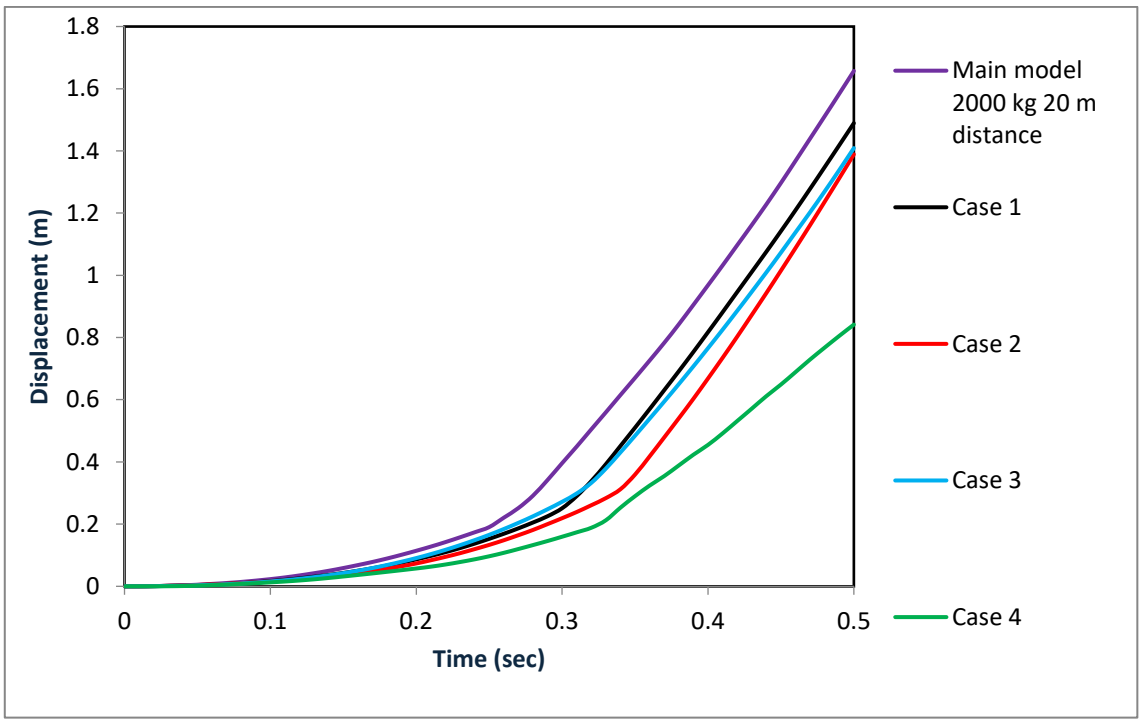


Figure 19. The relationship between displacement and time for strengthened JTOPs subject to blast load 2 ton at 20 m.

3.3.2. Structure Damaging

Figure 19 shows that applying blasting load with 2 ton at 20 m distance away from the offshore steel structure was changed based on the strengthening case, where case 5 with single parallel steel plate has the highest displacement value 2.54489m, while case 8 with steel slices has been placed on four offshore structure's sides has the lowest displacement value 0.282685m. The relationship between displacement and damage is a positive relationship, therefore Case 4 has the lowest damaging and best condition to resist the explosion, while case 1 has highest damaging and worst condition against the same explosion.

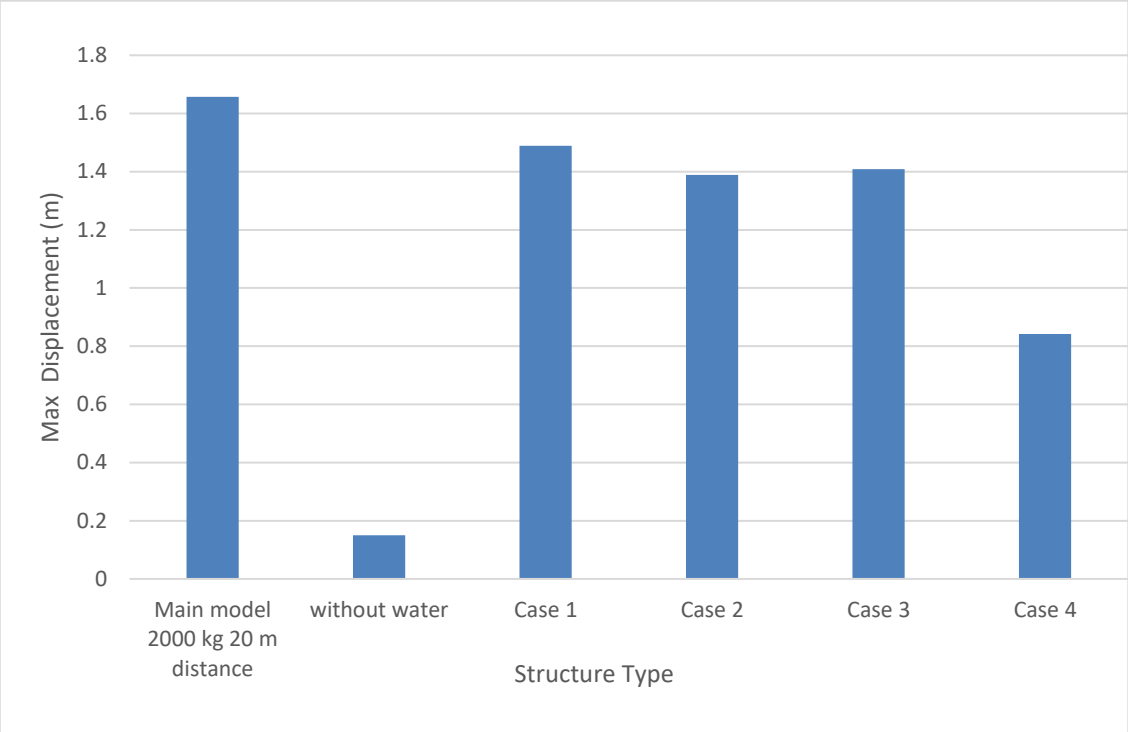


Figure 20. Max displacement value for model 2 ton and 20 m displacement with different strengthening.

3.3.3. Structure Deformation

Figure 20 to 22 show the offshore structure deformation simulation for different strengthen cases by ABAQUS software program using 2 ton blasting load located at 20 m away from the structure. Figure 20 shows the offshore structure deformation for case 1 that strengthening with two parallel steel plates at the middle of the structure. The structural deformation has been reduced after placing symmetrical strengthening. Figure 21 shows reduction in deformation of the structure in one side due to unsymmetrical strengthening of the offshore structure.

Figure 22 shows increment in the structural deformation after placing the steel plates at the edge of the structure, due to increasing the structural resistance against the blast load that happened when increasing the surface area of that effected by blasting load and that compatible with [53].

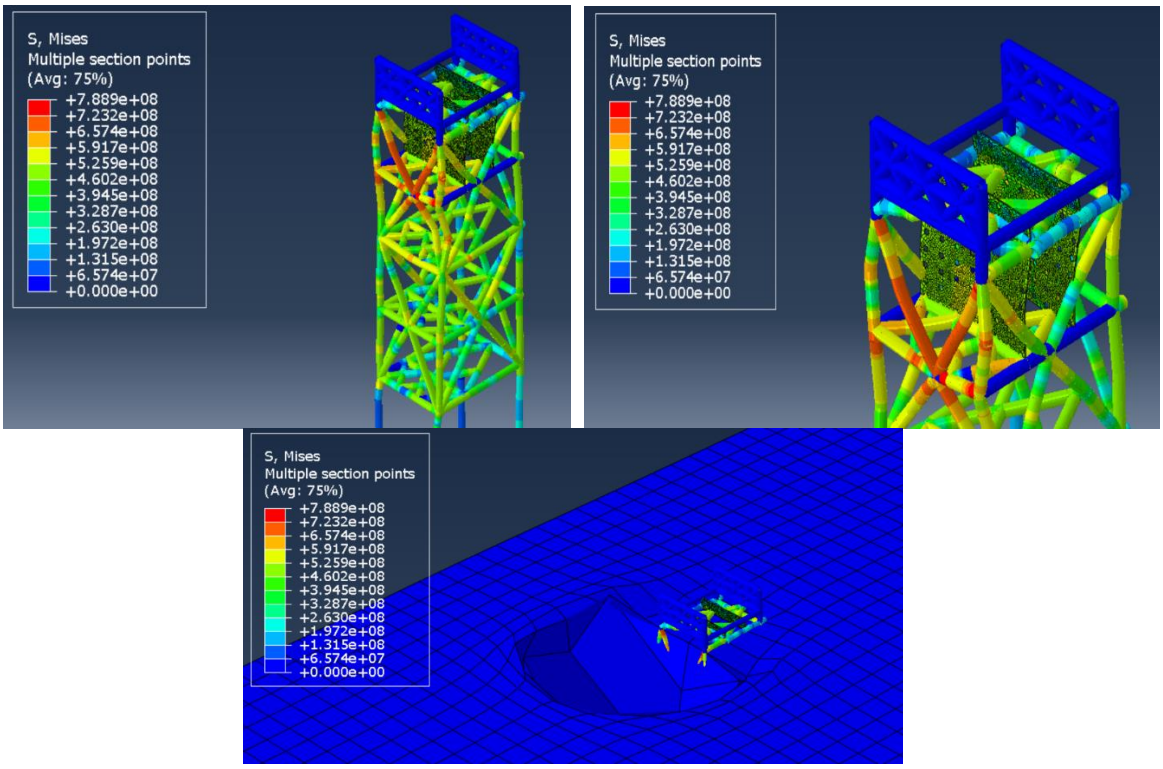


Figure 21. Strengthened offshore structure Case 1 with 2 ton loading and 20 m distance

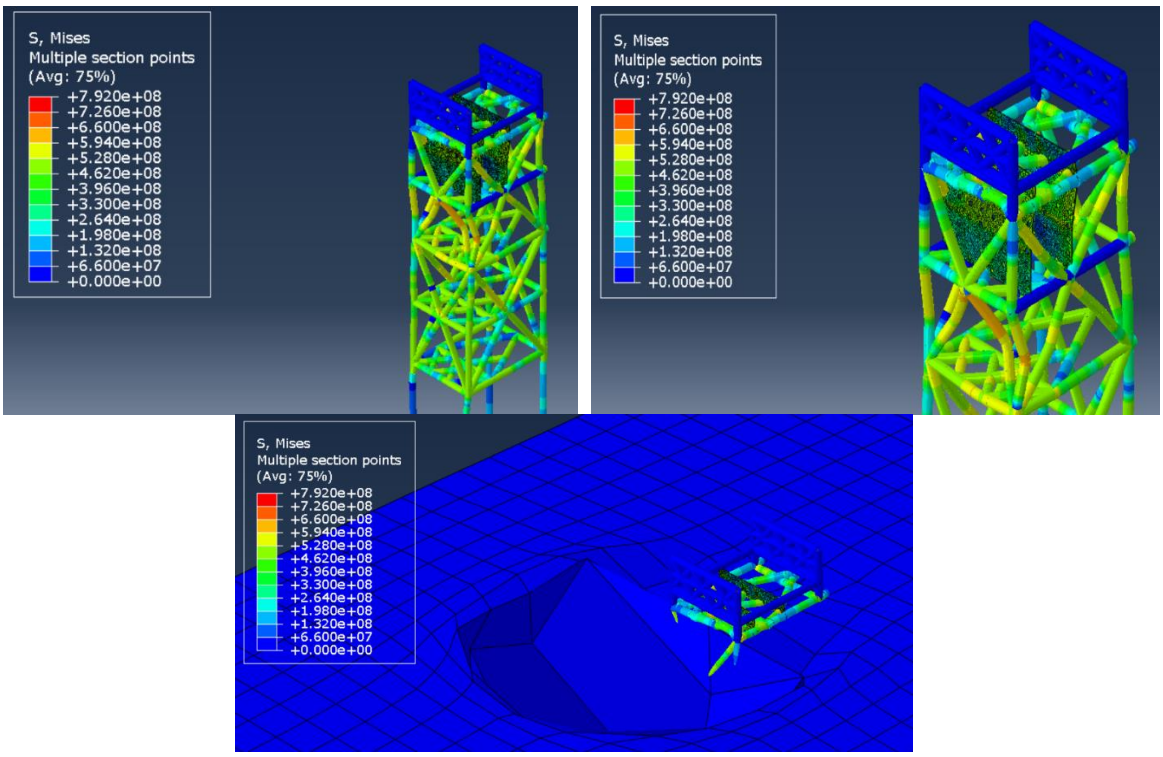


Figure 22. Strengthened offshore structure Case 2 with 2 ton loading and 20 m distance

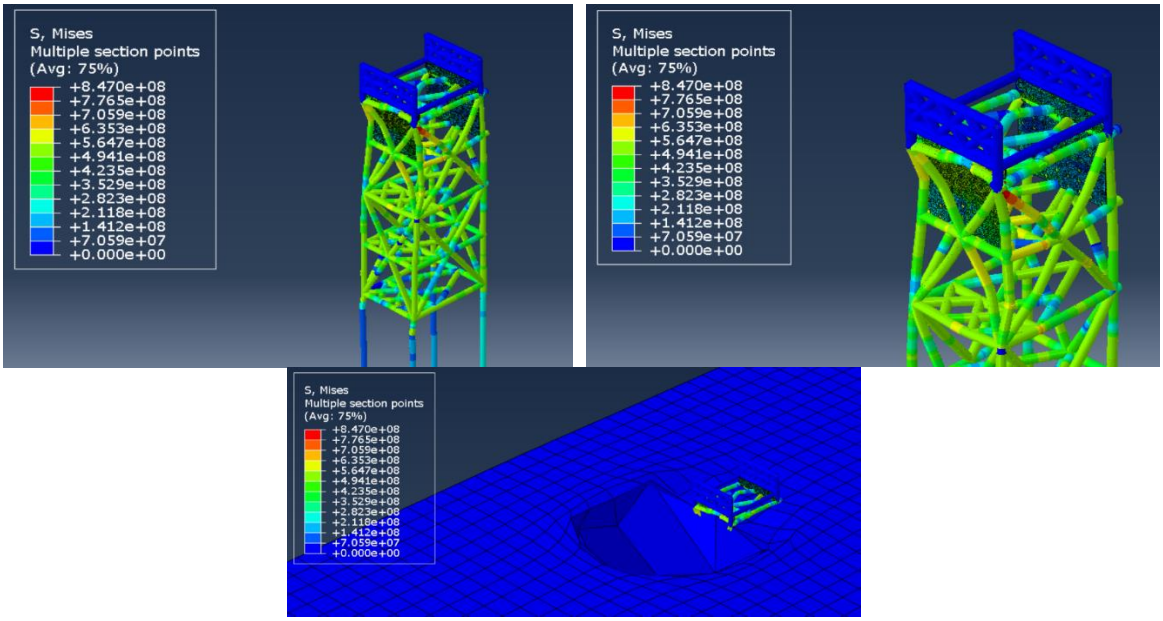


Figure 23. Strengthened offshore structure Case 3 with 2 ton loading and 20 m distance

Figure 23 shows the offshore structure deformation for case 4 that subject to 2 ton blasting at 20 m and strengthening with four parallel steel plates near to the structural edges. Figure 23 shows increment in the structural deformation after placing the four steel plates comparison with figure 22 due to increasing the structural resistance against the blast load that happened when increasing the surface area of that effected by blasting load and that compatible with [53].

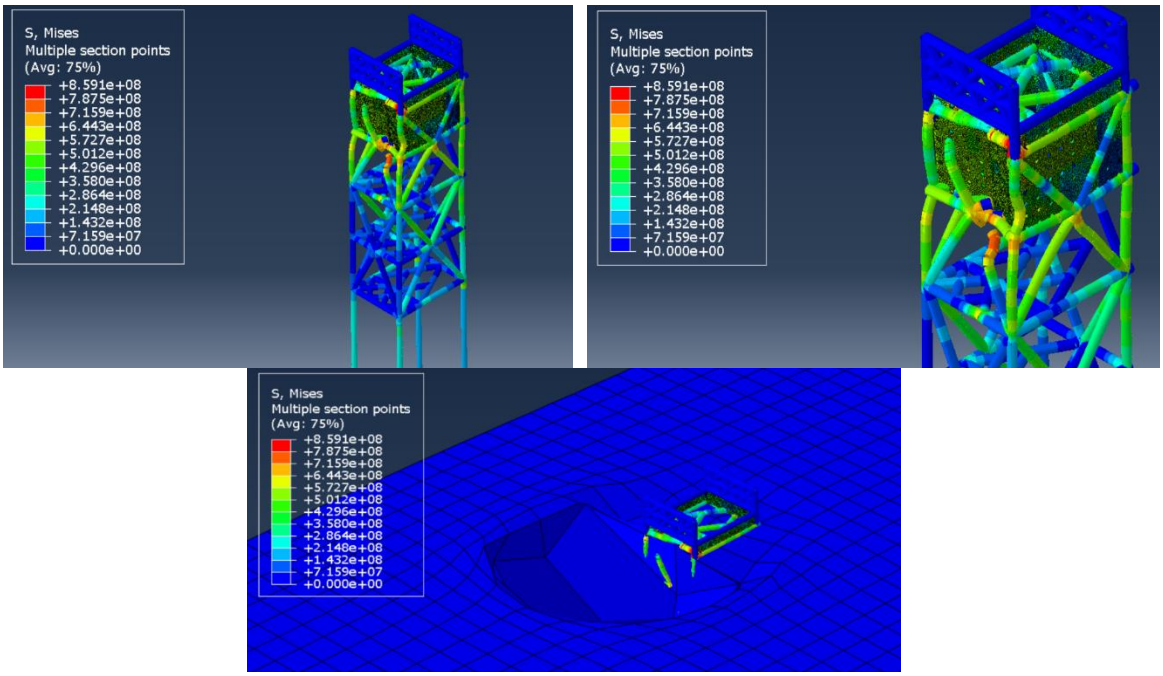


Figure 24. Strengthened offshore structure Case 4 with 2 ton loading and 20 m distance

4. Conclusion

The study concludes that the presence of water significantly amplifies structural displacement under blasting loads, with a threefold increase in displacement compared to air for a 10-ton load. Increasing the distance between the structure and the blast source reduces displacement in air but causes the opposite effect in water. Similarly, deformation increases with distance in air, while decreasing in water. Strengthening techniques generally enhance structural resistance, except for the use of steel plates, which increases the exposed surface, leading to higher displacement and deformation. These findings highlight the complex interactions between blasting loads, environmental conditions, and structural reinforcement:

- Applying 10 tons of blasting load in water leads to 3 times structure displacement when applying similar load at air.
- Increasing the distance between the offshore structure and the source of blasting leads to reduced structure displacement in absence of water, while lead to increase the structure displacement in presence of water.
- Increasing the distance between the offshore structure and the source of blasting leads to increased structure deformation in absence of water, while leads to reduce structure deformation in presence of water.
- Applying different strengthening cases lead to increase the structure resistance against blasting load incases 1, 2, 3, while using steel plate around the structure lead to increase the structural surface that exposure to blasting and then increasing the structural displacement and deformation.

For future work, it is recommended to investigate the response of different materials under similar blasting conditions, analyze the dynamic response of structures to repeated blasts, and examine the impact of water depth on displacement and deformation. Further research should focus on optimizing strengthening techniques to enhance structural resistance and evaluating the long-term effects of blasting loads, such as fatigue and material degradation.

References

1. Z. S. A.-K. Dr. Abdullah Jabar Hussain, “The Fields of Applying the Recycled and Used Oils by the Internal Combustion Engines for Purposes of Protecting the Environment against Pollutions,” J. Adv. Res. Dyn. Control Syst., vol. 12, no. 01-Special Issue, pp. 666–670, 2020, doi: DOI: 10.5373/JARDCS/V12SP1/20201119.
2. J. Hussain and Z. S. Al-Khafaji, “Reduction of environmental pollution and improving the (Mechanical, physical and chemical characteristics) of contaminated clay soil by using of recycled oil,” J. Adv. Res. Dyn. Control Syst., vol. 12, no. 4 Special Issue, pp. 1276–1286, 2020, doi: 10.5373/JARDCS/V12SP4/20201604.
3. Furlan and C. Mortarino, “Forecasting the impact of renewable energies in competition with non-renewable sources,” Renew. Sustain. Energy Rev., vol. 81, pp. 1879–1886, 2018.
4. R. M. Elavarasan, “The motivation for renewable energy and its comparison with other energy sources: A review,” Eur. J. Sustain. Dev. Res., vol. 3, no. 1, p. em0076, 2019.
5. A. L. I. SHUBBAR, Z. Al-khafaji, M. Nasr, and M. Falah, “Using non-destructive tests for evaluating flyover footbridge: case study,” Knowledge-Based Eng. Sci., vol. 1, no. 01, pp. 23–39, 2020.

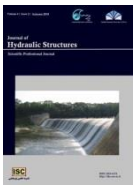
6. C. V. Amaechi, A. Reda, H. O. Butler, I. A. Ja'e, and C. An, "Review on fixed and floating offshore structures. Part I: Types of platforms with some applications," J. Mar. Sci. Eng., vol. 10, no. 8, p. 1074, 2022.
7. H. Baardsen, "A concept study on offshore floating hydrogen production, storage, and offloading." The University of Bergen, 2022.
8. Zhang, G. Gholipour, and A. A. Mousavi, "Blast loads induced responses of RC structural members: State-of-the-art review," Compos. Part B Eng., vol. 195, p. 108066, 2020.
9. K. Cragin, S. A. Daly, S. S. Everingham, J. Hoube, M. R. Kilburn, and C. Y. Marcum, The dynamic terrorist threat: An assessment of group motivations and capabilities in a changing world. Rand Corporation, 2004.
10. J. Revill, Improvised explosive devices: The paradigmatic weapon of new wars. Springer, 2016.
11. Kyei and A. Braimah, "Effects of transverse reinforcement spacing on the response of reinforced concrete columns subjected to blast loading," Eng. Struct., vol. 142, pp. 148–164, 2017.
12. M. E. O'Hanlon, "Forecasting change in military technology, 2020-2040," Mil. Technol., vol. 2020, p. 2040, 2018.
13. N. Brown and D. L. Borovina, "The trinity high-explosive implosion system: the Foundation for Precision Explosive Applications," Nucl. Technol., vol. 207, no. sup1, pp. S204–S221, 2021.
14. G. Liu and H. Li, Offshore platform integration and floatover technology. Springer, 2017.
15. W. Smith, Communication structures. Thomas Telford, 2007.
16. R. S. Nair, "Progressive collapse basics," Mod. steel Constr., vol. 44, no. 3, pp. 37–44, 2004.
17. H. Hao, Y. Hao, J. Li, and W. Chen, "Review of the current practices in blast-resistant analysis and design of concrete structures," Adv. Struct. Eng., vol. 19, no. 8, pp. 1193–1223, 2016.
18. Z. Koccaz, F. Sutcu, and N. Torunbalci, "Architectural and structural design for blast resistant buildings," in The 14th world conference on earthquake engineering, 2008.
19. M. S. Ayob, A. E. Kajuputra, K. Mukherjee, and B. S. Wong, "Global ultimate strength assessment of existing offshore jacket structures," in Offshore Technology Conference Asia, OTC, 2014, p. OTC-24938.
20. Z. NIZAMANI, "Environmental load factors and system strength evaluation of jacket platforms in offshore Malaysia." Universiti Teknologi PETRONAS, 2013.
21. M. A. El-Reedy, Marine structural design calculations. Butterworth-Heinemann, 2014.
22. M. Zarrin, B. Asgarian, and R. Fulad, "A review on factors affecting seismic pile response analysis: a parametric study," Numer. Methods Civ. Eng., vol. 2, no. 2, pp. 35–51, 2017.
23. J. A. Pratt, T. Priest, and C. J. Castaneda, Offshore pioneers: Brown & Root and the history of offshore oil and gas. Elsevier, 1997.
24. M. G. Stewart, M. D. Netherton, and D. V Rosowsky, "Terrorism risks and blast damage to built infrastructure," Nat. Hazards Rev., vol. 7, no. 3, pp. 114–122, 2006.

25. G. Mays and P. D. Smith, Blast effects on buildings: Design of buildings to optimize resistance to blast loading. Thomas Telford, 1995.
26. G. J. McKenzie, "Design Criteria for Blast Loadings in the Australian Environment With Special Reference to Controlled and Uncontrolled Implosions." Western Sydney University (Australia), 2018.
27. A. Neuberger, S. Peles, and D. Rittel, "Scaling the response of circular plates subjected to large and close-range spherical explosions. Part I: Air-blast loading," Int. J. Impact Eng., vol. 34, no. 5, pp. 859–873, 2007.
28. A. Neuberger, S. Peles, and D. Rittel, "Scaling the response of circular plates subjected to large and close-range spherical explosions. Part II: Buried charges," Int. J. Impact Eng., vol. 34, no. 5, pp. 874–882, 2007.
29. S. A. Tekalur, A. Shukla, and K. Shivakumar, "Blast resistance of polyurea based layered composite materials," Compos. Struct., vol. 84, no. 3, pp. 271–281, 2008.
30. S. A. Tekalur, K. Shivakumar, and A. Shukla, "Mechanical behavior and damage evolution in E-glass vinyl ester and carbon composites subjected to static and blast loads," Compos. Part B Eng., vol. 39, no. 1, pp. 57–65, 2008.
31. S. A. Tekalur, A. E. Bogdanovich, and A. Shukla, "Shock loading response of sandwich panels with 3-D woven E-glass composite skins and stitched foam core," Compos. Sci. Technol., vol. 69, no. 6, pp. 736–753, 2009.
32. M. S. Hoo Fatt and L. Palla, "Analytical modeling of composite sandwich panels under blast loads," J. Sandw. Struct. Mater., vol. 11, no. 4, pp. 357–380, 2009.
33. S. Defranco, P. O'Connor, F. Puskar, J. R. Bucknell, and K. A. Digre, "API RP 2SIM: Recommended practice for structural integrity management of fixed offshore platforms," in Offshore Technology Conference, OTC, 2010, p. OTC-20675.
34. G. Abaqus, "Abaqus 6.11," Dassault Syst. Simulia Corp. Provid. RI, USA, 2011.
35. H. Sharifian, K. Bargi, and M. Zarrin, "Ultimate strength of fixed offshore platforms subjected to near-fault earthquake ground vibration," Shock Vib., vol. 2015, pp. 1–19, 2015.
36. A. A. Golafshani, V. Bagheri, H. Ebrahimian, and T. Holmas, "Incremental wave analysis and its application to performance-based assessment of jacket platforms," J. Constr. Steel Res., vol. 67, no. 10, pp. 1649–1657, 2011.
37. M. Abyani, B. Asgarian, and M. Zarrin, "Statistical assessment of seismic fragility curves for steel jacket platforms considering global dynamic instability," Ships Offshore Struct., vol. 13, no. 4, pp. 366–374, 2018.
38. T. Elsayed, M. El-Shaib, and K. Gbr, "Reliability of fixed offshore jacket platform against earthquake collapse," Ships Offshore Struct., vol. 11, no. 2, pp. 167–181, 2016.
39. R. H. Cole, Underwater explosions. Princeton Univ. Press, 1948.
40. Y. Jen, "Coupled acoustic–structural response of optimized ring-stiffened hull for scaled down submerged vehicle subject to underwater explosion," Theor. Appl. Fract. Mech., vol. 52, no. 2, pp. 96–110, 2009.

41. A. M. Zhang, X. L. Yao, and J. Li, “The interaction of an underwater explosion bubble and an elastic–plastic structure,” Appl. Ocean Res., vol. 30, no. 3, pp. 159–171, 2008.
42. Y. S. Shin, “Ship shock modeling and simulation for far-field underwater explosion,” Comput. Struct., vol. 82, no. 23–26, pp. 2211–2219, 2004.
43. A. Forghani et al., “Modelling of damage development in blast loaded composite panels,” in the 16th International Conference on Composite Materials, Kyoto, 2007, pp. 1–8.
44. R. Kalavalapally, R. Penmetsa, and R. Grandhi, “Multidisciplinary optimization of a lightweight torpedo structure subjected to an underwater explosion,” Finite Elem. Anal. Des., vol. 43, no. 2, pp. 103–111, 2006.
45. K. Hibbitt and I. Sorensen, “AbaqusTutorial Version 6. 10 Example Problems Manual,” USA2010, 2010.
46. F. Hung, B. J. Lin, J. J. Hwang-Fuu, and P. Y. Hsu, “Dynamic response of cylindrical shell structures subjected to underwater explosion,” Ocean Eng., vol. 36, no. 8, pp. 564–577, 2009.
47. Y. S. Shin, “Naval ship shock and design analysis: course notes for underwater shock analysis,” Daejeon, Repub. Korea KAIST, 2009.
48. N. Zhang and Z. Zong, “The effect of rigid-body motions on the whipping response of a ship hull subjected to an underwater bubble,” J. Fluids Struct., vol. 27, no. 8, pp. 1326–1336, 2011.
49. C.-C. Liang and Y.-S. Tai, “Shock responses of a surface ship subjected to noncontact underwater explosions,” Ocean Eng., vol. 33, no. 5–6, pp. 748–772, 2006.
50. H. Jang, D. Handel, Y. Ko, H.-S. Yang, and J. Miedecke, “Effects of water deck on rock blasting performance,” Int. J. Rock Mech. Min. Sci., vol. 112, pp. 77–83, 2018.
51. H. X. Yu and J. Y. R. Liew, “Steel framed structures subjected to the combined effects of blast and fire-Part 1: State-of-the-art review,” Adv. Steel Constr., vol. 1, no. 1, pp. 67–84, 2005.
52. Ainalis, O. Kaufmann, J.-P. Tshibangu, O. Verlinden, and G. Kouroussis, “Modelling the source of blasting for the numerical simulation of blast-induced ground vibrations: a review,” Rock Mech. rock Eng., vol. 50, pp. 171–193, 2017.
53. J.-H. Choi, S.-J. Choi, J.-H. J. Kim, and K.-N. Hong, “Evaluation of blast resistance and failure behavior of prestressed concrete under blast loading,” Constr. Build. Mater., vol. 173, pp. 550–572, 2018.

© 2024 by the authors. Licensee SCU, Ahvaz, Iran. This article is an open access article distributed under the terms and conditions of the Creative Commons Attribution 4.0 International (CC BY 4.0 license) (http://creativecommons.org/licenses/by/4.0/).

Journal of Hydraulic Structures
J. Hydraul. Struct., 2025; 11(2): 87-105
DOI: 10.22055/jhs.2024.47643.1316



OPEN ACCESS

Investigating the vulnerability of underground water to pollution (case study: East and Northeast of Chaharmahal and Bakhtiari province)

Mohammad Sadegh Talebi[1]

Abstract

Groundwater aquifers, as one of the most important and vulnerable water resources, are exposed to pollution in various ways, and the detection and control of pollution in them is more difficult and costly than surface water. Also, due to the persistence of pollution in these sources, the best way to prevent their pollution is to identify polluting sources and vulnerable sources, prepare vulnerability zoning maps and adopt appropriate management policies. Considering the importance of the existing aquifers in the east and northeast of Chaharmahal and Bakhtiari province as a supplier of drinking water and agriculture in Barzagi sector of Shahrekord, Farsan, Borujen and Kiyar cities, this research aims to identify the vulnerable areas of the mentioned aquifers using DRASTIC model was done in GIS environment. Then validation was done using the available data. The results showed that the vulnerable classes were: low pollution 42.71%, very low 33.53%, low to medium 17.83%, no pollution 4.07%, medium to high 1.57% and high 0.29% covers the area.

Keywords: risk assessment; DRASTIC model; special vulnerability; Chaharmahal and Bakhtiari.

Received: 03 August 2024; Accepted: 25 October 2024

1. Introduction

Groundwater is considered as an important source of water resources due to its low pollution potential and high storage capacity compared to surface water. The presence of pollutants caused by human activities on the surface of the earth and the penetration of these pollutants into the aquifer reduces the quality of underground water, for this reason it seems necessary to prevent the pollution of groundwater [1]. One of the appropriate tools that helps effectively in groundwater management is the preparation of maps in which vulnerable or sensitive areas to pollution are identified. In this way, different areas can be compared with each other and have a single criterion for evaluation. There are different methods to determine the vulnerability

[1] Assistant Professor, Department of Geography, Meybod University, Meybod, Iran. Email: talebi@meybod.ac.ir **(Corresponding author)**

potential of the groundwater table, including overlapping methods, mathematical methods, statistical methods and combined methods. The overlapping methods are based on combining the layers obtained from different parameters and have the same working basis. These methods differ in the use of the type and number of parameters, but ultimately lead to recording a numerical index or score for each feature [2]. One of the most practical overlapping methods is the Drastic method, which was provided by the US Environmental Protection Agency to determine the potential of groundwater [3]. In this research, the DRASTIC model is used to evaluate the potential of groundwater pollution in the eastern and northeastern regions of Chaharmahal and Bakhtiari provinces.

Checha Ramhal and Bakhtiari province with an area of 16,532 square kilometers is located in the southwest of the country, in the east and northeast of this province are Shahrekord, Farsan, Kiyar and Borujen counties. The suppliers of drinking water and agriculture in a large part of the province are located in the mentioned cities [4]. In recent years, the increase in population and the consequent increase in water demand, as well as the decrease in the quality and pollution of groundwater due to the development of industry and agriculture, have caused attention to the quality of groundwater resources. One of the appropriate ways to prevent groundwater pollution is to identify vulnerable aquifer areas and manage the exploitation of water resources and land use. Changing the quality of groundwater is a big risk for the development of agriculture, animal husbandry, tourism and economy of the province. Considering the importance and necessity of this matter in this research, the zoning of the vulnerability potential of the aquifers is done using the DRASTIC model in the GIS environment.

The DRASTIC model was first introduced in 1987 by Aller and the US Environmental Protection Agency developed it in 1990 to be used as a standard system for assessing groundwater contamination potential [5]. DRASTIC model is one of the most practical overlapping methods. The term DRASTIC stands for parameters that control groundwater pollution in the hydrogeological system. These parameters include: groundwater depth (D), recharge (R), aquifer constituents (A), soil type (S), topography (T), effect of unsaturated zone (I) and hydraulic conductivity of the aquifer (C). Groundwater determines the depth that the pollutant must travel to reach the water table and is very important [6]. Net nutrition is a very important factor for the penetration and transfer of pollutants from the unsaturated zone to the saturated zone, and it takes solid and liquid pollutants to the groundwater level and can also increase the water level [7]. The aquifer environment includes empty spaces and fractures that hold and pass water, so the ingredients of the aquifer affect the flow inside it [8]. The soil environment is called the weathered part above the unsaturated zone. This part is very important in terms of biological activities and the presence of organic substances, and it has a high power to remove and reduce the concentration of pollutants [9]. Topography refers to the changes in the slope of the land, which controls the pollutant movement and its retention on the land surface [10]. The unsaturated environment includes the part located between the water table and the soil environment, which is essentially unsaturated or discontinuously saturated [11]. Hydraulic conductivity shows the ability of aquifer materials to transport water. The movement and diffusion of water and pollutants in the aquifer is controlled by hydraulic guidance [12]. The DRASTIC model is based on the following four assumptions that should be considered for choosing the study area. 1- Contamination enters the groundwater from the surface of the earth. 2- The pollution is washed away by rain and enters the underground water. 3- Transfer of pollution through water and at a similar speed. 4- The area studied under the DRASTIC system must have an area of more than 40 hectares [13]. Finally, after collecting and digitizing the hydrogeological information, the seven mentioned factors that control the pollution potential.

They are overlapped and combined to prepare a vulnerability map, and a new layer named DRASTIC index is obtained.

In recent years, the evaluation of groundwater has been done by researchers in the world and in Iran with several methods, which shows the importance of this issue, which is mentioned in some studies. Siganga et al. (2023) in a study entitled the assessment of groundwater vulnerability in a region in Kenya using the drastic method concluded that Maraka region and Muchi town are more vulnerable than the rest of the studied regions [14]. Ansari and Jabbari (2023) in the article assessing the vulnerability of the aquifer in a semi-arid region of Iran (Izadkhash Fars Plain) announced that almost 50% of the plains were in the high vulnerability class and 28% were in the very high vulnerability class. Places with high vulnerability to pollutants and polluted water were observed in the east and center of the plain. The influence of the formations in the east of the basin can be seen because the amount of sulfate has increased sharply at the outlet of the rivers in the east of the basin, which indicates the presence of evaporite formations with chalk. In the center of the basin, the heavy texture of the soil, low slope and more accumulation of water entering the basin, some of which have a lot of salts, have increased the vulnerability of this part. Another result of this study is that the DRASTIC model is highly effective in evaluating vulnerabilities similar to this research [15]. Among the reasons for the differentiation and innovative aspects of this research compared to similar cases, we can mention: the vast extent of the study area (four major cities of the province including: Shahrekord, Borujen, Farsan and Kiyar) mentioned. On the other hand, nitrate and groundwater quality index have been used to validate the drastic model. To calculate the groundwater quality index, the standards of the Iranian Institute of Standards and Industrial Research and the standards of the World Health Organization have been considered.

2. Materials and ways

2.1. The study area

Chaharmahal and Bakhtiari province with an area of 16533 square kilometers and an average height of 2668 meters in the range between 31 degrees 14 minutes to 33 degrees 47 minutes North latitude and 49 degrees 49 minutes to 51 degrees 34 minutes East longitude in the southwest of the Iranian plateau and the central part Zagros mountain range is located. Figure 1 shows the location of Chaharmahal and Bakhtiari province. Shahrekord, Farsan, Kiyar and Borujen cities are located in the east and northeast of this province [16]. The aquifers of Shahrekord, Farsan, Kiar, Shalamzar, Sefidasht, Boruj and Gandaman-Beldaji, which supply drinking and agricultural water to a large part of the province, are located in the mentioned cities.

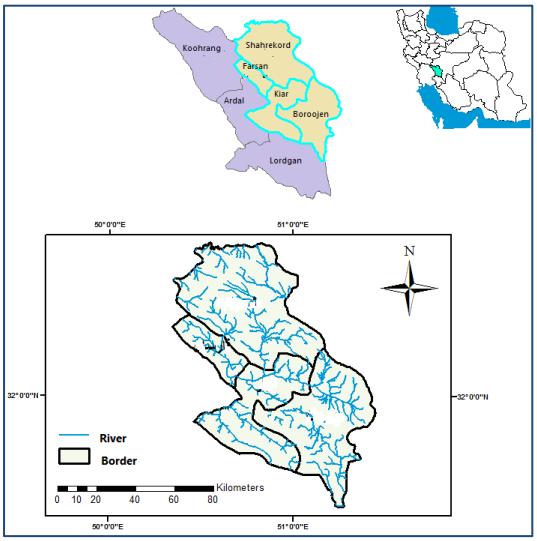


Figure 1. Location of the study area

2.2. Data collection and preparation

The present research is descriptive and analytical in terms of type and practical in terms of purpose. This research was carried out through the steps of: collecting the required data and information and preparing standard maps, assessing the vulnerability potential of Alogi using the DRASTIC model and validating the DRASTIC model. For this purpose, the available statistics and information were entered into the GIS database. From various information sources, including topographic maps with a scale of 1/50000 and land use and geological maps with a scale of 1/100000 of the National Geological Organization, soil map, meteorological statistics, hydrology, groundwater level, results of pumping tests, drilling logs Observational, exploration and exploitation wells, maps of geophysical studies and statistics of water resources were used. These data were obtained from organizations such as Iran Resources Management Company, Provincial Regional Water Company, Provincial Agricultural Jihad Organization and Soil and Water Research Institute. Map information (such as topographic and geological maps) after being digitized and tabular information such as groundwaterlevel, was converted into information bank format and entered into the database, and ArcGIS 10.5 software was used to prepare the required layers. In order to evaluate the vulnerability of groundwater pollution, 7 layers of information including groundwater depth, net nutrition, aquifer environment, soil environment, slope, unsaturated environment and hydraulic conductivity of the aquifer were used. In order to prepare the depth layer to the water level, the statistics and information of 150 piezometric wells in the area were used. To prepare the slope map, a digital topographic map of the area with a scale of 1/100,000 along with auxiliary elevation points related to observation wells was used. The obtained topographic map was converted into a raster and then the slope value was calculated for each cell. Piscopo (2001) method was used to prepare the feeding layer. Piscopo replaced the nutrient potential of an area based on the amount of rainfall, topography and permeability of the area, replacing the method provided by the United States Environmental Protection Agency. To calculate the amount of nutrition, the slope is extracted from the digital elevation model of the area and using the criteria in table (1) was classified.

Table 1. The method of rating the effective slope factor in net feeding [17]

Parameter	Slope%
4	<2
3	2-10
2	10-33
1	33<

Permeability map was also prepared and classified according to the soil hydrology group of the region and according to the criteria defined in table (2) and table (3).

Table 2. minimum infiltration intensity in soil hydrological groups [18]

Soil Hydrological groups	Soil Type	Penetration Rate
A	Sand and gravel	High
B	loamy sand-clay	Medium
C	sand	
D	Lumi	low
	Clay, saline soils, stone	very low

Table 3. Method of rating effective soil permeability factor in pure nutrition [19]

Parameter	Permeability
5	High
4	Medium -
3	High
2	Medium
1	low
	very low

Then, using the data obtained from meteorology, the precipitation map of the studied area was prepared and classified according to table (4).

Table 4. Method of rating effective precipitation factor in net feeding [20]

Parameter	Rainfall(mm)
4	850<
3	700-850
2	500-700
1	<500

After preparing the mentioned maps, in order to obtain net nutrition, all three maps of slope, infiltration and rainfall of the area were overlapped and net nutrition was obtained from equation (1).

Relationship (1) amount of nutrition = % slope + amount of rainfall (mm) + amount of permeability (mm) And finally, the nutrition map was ranked using table (5).

Table 5. Net nutrition ranking method [21]

Rank	Range
10	11-13
8	9-11
5	7-9
3	5-7
1	3-5

The aquifer environment and its ingredients determine the length and trend of the groundwaterflow system in the aquifer. The coarser the materials are, due to the higher permeability of these materials, the vulnerability potential of the aquifer will be higher [22]. To prepare the aquifer layer, the logs of observation and exploitation wells in the region were used. First, the geology map was introduced to the ArcGIS environment and the Eliminate command was performed to remove small areas, then according to the type of log wells (from the reservoir level to the bedrock) or the numerical value based on table (6) was entered in the field created in the geology map. and after that the Dissolve command was executed to unify the common codes, and finally, with the polygon to raster command, the vector map was converted to raster and the final map of the aquifer environment was obtained.

Table 6. ranges and ratings related to the aquifer environment [23]

Range	Rank
Massive shale	2
Igneous/metamorphic	3
Igneous / weathered	4
metamorphism	5
Frosts	6
Layered sandstone,	6
limestone	6
Massive sandstone	8
Massive limestone	9
basalt	10
Limestone	

The soil environment means the upper part of the unsaturated zone, which continues until the penetration of plant roots or the activity of organic organisms. The potential of soil pollution depends on soil characteristics such as soil texture, permeability, and soil organic matter percentage [24]. The soil map of the area was produced according to the land use map and using the existing soil maps of the area in the GIS environment, and the soil environment layer was produced and stored as a raster layer and classified using table (7).

Table 7. Ranges and rankings of soil texture type [25]

soil pattern	Rank
Narc or	10
lack of soil	10
layer	9
Sand	8
sand	7
plant	6
fertilizer	5
dense clay	4
Sandy loam	3
loam	2
Silty loam	1
clayey	
loam	
Fertilizer	
loose clay	

Milder slopes provide the opportunity and possibility of more contamination penetration along with rainfall and in this way, create more pollution potential. Therefore, in the DRASTIC model, areas with a lower slope are ranked higher. The important role of topography can be mentioned in the development and evolution of soil. So that in steep slopes compared to gentler slopes, the thickness of the surface soil layer is less. Therefore, topography by affecting the soil development also affects the pollution potential [26]. In order to prepare the slope layer, using the digital elevation model map of the region in the ArcGIS environment, in the Spatial Analyst section, using the slope determination tool, this layer was prepared and classified and weighted according to the standards and criteria defined in table (8).

Table 8. Slope ranges and ratings [27]

Slope %	Rank
0-2	10
2-6	9
6-12	5
12-18	3
18<	1

The unsaturated environment refers to the lower part of the topsoil up to the water table. The unsaturated environment layer, similar to the soil layer, affects the pollution potential, and the extent of its effects is a function of the permeability and characteristics of the environment of the unsaturated zone. In the unsaturated part, the type of the unsaturated zone and the ability to absorb and retain pollutants and the texture of the geological materials present in it are taken into consideration. Fine particles in clay have greater absorption and retention power than coarse particles and prevent the movement of pollutants into the waters. It is underground and reduces the potential of aquifer pollution. To prepare this layer, exploratory and observational well logs were used, and a similar method was used to prepare the aquifer environment layer, with the difference that for the unsaturated environment layer, the thickness and material of the layers of the unsaturated zone in the well logs have been considered. To prepare the mentioned layer, first introduce the geology map to the ArcGIS environment and execute the Eleminate command to remove small areas, then, according to the type of well logs, enter a numerical value based on

table (9) in the field created in the geology map and the Dissolve command to merge The common codes are executed and finally, with the polygon to raster command, the vector map is converted to a raster and the final map of the unsaturated environment is produced and multiplied by five (layer weight) in the raster calculator part of the ArcGIS environment. The high weight of this layer is because the area Unsaturated by retaining, absorbing and removing pathogenic viruses and bacteria, absorbing and reducing many synthetic organic chemicals, diluting the concentration of heavy metals and other inorganic chemicals through absorption and reaction with the surface of minerals in the unsaturated zone and through Plants and agricultural products play a key role in protecting groundwater.

Table 9. ranges and ratings of the unsaturated environment [28]

Range	Rank
Locking layer	1
silt/clay	3
shale	3
Limestone	6
Sandstone	6
Limestone and Layered	6
shales	6
	4
Sand with a large amount	8
of silt clay	9
Igneous/metamorphic	10
Sand	
basalt	
Karst limestone loose clay	

The hydraulic conductivity of an aquifer shows the mobility capacity of groundwaterin a saturated environment, therefore, the potential for the mobility of polluting substances by groundwateris almost equal to the hydraulic conductivity of the aquifer [29]. The amount of hydraulic conductivity controls the pollutant's movement and spread from the point of infiltration until it reaches the saturated zone. For this reason, areas with high hydraulic conductivity create more pollution potential. The information related to hydraulic conductivity is obtained from the calculations of the pumping test of the existing wells in the study area. Considering that in the pumping tests, the value of the transferability coefficient parameter is measured, the information and geographical location related to the transferability coefficient and saturation thickness The aquifer of the studied area was obtained from the reports prepared by the water district administration. Then, the transferability coefficient map was obtained on the aquifer thickness map according to equation (2) and the hydraulic conductivity map of the area was obtained and it was classified according to the criteria defined in table (10).

Equation (2) T=Kb In this relation, K is the hydraulic conductivity in terms of (m/D), b is the thickness of the aquifer in terms of (m) and T is the transfer coefficient in terms of (m^2/D).

Table 10. ranges and ratings of hydraulic conductivity [30]

Range(m/Day)	Rank
0.04-4.1	1
4.1-12.3	2
12.3-28.7	4
28.7-41	6
41-82	8
82<	10

Finally, after collecting and digitizing the hydrogeological information, the seven mentioned factors that control the pollution potential. They were overlapped and combined to prepare the inherent vulnerability and a new layer named DRASTIC index was obtained. Therefore, the inherent vulnerability index in this method was obtained by multiplying the weight of each parameter by its rank [31]. The classification and valuation of the classes related to each of the parameters was done based on the DRASTIC standard method in the GIS environment in the Raster calculator section. A larger DRASTIC index indicates a greater sensitivity of the area to pollution, and a smaller number indicates a lower sensitivity. Finally, by ranking the DRASTIC index based on table (11), the vulnerability map of the region was prepared.

Table 11. ranking of DRASTIC vulnerability index [32]

Index value	Vulnerability class
<79	No risk of
80-99	contamination
100-119	very little
120-139	Low
139-159	low to medium
160-179	Moderate to high
180-199	Much
199 <	very much
	Quite susceptible

3. Discussion and results

The precipitation map of the studied area is shown in figure (2), the elevation map is in figure (3), the geological map is in figure (4) and the land use map is shown in figure (5).

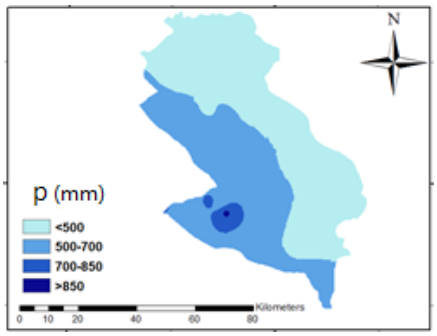


Figure 2. map of precipitation of the studied area

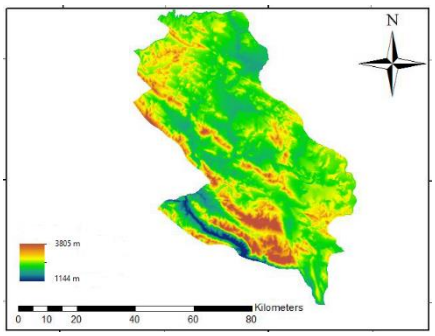


Figure 3. Elevation map of the studied area

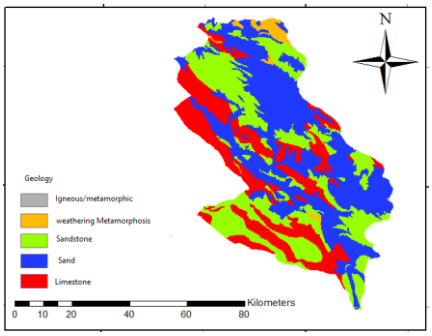


Figure 4. geological map of the studied area

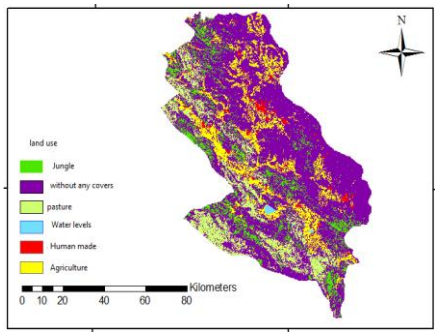


Figure 5. land use map of the studied area

In the studied area, the depth to the water table varies from 0.88 to 80.5 meters above the ground. The groundwaterdepth map is shown in Figure (6). The largest area of the studied area is related to the depths between 4.5 and 9 meters, which covers 24.82% of this area and in terms of vulnerability, it has assigned a value of 7. which has high ranks for vulnerability, and it can be said that the ability of the studied area in terms of the depth of the water table to be polluted was high. In fact, the depth of groundwaterhas an opposite relationship with the level of vulnerability. The more the depth of the groundwaterdecreases, the greater the vulnerability.

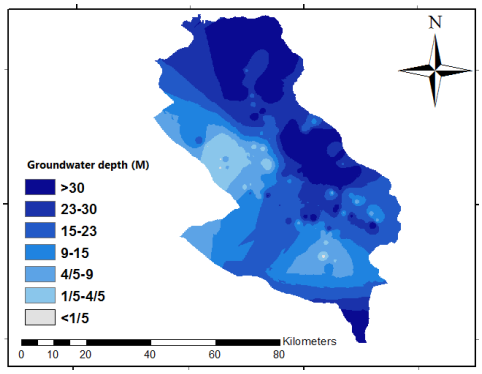


Figure 6. ranking the depth of the area in terms of pollution potential

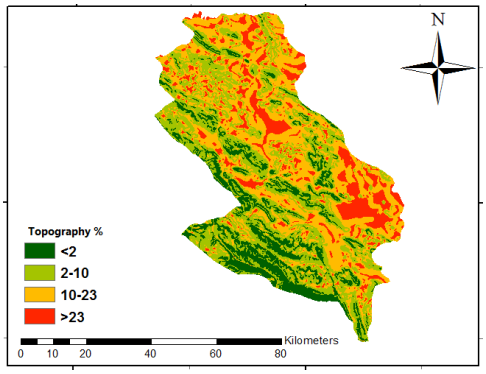


Figure 7. ranking of the slope map of the studied area

The slope map is classified according to table (1) and shown in figure (7).

Figure (8) shows the precipitation map of the study area. About 58% of the area has less than 500 mm of rainfall, and in the southwestern regions there are areas with more than 850 mm of rainfall. The higher the amount of precipitation, the higher the amount of nutrition, and this increases the vulnerability of the region to pollution.

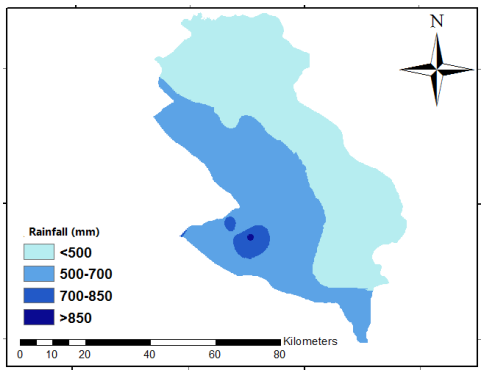


Figure 8. Rainfall ranking of the study area

Figure (9) shows the ranking of soil permeability of the study area. The lower the permeability, the less prone to contamination.

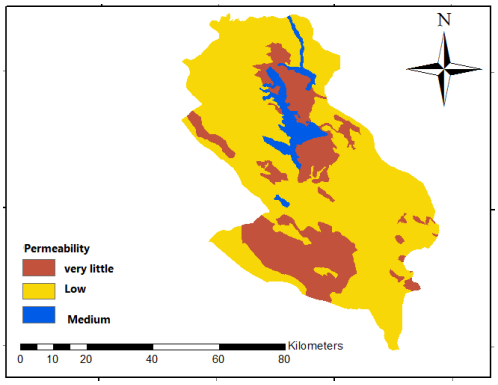


Figure 9. soil permeability ranking of the study area in terms of pollution potential

Figure (10) shows the map of net nutrition. Nutrition and vulnerability are directly related. As the amount of nutrition increases, the vulnerability also increases.

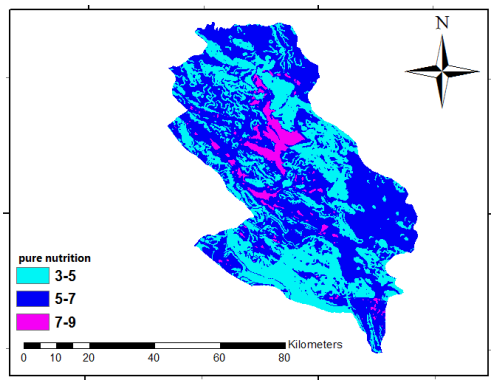


Figure 10. ranking of net nutrition of the study area

Figure (11) shows the zoning of the aquifer environment. According to the figure, up to 41.5% of the area of the area is related to sand and after that, sandstone covers up to 31% of the area.

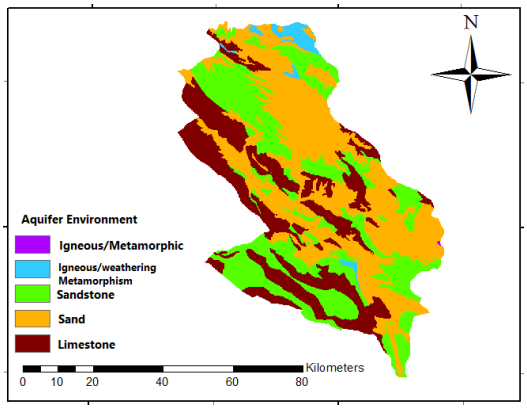


Figure 11. ranking of the aquifer environment of the study area in terms of pollution potential

Figure (12) shows the soil map of the region, according to which more than 50.8% of the area is related to loamy textures, 22.7% is non-dense clay and about 17.5% is clayey loam and according to table (7) respectively They have ranks 5, 1 and 3, and these tissues have low to medium ranks in terms of vulnerability. The texture of sand and gravel has a greater ability to transfer pollutants from the surface of the earth to the underground aquifers, which is small in the studied area.

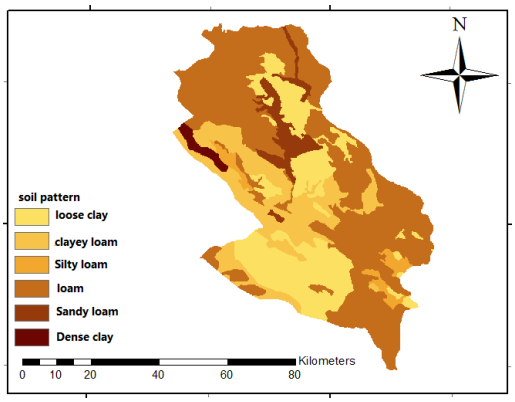


Figure 12. ranking of the soil texture of the study area in terms of pollution potential

Figure (13) shows the slope map. According to the figure, the largest extent is related to the slope of 0-2%, which according to table (8) is given the 10th rank in terms of vulnerability. In fact, slope and vulnerability have the opposite relationship. The lower the slope, the higher the vulnerability.

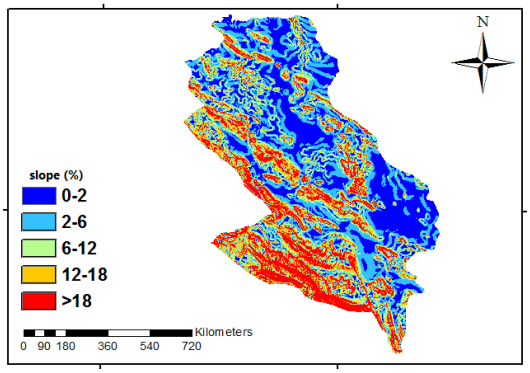


Figure 13. ranking of the slope of the study area in terms of pollution potential

Figure (14) shows the map of the effect of the unsaturated zone. According to the figure, the largest area with 51.3% is related to silt and clay and the smallest area is igneous and metamorphic with 2.54% of the area.

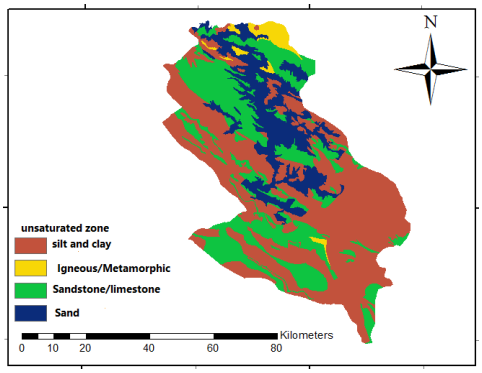


Figure 14. ranking the effect of the unsaturated zone of the study area in terms of pollution potential

The zoning map of hydraulic conductivity is presented in figure (15). According to the figure, about 83.6% of the area under study corresponds to rank 2 (12.3-4.1 meters per day). Hydraulic conductivity and the degree of vulnerability have a direct relationship. Vulnerability increases with the increase of hydraulic conductivity.

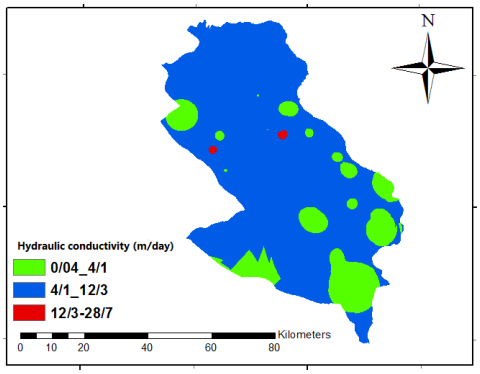


Figure 15. hydraulic conductivity rating of the studied area in terms of pollution potential

In Figure (16), the zoning map of inherent vulnerability is shown using the combination of seven drastic parameters, which classified the studied area into 6 categories: no pollution, very low, low, low to medium, medium to high, and high. These points should be taken into account when combining layers: a. All the created layers should be raster. b. Pixel size should be the same in all layers. J. All layers should be prepared in a similar coordinate system. According to table (12), the low vulnerability class has the largest area and the high vulnerability class has the least area. The three categories of low to medium vulnerability, medium to high and high pollution are mostly concentrated in the western areas of the study area. This indicates that there is more potential for vulnerability in the western areas and should be prioritized in pollution management planning. Take

Table 12. vulnerability classification of Drastic model and the area of each floor

Vulnerability class	Range of floors	area (km^2)	area (%)
No pollution	<79	296.11	4.07
very little	80-99	2437.56	33.53
Low	100-119	3104.86	42.71
low to	119-139	1296.53	17.83
medium	139-159	113.52	1.57
Moderate to high	160-179	21.05	0.29
Much			

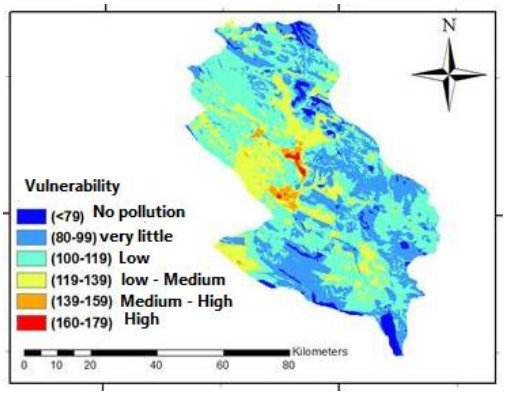


Figure 16. Inherent vulnerability zoning map using the combination of seven parameters

3.1. Validation of DRASTIC model using nitrate and GQI

Figure (17) shows the location of the wells where the nitrate parameter was measured on the DRASTIC pollution potential map. Figures (18) and (19) respectively show the location of the wells that the GQI obtained based on the standards of the Iranian Institute of Standards and Industrial Research and based on the standards of the World Health Organization. The final index calculated for the quality parameter of groundwaterin the region The studied item is above 80, which is in the good category based on table (13) of the groundwaterquality index.

Table 13. ranking and value range in GQI [33]

Qualitative value of the index	Range
weak	<60
medium	60-80
Good	80<

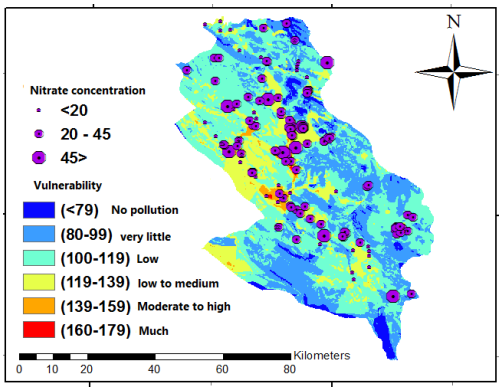


Figure 17. Drastic vulnerability map and nitrate concentration

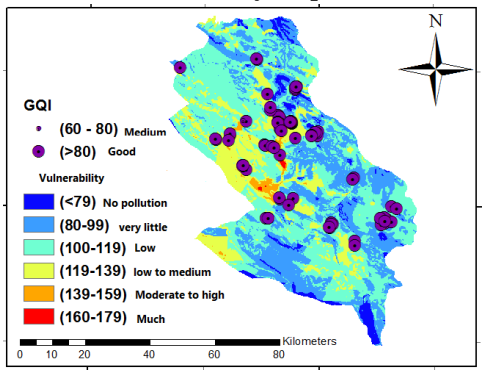


Figure 18. drastic vulnerability map and groundwater quality index based on ISIRI standards

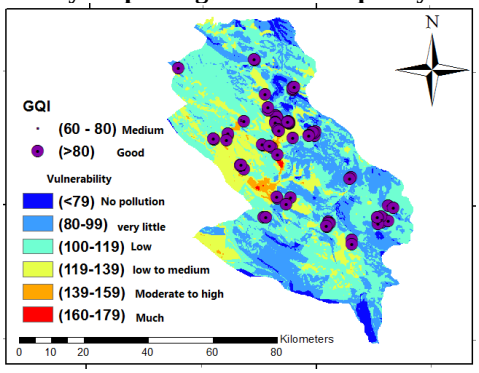


Figure 19. drastic vulnerability map and groundwater quality index based on WHO standards

4. Conclusion

In recent years, the increase in water consumption and the increasing and costly limitations of the development of surface water resources have led to double pressures on the country's underground water resources. Sustainable access to safe drinking water is necessary and

necessary for the well-being and health of human life. Therefore, protection of groundwater quality is an important challenge.

By examining the model used in this aquifer, it can be concluded that the use of more parameters has a great effect on the accuracy of the results. Although this point is not a reason to reject or accept other models; Because many of the models with less parameters can be in the levels and larger scales with fewer parameters provide acceptable results. What comes from the results of this study is that the model Dractic has more acceptable accuracy. The results of the study by Ghanbarian and Ahmadi Nadushan under the title of assessing the vulnerability of the Lordegan Plain aquifer using DRASTIC, AVI, and GODS models confirm this [34]. The current study and its results, because it shows the vulnerability of groundwater to pollution in a complete and visual way, has provided a very valuable tool for officials and managers to make the necessary decisions to improve land use and management of aquifers such as the plain. Adopt management practices in the use of agricultural water and agricultural fertilizers, urban sewage, land use change, etc. According to table (12), the studied area is in the range of no pollution to high pollution in terms of pollution classification. Vulnerable classes in order: low pollution 42.71%, very low 33.53%, low to medium 17.83%, no pollution 4.07%, medium to high 1.57% and high 0.29%. includes In these areas, the natural conditions of the region, such as low slope, precipitation of more than 700 mm, high nutrition, sand and lime in the aquifer environment and high hydraulic conductivity, have created a high potential for increasing the level of vulnerability, which is necessary to prevent pollution. Groundwater, more care and control should be considered. In general, it can be concluded that based on the results of the Drastic model, the western and central regions of the study area have the highest potential of being vulnerable to pollution.

In this research, Drastic model was used to evaluate pollution, but there are other models to evaluate vulnerability. Therefore, it is necessary to try other models to assess the vulnerability so that the model is selected according to the local hydrogeological conditions of the region.

Author contributions

The entire research process was done by myself as the responsible author.

Appreciation

The author is grateful to Chaharmahal and Bakhtiari regional water organization for providing raw data related to the studied aquifers.

Conflict of interest

No financial assistance or fees were received from any person or organization for conducting this research.References

References

1. Ghafari, S. R., & Nasehi, H. (2021) Spatial model of establishment and construction of rural-nomadic tourism complexes in Chaharmahal and Bakhtiari province. Journal of Sustainable Rural Development, 5(1), 83-96. https://dorl.net/dor/20.1001.1.25383876.2021.5.1.7.1
2. Ahmed S, Akhtar N, Rahman A, Mondal NC, Khurshid S, Sarah S, Khan MMA, Kamboj V. (2022) Evaluating groundwater pollution with emphasizing heavy metal hotspots in an

urbanized alluvium watershed of Yamuna River, northern India. Environ Nanotechnol Monit Manag 18:1007442. https://doi.org/10.1016/j.enmm.2022.100744.

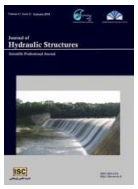
3. Guo X, Xiong H, Li H, Gui X, Hu X, Li Y, Cui H, Qiu Y, Zhang F, Ma C (2023) Designing dynamic groundwater management strategies through a composite groundwater vulnerability model: Integrating human-related parameters into the DRASTIC model using LightGBM regression and SHAP analysis. Environ Res 236:116871. https://doi.org/10.1016/j.envres.2023.116871
4. Ghafari, S. R., & Nasehi, H. (2021) Spatial model of establishment and construction of rural-nomadic tourism complexes in Chaharmahal and Bakhtiari province. Journal of Sustainable Rural Development, 5(1), 83-96. https://dorl.net/dor/20.1001.1.25383876.2021.5.1.7.1
5. Ahmed SI, Cheng CL, Gonzalez J, Kang JJ, Ho J, Soto-Sanchez L (2022) Groundwater vulnerability assessment of shallow aquifer in the South Texas sand sheet using a GIS-based DRASTIC model. Earth Syst Environ 8:4075–4091. https://doi.org/10.1007/s40808-021-01292-4
6. Asomaku SO (2023) Quality assessment of groundwater sourced from nearby abandoned landfills from Industrial City in Nigeria: water pollution indices approach. Hydroresearch 6:130–137. https://doi.org/10.1016/j.hydres.2023.03.002
7. Monatisa L, de Kock LA, Mamba BB, Nkambule TTI, Izady A, Al-Maktoumi A, Msagati TA (2023) Development of the early warning model for oil produced water pollution and compliance with the guidelines using dimensional analysis. J Water Process Eng 53:103870. https://doi.org/10.1016/j.jwpe.2023.103870
8. Chakraborty, M. et al. (2022) 'Assessment of groundwater quality using statistical methods: A case study', Arabian Journal of Geosciences, 15(12), pp. 1136–1136. doi: https://doi.org/10.1007/s12517-022- 10276-2
9. Das, B., Dhorde, A., and Mitra, D. (2022) 'Delineating saltwater intrusion zones and assessing its relation with mangrove species along the coastal tracts of Raigad district of Maharashtra, India', Journal of Coastal Conservation, 26(6), pp. 78-88. doi: https://doi.org/10.1007/s11852-022-00926-8
10. Eftekhari, M., and Akbari, M. (2020) 'Evaluation of the SINTACS-LU model capability in the analysis of aquifer vulnerability potential in semi-arid regions', Journal of Applied Research in Water and Wastewater, 7(2), pp. 111–119. doi: https://doi.org/10.22126/arww.2020.4785.1151
11. Fankhauser, K. et al. (2022) 'Estimating groundwater use and demand in arid Kenya through assimilation of satellite data and in-situ sensors with machine learning toward drought early action', Science of The Total Environment, 831, pp. 154453–154468. doi: https://doi.org/10.1016/j.scitotenv.2022.154453
12. Gwara, S. et al. (2020) 'Why do we know so much and yet so little? a scoping review of willingness to pay for human excreta derived material in agriculture', Sustainability, 12(16), pp.6490–6515. https://doi.org/10.3390/su12166490
13. Amin, H.M. et al. (2021) 'Assessment of wastewater contaminant concentration through the vadose zone in a soil aquifer treatment system', Applied Ecology and Environmental Research, 19(3), pp. 2385–2403. doi: https://doi.org/10.15666/aeer/1903_23852403
14. Siganga, C. A., Ong'or, B. T. I., & Kanda, E. K., (2023) Assessment of groundwater vulnerability in Webuye Municipality, Kenya, Journal of Applied Research in Water and Wastewater, 10 (2), 2023, 103-111. doi: https://doi.org/10.22126/arww.2024.9358.1300

15. Ansari, I., Jabbari, (2023) Evaluation of the vulnerability of groundwaterresources in the Izadkhast plain of Fars province, Journal of Applied Research in Water and Wastewater, 10 (2), 2023, 150-155. doi: https://doi.org/ 10.22126/arww.2023.8858.1285.
16. Ghafari, S. R., & Nasehi, H. (2021) Spatial model of establishment and construction of rural-nomadic tourism complexes in Chaharmahal and Bakhtiari province. Journal of Sustainable Rural Development, 5(1), 83-96. https://dorl.net/dor/20.1001.1.25383876.2021.5.1.7.1
17. Ansari, I., Jabbari, (2023) Evaluation of the vulnerability of groundwaterresources in the Izadkhast plain of Fars province, Journal of Applied Research in Water and Wastewater, 10 (2), 2023, 150-155. doi: https://doi.org/ 10.22126/arww.2023.8858.1285.
18. Kadkhodaie, F., Asghari Moghaddam, A., & Barzegar, R. (2019) Optimizing the DRASTIC vulnerability approach to overcome the subjectivity: a case study from Shabestar plain, Iran. Arab Journal of Geosciences, 12(527). https://doi.org/10.1007/s12517-019-4647-y
19. Kadkhodaie, F., Asghari Moghaddam, A., & Barzegar, R. (2019) Optimizing the DRASTIC vulnerability approach to overcome the subjectivity: a case study from Shabestar plain, Iran. Arab Journal of Geosciences, 12(527). https://doi.org/10.1007/s12517-019-4647-y
20. Kadkhodaie, F., Asghari Moghaddam, A., & Barzegar, R. (2019) Optimizing the DRASTIC vulnerability approach to overcome the subjectivity: a case study from Shabestar plain, Iran. Arab Journal of Geosciences, 12(527). https://doi.org/10.1007/s12517-019-4647-y
21. Kadkhodaie, F., Asghari Moghaddam, A., & Barzegar, R. (2019) Optimizing the DRASTIC vulnerability approach to overcome the subjectivity: a case study from Shabestar plain, Iran. Arab Journal of Geosciences, 12(527). https://doi.org/10.1007/s12517-019-4647-y
22. Khrisat, H. Al-Bakri, J. (2019), Assessment of Groundwater Vulnerability in Azraq Catchment in Fuhais-Jordan Using DRASTIC Model. Open Journal of Geology Vol.9 No.7, https://doi.org/ 10.4236/ojg.2019.97024
23. Ansari, I., Jabbari, (2023) Evaluation of the vulnerability of groundwaterresources in the Izadkhast plain of Fars province, Journal of Applied Research in Water and Wastewater, 10 (2), 2023, 150-155. doi: https://doi.org/ 10.22126/arww.2023.8858.1285.
24. Guo X, Xiong H, Li H, Gui X, Hu X, Li Y, Cui H, Qiu Y, Zhang F, Ma C (2023) Designing dynamic groundwater management strategies through a composite groundwater vulnerability model: Integrating human-related parameters into the DRASTIC model using LightGBM regression and SHAP analysis. Environ Res 236:116871. https://doi.org/10.1016/j.envres.2023.116871
25. Anvari, S., Rezakhani Nejad, M. (2022). 'Vulnerability, Underground Water, DRASTIC Model, GIS, Sirjan Plain.', Irrigation Sciences and Engineering, 45(2), pp. 19-29. https://doi.org/10.22055/JISE.2022.41088.2033
26. Nadjai, S., Khammar, H., Boulabeiz, M., Nabed, A. N., Benaabidate, L. (2024) Sensitivity Analysis and GIS Tools for Groundwater Vulnerability Assessment. (Application in the Middle Chellif Plain, Algeria). Earth Sciences Research Journal, 28(1), 65-72. https://doi.org/10.15446/esrj.v28n1.106588.
27. Siganga, C. A., Ong'or, B. T. I., & Kanda, E. K., (2023) Assessment of groundwater vulnerability in Webuye Municipality, Kenya, Journal of Applied Research in Water and Wastewater, 10 (2), 2023, 103-111. doi: https://doi.org/10.22126/arww.2024.9358.1300
28. Kadkhodaie, F., Asghari Moghaddam, A., & Barzegar, R. (2019) Optimizing the DRASTIC vulnerability approach to overcome the subjectivity: a case study from Shabestar plain, Iran. Arab Journal of Geosciences, 12(527). https://doi.org/10.1007/s12517-019-4647-y

29. Siganga, C. A., Ong'or, B. T. I., & Kanda, E. K., (2023) Assessment of groundwater vulnerability in Webuye Municipality, Kenya, Journal of Applied Research in Water and Wastewater, 10 (2), 2023, 103-111. doi: https://doi.org/10.22126/arww.2024.9358.1300
30. Kadkhodaie, F., Asghari Moghaddam, A., & Barzegar, R. (2019) Optimizing the DRASTIC vulnerability approach to overcome the subjectivity: a case study from Shabestar plain, Iran. Arab Journal of Geosciences, 12(527). https://doi.org/10.1007/s12517-019-4647-y
31. Siganga, C. A., Ong'or, B. T. I., & Kanda, E. K., (2023) Assessment of groundwater vulnerability in Webuye Municipality, Kenya, Journal of Applied Research in Water and Wastewater, 10 (2), 2023, 103-111. doi: https://doi.org/10.22126/arww.2024.9358.1300
32. Kadkhodaie, F., Asghari Moghaddam, A., & Barzegar, R. (2019) Optimizing the DRASTIC vulnerability approach to overcome the subjectivity: a case study from Shabestar plain, Iran. Arab Journal of Geosciences, 12(527). https://doi.org/10.1007/s12517-019-4647-y
33. Kadkhodaie, F., Asghari Moghaddam, A., & Barzegar, R. (2019) Optimizing the DRASTIC vulnerability approach to overcome the subjectivity: a case study from Shabestar plain, Iran. Arab Journal of Geosciences, 12(527). https://doi.org/10.1007/s12517-019-4647-y
34. Ghanbarian M, Ahmadi Nadoushan M. (2019) Determination of AquiferVulnerability in Lordegan Aquifer Using DRASTIC, AVI and GODS Models.Iranian Journal of Research in Environmental Health.;4 (4): 257- 271.

© 2025 by the authors. Licensee SCU, Ahvaz, Iran. This article is an open access article distributed under the terms and conditions of the Creative Commons Attribution 4.0 International (CC BY 4.0 license) (http://creativecommons.org/licenses/by/4.0/).

Journal of Hydraulic Structures
J. Hydraul. Struct., 2025; 11(2): 106-117
DOI: 10.22055/jhs.2024.48222.1327



OPEN ACCESS

Full scale optimization of chlorine injection pattern in Khansar water distribution network using WaterGEMS

Ali Poorkarimi[*1]
Habib Asi[1]
Shahrzad Maleki[1]

Abstract

Chlorine is the most widely used disinfectant in the water treatment process for eliminating pathogenic microorganisms that may be present in the distribution network. Maintaining minimum residual chlorine in water distribution networks is challenged by its decay over time and distance travelled. Chlorine dosage must be optimized by adjusting its injection rates and placement. This study utilized WaterGEMS software to model the water network of Khansar city and analyze its current chlorine levels. It was found that some end-of-line pipes had chlorine concentrations that fell below the standard limits. Through optimization of chlorine dosing at the reservoirs while simultaneously reducing chlorine consumption, approximately 65% of the pipes with non-compliant chlorine levels were brought into compliance. Additionally, 66% of the water volume that previously had insufficient chlorine now meets the standard and is delivered to consumers. It should be noted that these results were obtained at the same time as the amount of chlorine consumed daily decreased from 1130.4 to 656.7.

Keywords: Residual chlorine; Disinfection; Bulk decay; Wall decay; WaterGEMS.

Received: 25 October 2024; Accepted: 29 October 2024

1. Introduction

Water quality in distribution networks must meet both potability and aesthetic standards. Potability implies that the levels of chemical, physical, and microbiological contaminants do not exceed permissible limits, and aesthetic factors, including parameters such as color, odor, taste, and turbidity. Declining water quality in distribution networks poses a serious risk to public health; thus, effective management of these networks is essential for maintaining water quality. Moreover, as a hygienic product, treated water helps prevent many harmful microorganisms' proliferation [1].

Disinfection is considered the minimum treatment for drinking water sources. Among the available disinfectants, chlorine and its derivatives are widely used due to their low cost, ease of

[*] E-mail: poorkarimi@fasau.ac.ir (**Corresponding Author**)
[1] Department of Civil Engineering, Faculty of Engineering, Fasa University, Fasa, Iran.

application, and ability to inactivate microorganisms in drinking water distribution networks. As chlorinated water travels through pipes, it reacts with substances in the water and pipe walls, causing a decrease in chlorine levels in the network [2]. Maintaining residual chlorine within the limits specified by standards in water supply networks ensures the quality and safety of drinking water. However, it is important to note that residual chlorine concentrations are not uniform throughout the network and exhibit fluctuations. In some parts of the network, chlorine levels may exceed permissible limits, leading to off-flavors and odors, and formation of toxic disinfection byproducts. Conversely, residual chlorine levels may fall below permissible limits in other parts of the network, increasing the risk of waterborne disease outbreaks. This phenomenon of chlorine reduction in water distribution networks is called chlorine decay [3].

The amount of chlorine added can be adjusted by controlling the chlorine concentration in reservoir before the water enters the network or in the booster stations through the network. If these locations are not specified correctly, it can result in excessive residual chlorine concentrations in pipes near the injection locations and insufficient residual chlorine concentrations in pipes further away at certain times. Therefore, to effectively manage water quality in distribution networks, it is essential to determine the optimal amount and location of chlorine injection to ensure that concentrations remain within the specified range throughout the network [4]. Optimizing the chlorine injection in water distribution networks has been studied in several research focusing on the locations and/or the scheduling of chlorine dosing stations [5-13]. Various studies examined simulation models such as EPANET for residual chlorine prediction in a network [13-17]. However, WaterGEMS software has only been used in a limited number of studies to determine residual chlorine in water distribution networks [9,18,19].

The aim of this study is to determine the chlorine injection for the water distribution network of Khansar city. This distribution network has 7 independent pressure zones, each fed by one or two reservoirs. To optimize chlorine injection, WaterGEMS software was used for hydraulic and water quality simulation. According to the separation of the distribution network of the whole city into independent zones, the pattern of chlorine injection in the reservoirs was considered. The optimization of the chlorine dose rate was achieved by changing the injection dose rate in the reservoirs so that the chlorine concentration maintains the permissible limits at demand junctions and pipes.

2. Residual Chlorine Concentration

The reduction in residual chlorine concentration within water distribution networks is attributed to two primary mechanisms: bulk decay and wall decay.

In bulk decay, chlorine reacts with mineral and organic molecules present in the water, leading to a decrease in its concentration. This reduction in chlorine concentration within the water network is termed bulk chlorine decay. Over the past few decades, researchers have conducted extensive investigations into bulk chlorine decay. The general reaction form and the differential equation employed in these studies are presented in Equations (1) and (2), respectively [20,21].

$$Cl + A \rightarrow Product \tag{1}$$

$$\frac{dC}{dt} = -k'C^n R^m \tag{2}$$

where k represents the bulk kinetic coefficient, C is the chlorine concentration (mg/L), R is the concentration of chlorine demand substances (mg/L), and m and n are the reaction orders for the chlorine demand substance and chlorine, respectively. Since the concentration of chlorine demand

substances is significantly higher than the concentration of the chlorine, the concentration of chlorine demand substances is assumed to be constant over time. Consequently, the developed Equation (3) is proposed [21].

$$\frac{dC}{dt} = k_b C^n \tag{3}$$

In wall decay, the reaction between chlorine and the inner surface of pipes in distribution and transmission networks leads to a decrease in chlorine concentration. This type of chlorine concentration reduction is termed wall decay. According to Equation (4), there is a direct correlation between the rate of wall decay, the surface-to-volume ratio of the pipe, the mass transfer coefficient, and the chlorine concentration [22]. Many researchers, including Hallum et al., Rossum et al., and Jisberg, emphasize the primary nature of wall decay reactions, and the differential equation for this process is represented as follow [23,24,25].

$$\frac{dC}{dt} = \frac{A}{V} k_w C^n \tag{4}$$

The physical, chemical, and microbiological parameters of water within distribution networks must adhere to the permissible limits outlined in the drinking water quality standard [26]. Consequently, in accordance with the provisions of the 43rd publication of the Technical Regulations and Criteria for the Water Industry in Iran, sequential and regular sampling of the network should be conducted to measure residual chlorine at various points [27].

According to the Iranian drinking water standard, to prevent and control secondary contamination within the water network, a minimum residual chlorine concentration of 0.6 mg/L is required, and based on the US Environmental Protection Agency (USEPA) guidelines, the maximum residual chlorine concentration should not exceed 4 mg/L at any point in the distribution network [28].

This chlorination method significantly increases the likelihood of insufficient standard chlorine concentrations at certain points within the network, especially at the end points. Studies and research have shown that consumers at the end of the network do not receive adequate quality drinking water. Therefore, they are at a higher risk of waterborne contamination. Conversely, excessive chlorine levels in water can also pose problems [29]. The permissible limits for free residual chlorine in drinking water for various water supply systems and sampling locations are presented in Table 1.

Table 1. Permissible limits for free residual chlorine.

Water supply system and harvesting site	Amount of residual free chlorine (mg/L)
Public Water Tap	0.5-1.0
Water Delivery Point	0.2-0.8
Mobile drinking water tankers at the water intake site	1.0-2.0
Mobile drinking water tankers at the delivery point	0.8-1.0

3. Methodology

3.1. Case Study

Khansar city, with an area of 953 km^2, and an altitude of 2215 m above sea level, located in the west of Isfahan province, Iran, was selected as the case study for this research. Figure 1 presents a schematic image of the location of Khansar city. WaterGEMS Connect Edition Update 10 software was employed for hydraulic and water quality simulations of the network. Necessary data, such as water distribution network map of Khansar city, network specification, and water demand and consumption pattern, were obtained from the Isfahan Water and Wastewater Company.

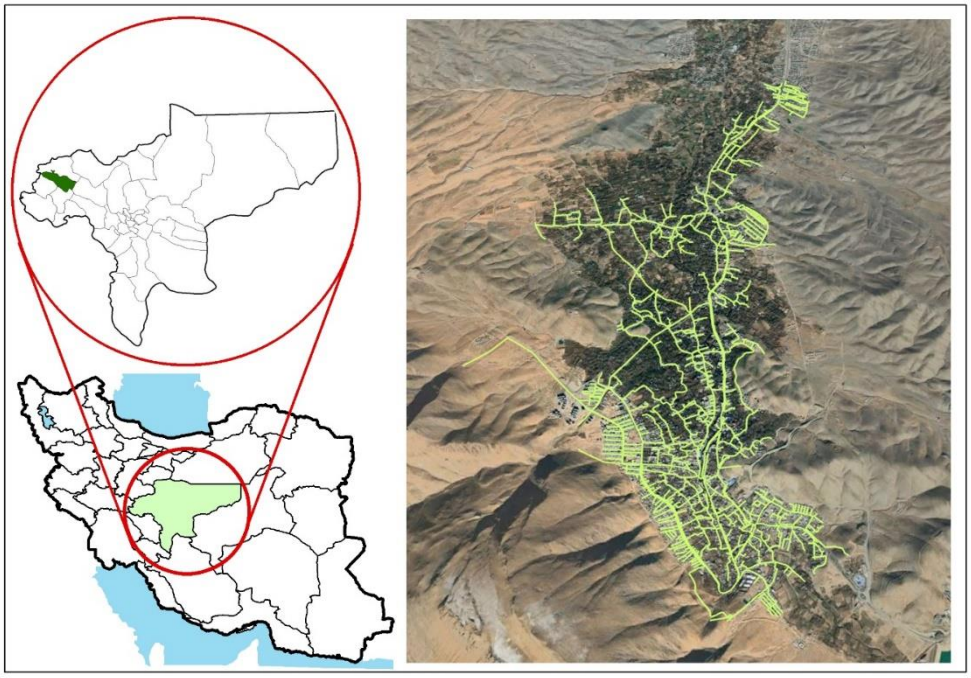


Figure 1. Schematic image of the location of Khansar city.

3.2. Hydraulic Characteristics and Zones

The water distribution network of Khansar city is about 130 km long. The city's water supply is mostly sourced from wells and, a few times a year, through the Baghkal Dam. The transmission line from Baghlak dam to the water treatment plant is 7.6 km long and has 400 and 500 mm diameters. The diameter of the pipes used in the distribution network is 32 to 400 mm, and they are made of asbestos cement, polyethylene, ductile iron, and steel.

The water distribution network consists of 7 completely independent pressure zones. Each zone is fed by one or two reservoir. Figure 2 shows the water distribution network of Khansar city and its pressure zones. Table 2 gives the length and type of pipes used in each zone.

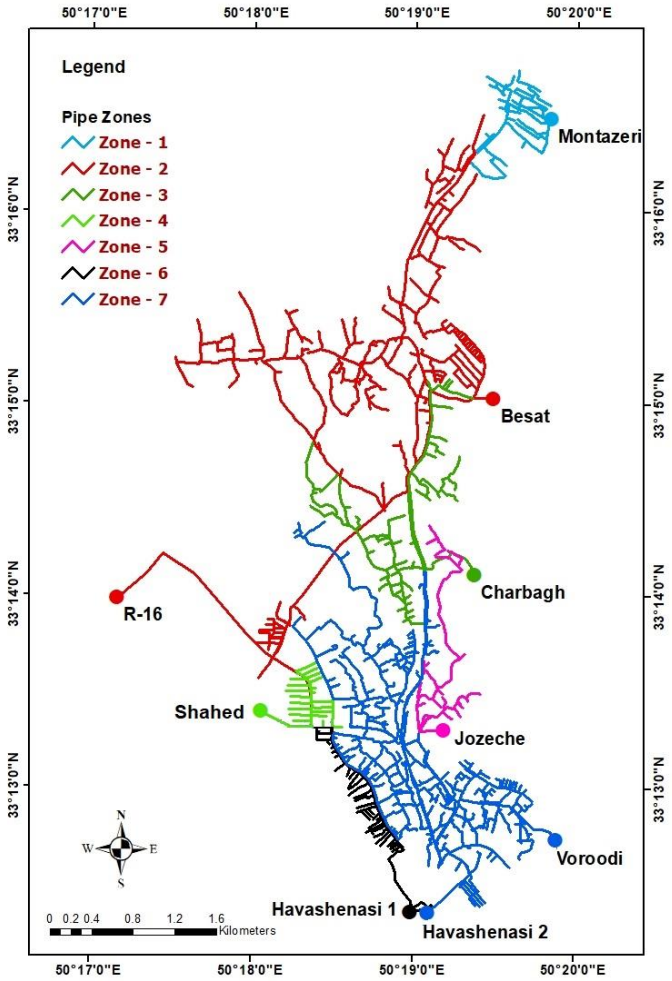


Figure 2. Zoning of Khansar water distribution network.

Table 2. Specifications of water distribution network pipes of Khansar city.

Zone name	Material				Total
	Asbestos cement	Ductile Iron	Polyethylene	Steel	
Zone1	2506	475	4721	0	7702
Zone2	26260	3321	11978	10	41626
Zone3	9613	37	3908	0	13558
Zone4	3740	82	940	0	4762
Zone5	4782	233	843	0	5858
Zone6	6328	0	892	0	7245
Zone7	22173	13432	9177	827	45846
Total	78529	18101	32633	837	130419

As shown in Figure 3, the consumption pattern exhibits significant diurnal variations. The minimum hourly coefficient is 0.792 at 4:30 AM, and the maximum is 1.51 at 12:30 PM.

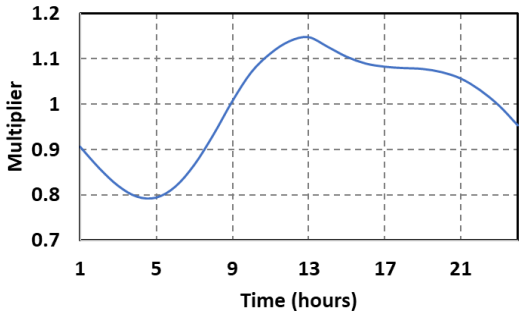


Figure 3. Hourly water consumption pattern.

3.3. Water Quality Analysis

To simulate chlorine decay in the network, diffusion coefficient, bulk decay and wall decay coefficients are needed. The diffusion coefficient of chlorine in water for a temperature of 20 °C equals 1.208e-9 m^2/s [30]. The bulk chlorine coefficient can vary depending on water temperature, and therefore, a value of 0.3 $(mg/L)^{(1-n)/d}$, which represents an average from various studies, was used [31]. The wall decay coefficient varies based on the pipe material. Given that most of the pipes in the network are made of asbestos and considering the significant impact of pipe age on wall decay, the maximum and conservative value of this coefficient was extracted from relevant tables and applied. According to most researchers, this coefficient is considered first-order [21, 24]. In this study, a network runtime of 96 hours (4 days) was considered to achieve a steady-state chlorine concentration. In other words, the residual chlorine concentration in the entire distribution network was monitored every 24 hours. Considering that the chlorine concentration on the fourth day was not significantly different from the third day, 96 hours duration was chosen as the appropriate time for simulation.

3.4. Chlorine Dosing Optimization

Optimization of chlorine dosing was conducted individually for each zone to minimize daily chlorine consumption while maintaining residual chlorine levels within permissible limits. The chlorine dose injected into the reservoirs was varied from 0.2 to 3 mg/L in increments of 0.1. Then, for each zone, the graphs of the water volumes versus the injected chlorine concentration were drawn, and the optimal amount of injected chlorine was determined according to the constant values of the water volume. Optimization of chlorine concentration for zones connected to two water tanks was carried out similarly to other zones, with the difference that for zones with two tanks, the chlorine injection concentration was performed separately for each tank. Therefore, more runs were required for these zones. The maximum and minimum chlorine concentrations in each zone were monitored to ensure compliance with both the upper and lower limits of the permissible chlorine range. The corresponding chlorine consumption was calculated based on the 24-hour diurnal demand pattern and optimum chlorine concentration and compared with the conditions before optimization.

4. Results and Discussion

4.1. Chlorine Distribution Simulation in the Existing Condition

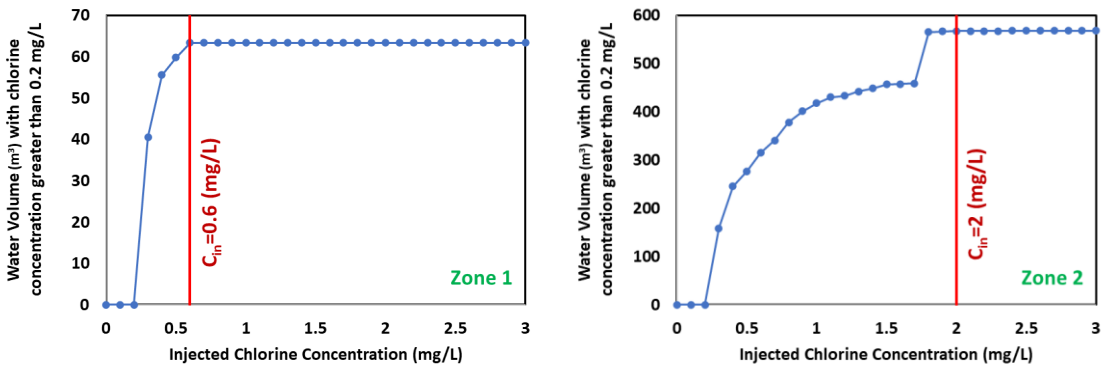
Based on the data obtained from the Isfahan Water and Wastewater Company, the current chlorine dose in all reservoirs is 2 mg/L at all times. The network was analyzed under existing conditions, and the daily chlorine consumption was calculated based on the average flow rate of each reservoir, as shown in Table 3. It is worth noting that due to the fluctuations in consumption over 24 hours, the maximum chlorine consumption was 1202.4 g/h, and the minimum consumption was 842.4 grams per hour.

Table 3. Calculation of mass flow rate of injected chlorine before optimization.

Zone	Reservoir name	Injected chlorine concentration (mg/L)	Flowrate (L/s)	Injected chlorine (g/h)
Zone1	Montazeri	2	28	201.6
Zone2	R16	2	9	64.8
	Besat	2	19	136.8
Zone 3	Charbagh	2	12	86.4
Zone 4	Shahed	2	40	288
Zone 5	Jozeche	2	6	43.2
Zone 6	Havashenasi 1	2	8	57.6
Zone 7	Havashenasi 2	2	8	57.6
	Voroodi	2	27	194.4
	Total			1130.4

4.2. Finding the Optimal Amount of Injected Chlorine

According to Iran's drinking water standard 1053, the chlorine concentration in each designated zone must not fall below 0.2 mg/L. So, as mentioned earlier, water volume with chlorine concentration greater than 0.2 mg/L was plotted versus injected chlorine concentration in the reservoir for various zones to achieve the optimal amount of injected chlorine. In order to obtain the data for these graphs, 29 runs were performed for each zone, and the minimum and maximum chlorine concentration values were recorded. As shown in Figure 4, the volume of water containing chlorine with a concentration of more than 0.2 mg/L increases with the increase of injected chlorine until it reaches a constant value. This means that injecting more chlorine increases the residual chlorine in the water distribution network, while the concentration of 0.2 mg/L is sufficient. The optimal amount of chlorine for each zone is shown in the graphs in Figure 4.



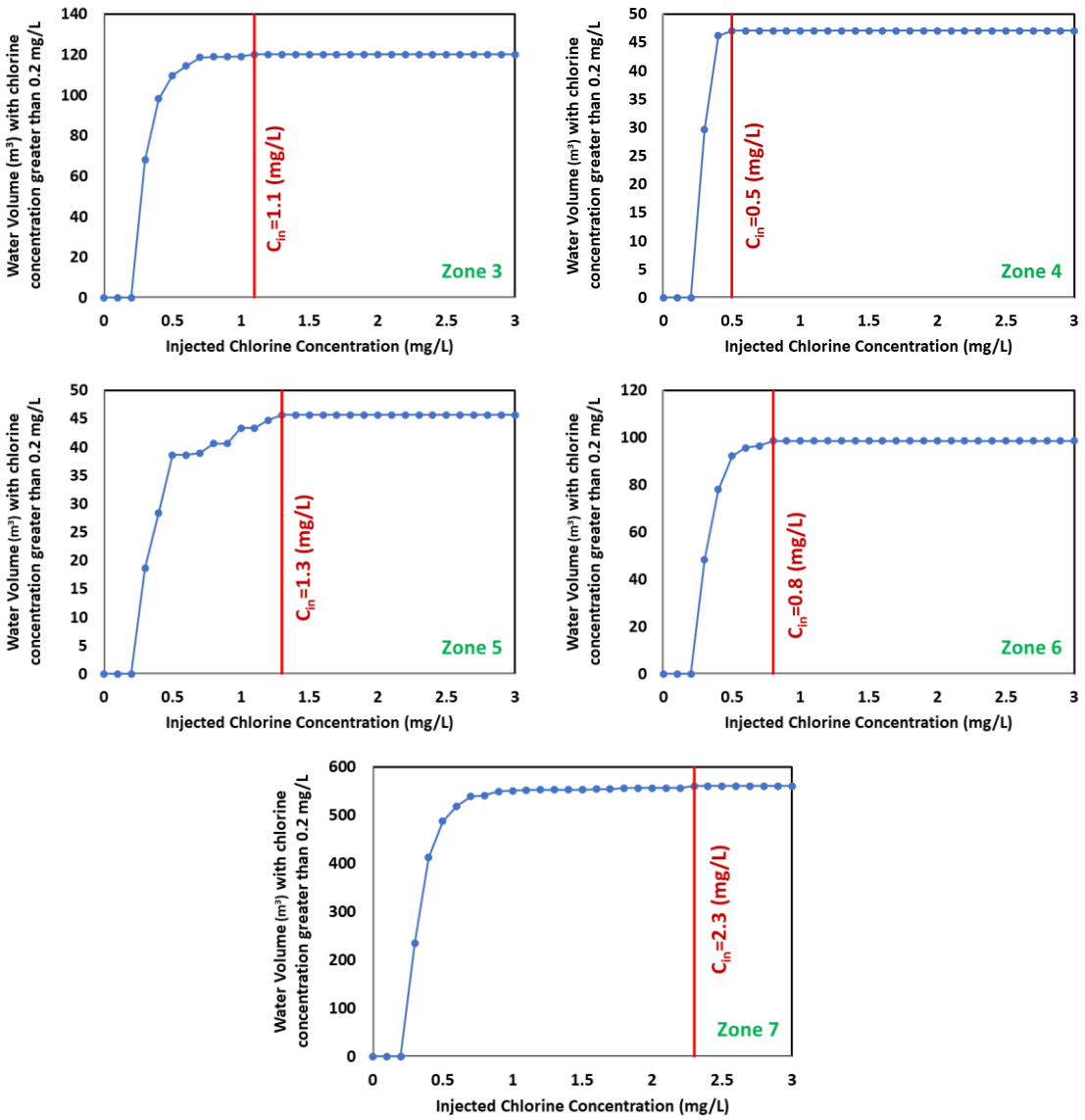


Figure 4. Water volume with chlorine concentration greater than 0.2 mg/L vs injected chlorine concentration in reservoir for various zones.

After finding the optimal amounts of injected chlorine, the remaining chlorine map in the entire water distribution network was prepared before and after optimization, as shown in Figure 5. The amount of chlorine needed per hour was also calculated using the coefficients of the consumption pattern. The optimal amount of chlorine and the results are given in Table 4.

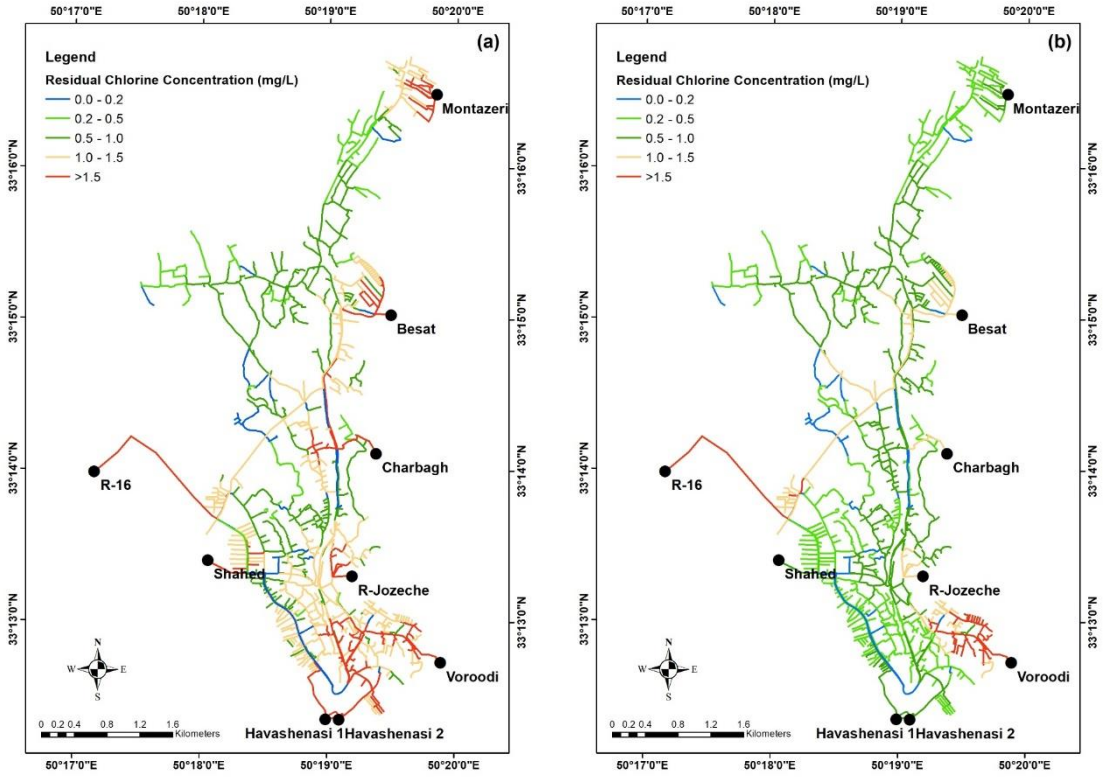


Figure 5. The amount of residual chlorine in the existing condition (a) after 2 hours (b) after 24 hours.

Table 4. Calculation of mass flow rate for injected chlorine after optimization.

Zone	Reservoir name	Injected chlorine concentration (mg/L)	Flowrate (L/s)	Injected chlorine(g/h)
Zone1	Montazeri	0.6	28	60.5
Zone2	R16	2.1	9	68
	Besat	1.5	19	102.6
Zone 3	Charbagh	1.1	12	47.5
Zone 4	Shahed	0.6	40	86.4
Zone 5	Jozeche	1.3	6	28
Zone 6	Havashenasi 1	0.8	8	23
Zone 7	Havashenasi 2	0.6	8	17.3
	Voroodi	2.3	27	223.5
		Total		656.7

Analysis of the existing and optimized conditions revealed that, of the 1127 pipes in the water supply network, 34 pipes had residual chlorine concentrations below the standard (0.2 mg/L) in the existing condition. However, following optimization and adjustments to the chlorine dosing in the reservoirs, this number decreased to 12. It should be noted that because the water in these pipes is stagnant, increasing the amount of injected chlorine cannot increase the residual chlorine in the pipes. In the existing condition, 51.9% of the pipes had residual chlorine below 1 mg/L, while in the optimized condition, this percentage decreased to 61.8%. Although the amount of chlorine was reduced by 42%, the volume of water that did not meet the standard in the existing condition was

34.37 m³, which decreased to 11.8 m³ after optimization. In other words, 99.2% of the network has a concentration more than 0.2 mg/L after optimization. Therefore, by adjusting the chlorine dosing, 66% of the water volume with insufficient chlorine was brought up to standard.

5. Conclusion

This study optimized the chlorine dosing in various reservoirs of the Khansar city network through trial and error. WaterGEMS software was used for the simulation of the hydraulic and water quality of the distribution network. In the first step, the existing conditions of residual chlorine in the distribution network were investigated. According to the results, 34 pipes out of 1127 pipes in the distribution network had residual chlorine concentrations less than 0.2 mg/L. In the next step, in order to optimize the chlorine dose, the distribution network was analyzed under the various concentrations of injected chlorine in each reservoir and the optimal dosing rate was determined for each reservoir. The results indicate that chlorinating the network with the newly obtained concentrations significantly improved the network's performance compared to the existing condition. Changes in the chlorine dosing to the reservoirs not only did not increase the daily chlorine consumption but also reduced it. This study demonstrated that appropriate chlorine dosing, especially during peak hourly consumption, resulted in a more uniform distribution and improved conditions in critical network points.

After optimization, a higher percentage of pipes had chlorine concentrations between 0.2 and 1 mg/L. Additionally, 66% of the previously substandard-quality water volume met the standard after implementing the optimized dosing strategy. Zones connected to a single reservoir had consistently standard chlorine levels due to the shorter network length. Zones connected to two reservoirs had the highest number of pipes with below-standard chlorine levels due to their longer lengths.

References

1. Coelho, S.T., (1996), “Performance assessment in water supply and distribution”, Ph.D.Thesis, Civil & Offshore Engineering Department, Heriot-Watt University, Edinburg. UK.
2. Haghighi, M.R., and Alian Koupaee, T., (2023) “Investigating the effects of temperature on chlorine decay coefficients in water distribution networks using a dynamic quality model”. Journal of Water and Wastewater; 47: p. 21-9. [In Persian].
3. Coulson, J.M., and Richardson, J.F. (1964), “Chemical Engineering”, 2nd Edn. Pergamon Press, Oxford, (3 Volumes).
4. Tabesh M, and Azadi B. (2007), “Optimum management of water distribution networks via determination of the optimum rate of chlorine injection using analytical excel and genetic algorithms”. Journal of Water and Wastewater Plan Management 77: p. 2-12. [In Persian].
5. Tryby, M. E., Boccelli, D. L., Uber, J. G., and Rossman, L. A. (2002), “Facility location model for booster disinfection of water supply networks”, Journal of Water Resources Planning and Management, 128(5): p. 322-333.
6. Prasad, T. D., Walters, G. A., and Savic, D. A. (2004), “Booster disinfection of water supply networks: Multiobjective approach”, Journal of Water Resources Planning and Management, 130(5): p. 367-376.

7. Goyal, R. V., and Patel, H. M. (2017), "Optimal location and scheduling of booster chlorination stations for drinking water distribution system", Journal of Applied Water Engineering and Research, 5(1): p. 51-60.
8. Islam, N., Sadiq, R., and Rodriguez, M. J. (2017), "Optimizing locations for chlorine booster stations in small water distribution networks", Journal of Water Resources Planning and Management, 143(7): 04017021.
9. Javadinejad, S., Ostad-Ali-Askari, K., and Jafary, F. (2019), "Using simulation model to determine the regulation and to optimize the quantity of chlorine injection in water distribution networks", Modeling Earth Systems and Environment, 5: p. 1015-1023.
10. Maleki, M., Ardila, A., Argaud, P. O., Pelletier, G., and Rodriguez, M. (2023), "Full-scale determination of pipe wall and bulk chlorine degradation coefficients for different pipe categories", Water Supply, 23(2): p. 657-670.
11. Moeini, M., Sela, L., Taha, A. F., and Abokifa, A. A. (2023), "Bayesian optimization of booster disinfection scheduling in water distribution networks", Water Research, 242: p. 120117.
12. Frederick, F. D., Marlim, M. S., and Kang, D. (2024), "Optimization of Chlorine Injection Schedule in Water Distribution Networks Using Water Age and Breadth-First Search Algorithm", Water, 16(3): p. 486.
13. Gibbs, M. S., Dandy, G. C., and Maier, H. R. (2010), "Calibration and optimization of the pumping and disinfection of a real water supply system", Journal of Water Resources Planning and Management, 136(4): p. 493-501.
14. Kang, D., and Lansey, K. (2010), "Real-time optimal valve operation and booster disinfection for water quality in water distribution systems", Journal of Water Resources Planning and Management, 136(4): p. 463-473.
15. Ohar, Z., and Ostfeld, A. (2014), "Optimal design and operation of booster chlorination stations layout in water distribution systems", Water research, 58: p. 209-220.
16. Ayvaz, M. T., and Kentel, E. (2015), "Identification of the best booster station network for a water distribution system", Journal of Water Resources Planning and Management, 141(5): p. 04014076.
17. Goyal, R. V., and Patel, H. M. (2018), "Optimal location and scheduling of booster chlorination stations using EPANET and PSO for drinking water distribution system", ISH Journal of Hydraulic Engineering, 24(2): p. 157-164.
18. Avvedimento, S., Todeschini, S., Giudicianni, C., Di Nardo, A., Walski, T., and Creaco, E. (2020), "Modulating nodal outflows to guarantee sufficient disinfectant residuals in water distribution networks", Journal of Water Resources Planning and Management, 146(8): p. 04020066.
19. Tsitsifli, S., and Kanakoudis, V. (2021), "Assessing the impact of DMAs and the use of boosters on chlorination in a water distribution network in Greece", Water, 13(16): p. 2141.
20. Haas, C., and Karra, S. (1984), "Kinetics of wastewater chlorine demand exertion", Journal of Water Pollution Control Federation, 56(2): p. 170.
21. Rossman, L.A, (2000), "EPANET User's manual US. Environmental Protection Agency", Cincinnati, Ohio: Drinking Water Research.
22. Kurek, W., and Ostfeld, A. (2013), "Multi-objective optimization of water quality, pumps operation, and storage sizing of water distribution systems", Journal of Environmental Management, 115: p. 189-197.

23. Rosalam, H., and Krishnaiah, S.D., (2007), “Free Chlorine Residual Content within the Drinking Water Distribution System”, International Journal of Physical Sciences, 2(8): p.196-201.
24. Al-Jasser, A. (2007), “Chlorine decay in drinking-water transmission and distribution systems: Pipe service age effect", Water Research, 41(2): p. 387-396.
25. Hallam, N., West, J., Forster, C., Powell, J. and Spencer, I. (2002), “The decay of chlorine associated with the pipe wall in water distribution systems”, Water Research, 36(14): p. 3479-3488.
26. Publication No. 3-116, (1371) “Drinking Water Quality Standard”, Bureau of Research and Technical Standards of the Program and Budget Organization and Water Engineering Standards of the Ministry of Energy.
27. Publication No. 117-3, (2013) “Rules for the Design of Urban and Rural Water Transmission and Distribution Systems” Office of Research and Technical Standards of the Program and Budget Organization and Water Engineering Standards of the Ministry of Energy.
28. Publication No. 1053, (2008), “Physical and chemical characteristics of standard drinking water”, Iran Standard and Research Institute, fifth revision.
29. Simpson, K. and Hayes, K. (1998), “Drinking water disinfection by-products: an Australian perspective”, Water Research, 32(5): p. 1522-1528,
30. Hashimoto, K., Otsuki, N., Saito, T., and Yokota, H. (2013), “Application of electrical treatment to alteration of cementitious material due to leaching”, Journal of Advanced Concrete Technology, 11(3): p. 108-118.
31. Maleki, M., Ardila, A., Argaud, P. O., Pelletier, G., and Rodriguez, M. (2023). “Full-scale determination of pipe wall and bulk chlorine degradation coefficients for different pipe categories”. Water Supply, 23(2): p. 657-670.

© 2025 by the authors. Licensee SCU, Ahvaz, Iran. This article is an open access article distributed under the terms and conditions of the Creative Commons Attribution 4.0 International (CC BY 4.0 license) (http://creativecommons.org/licenses/by/4.0/).

Journal of Hydraulic Structures

Volume 11 – Issue 2 – April 2025

Contents:

01 Construction of Meandering Channel and Its Application in Investigation of Bed Topography around Hydraulic Structures

Nargess Moghaddassi; Mohammad Vaghefi

28 Simulation of Tsunami Waves Using Mike 3 Flow Model FM

Vahid Naderkhanloo; Mohammad Hemmati; Hojjat Ahmadi

44 An investigation on the parameters affecting the behavior of broadly graded, dispersive base soil-filter systems in earth dams

Amir Hossein Vakili; Amin Falamaki

61 Investigating the Behavior of Jacket Offshore Steel Structure under Blast Loading

Farhad Hosseinlou; Wissam Asaad Ibrahim; Mojtaba LabibZadeh

87 Investigating the vulnerability of underground water to pollution (case study: East and Northeast of Chaharmahal and Bakhtiari province)

Mohammadsadegh Talebi

108 Full scale optimization of chlorine injection pattern in Khansar water distribution network using WaterGEMS

Ali Poorkarimi; Habib Asi; Shahrzad Maleki

Shahid Chamran University of Ahvaz